



HAL
open science

Quantum scattering beyond quasi one-dimensional systems

Mathieu Istas

► **To cite this version:**

Mathieu Istas. Quantum scattering beyond quasi one-dimensional systems. Mesoscopic Systems and Quantum Hall Effect [cond-mat.mes-hall]. Université Grenoble Alpes, 2019. English. NNT: 2019GREAY023 . tel-02445475

HAL Id: tel-02445475

<https://theses.hal.science/tel-02445475>

Submitted on 20 Jan 2020

HAL is a multi-disciplinary open access archive for the deposit and dissemination of scientific research documents, whether they are published or not. The documents may come from teaching and research institutions in France or abroad, or from public or private research centers.

L'archive ouverte pluridisciplinaire **HAL**, est destinée au dépôt et à la diffusion de documents scientifiques de niveau recherche, publiés ou non, émanant des établissements d'enseignement et de recherche français ou étrangers, des laboratoires publics ou privés.

THÈSE

Pour obtenir le grade de

DOCTEUR DE LA COMMUNAUTÉ UNIVERSITÉ GRENOBLE ALPES

Spécialité : Physique Théorique

Arrêté ministériel : 25 mai 2016

Présentée par

Mathieu ISTAS

Thèse dirigée par **Xavier WAIN TAL**, CEA

et codirigée par **Christoph GROTH**

préparée au sein du **Laboratoire PHotonique, ELelectronique et
Ingénierie Quantiques**

dans l'**École Doctorale Physique**

Diffusion quantique au delà des systèmes quasi-unidimensionnels

Quantum scattering beyond quasi one- dimensional systems

Thèse soutenue publiquement le **19 juin 2019**,
devant le jury composé de :

Monsieur Xavier WAIN TAL

Directeur de Recherche, CEA Grenoble, Directeur de thèse

Monsieur Stephan Roche

Professeur des Universités, Institut Català de Nanociència i
Nanotecnologia , Rapporteur

Monsieur David Carpentier

Directeur de Recherche, Ecole Normale Supérieure de Lyon, Rapporteur

Monsieur Christophe Groth

Chargé de Recherche, CEA, Co-directeur de thèse

Monsieur Hervé Courtois

Professeur des Universités, Institut NEEL CNRS/UGA UPR2940,
Président

Monsieur Rodolfo JALABERT

Professeur des Universités, Université de Strasbourg I PCMS □
Département Magnétisme des Objets NanoStructurés (DMONS),
Examineur



Abstract

Numerical simulations in the field of quantum nanoelectronics are often restricted to devices of finite size that are connected to the macroscopic world with quasi-one-dimensional electrodes. This thesis presents novel numerical methods that lift many of these restrictions, in particular rendering realistic simulations of three-dimensional systems possible.

The first part introduces a robust and efficient algorithm for computing bound states of infinite tight-binding systems that are made of a scattering region connected to semi-infinite leads. The method is formulated in close analogy to the wave-matching approach used to compute the scattering matrix. It also allows one to calculate edge or surface states, e.g. the so-called Fermi arcs.

The second part is dedicated to a new numerical method, based on the Green's function formalism, that allows to efficiently simulate systems that are infinite in 1, 2 or 3 dimensions and *mostly* invariant by translation. Compared to established approaches whose computational costs grow with system size and that are therefore plagued by finite size effects, the new method allows one to directly reach the thermodynamic limit. It provides a practical route for simulating 3D setups that have so far remained elusive.

Both methods are illustrated by applications to several quantum systems (a disordered two-dimensional electron gas, a graphene device...) and topological materials (Majorana states in 1D superconducting nanowires, Fermi arcs in 3D Weyl semimetals...). This thesis ends with a last application that study transport properties of a disordered Weyl semimetal, a system that could not be studied with earlier approaches.

Contents

I	Quantum Transport simulations in nanostructures	9
1	Outline of the thesis	11
1.1	The need of new numerical tools for quantum transport: the MTIS approach	11
1.2	Note about free software implementation	12
1.3	Quantum transport at the mesoscopic scale	15
2	Introduction to numerical quantum transport	19
2.1	The wave guide problem	20
2.2	Discretization of a one-dimensional Hamiltonian	21
2.3	The infinite lead problem	23
2.3.1	The mode equation	25
2.3.2	Solutions to the mode equation (2.17)	26
2.4	Scattering formalism	28
2.4.1	The scattering matrix definition	29
2.4.2	Properties of the scattering matrix	30
2.4.3	From the scattering matrix to conductance	31
2.4.4	The scattering problem as a set of linear equations	33
2.5	Green's function formalism	36
2.5.1	Definition and interpretation	37
2.5.2	Properties of the Green's function	38
2.5.3	Adding perturbations in the Green's function formalism	39
2.5.4	General formulation of the Green's function as a linear problem	41
2.6	The Fisher-Lee relation for arbitrary tight-binding systems	44
II	A general algorithm for computing bound states in infinite tight-binding systems	

	49
3 A general formulation for the bound state problem	51
3.1 Introduction	51
3.2 The bound state problem	53
3.2.1 General model	53
3.2.2 Lead modes	54
3.2.3 Formulation of the bound state problem	55
3.3 Numerical algorithm for finding bound states	56
3.3.1 Algorithm I: non-Hermitian formulation	56
3.3.2 Hermitian formulation	57
3.3.3 Algorithm II: root finder in the Hermitian formulation	58
3.3.4 Algorithm III: improved convergence thanks to gradient calculation	59
3.3.5 Visualization of algorithms I, II and III	62
4 Applications of the bound state solver	63
4.1 Application to quantum billiards	63
4.2 Topological materials	65
4.2.1 One-dimensional superconducting nanowire, Majorana bound states	65
4.2.2 Quantum spin Hall effect	68
4.2.3 Fermi arcs in Weyl semimetals	70
4.3 Conclusion	72
III Mostly translationally invariant systems	75
5 The mostly translationally invariant systems concept	79
5.1 Introduction	79
5.1.1 Problem formulation	81
5.1.2 Principle of the technique	84
6 Applications to MTIS systems	89
6.1 Friedel oscillations in a two-dimensional electron gas	91
6.2 Quantum spin hall effect	93
6.3 Graphene nanoribbon	95
6.4 Weyl semimetal three terminal device	96
7 Analytical and numerical techniques in MTIS solver	105
7.1 The Residue problem	105
7.1.1 Formulation of the Residue problem	106

7.1.2	Solution to the residue problem	107
7.1.3	Proof of Eq. (7.19)	108
7.2	Numerical Fourier transform	110
7.3	The glueing sequence	111
7.4	The bound state problem	114
7.5	Conclusion	116
A	Bound state appendix	121
A.1	Normalization of the bound state	121
A.2	Proof of Eq. (3.13)	121
A.3	Degenerate eigenvalues	122
B	Mostly translationally invariant system appendix	125
B.1	Laurent expansion of the inverse of a matrix	125
	Bibliography	129

CONTENTS8

CONTENTS

Part I

Quantum Transport simulations in nanostructures

Chapter 1

Outline of the thesis

1.1 The need of new numerical tools for quantum transport: the MTIS approach

Quantum electronics systems range from a few μm down to the nanoscale, at temperatures low enough so that electrons can behave coherently. At these scales the physical devices inherently behave according to the laws of quantum physics, where particles behave as waves, introducing e.g. interference effects. Recent realizations of devices under these conditions are materials like topological insulators, Majorana fermions, graphene bilayer, etc. The modelization of these nanoscale systems is not only a fundamental science playground anymore, but must adequately reproduce realistic devices. This necessarily leads to a dramatic increase in the complexity of the systems under study, due for instance to the various geometries and materials, therefore making numerical simulations one of the key approaches.

Under the conditions of low temperature and voltage, the nanoelectronics devices, which contains up to a billion electrons, can be accurately described by the mean-field picture. This reduces the complex many-body problem to a simpler problem that is usually formulated with linear algebra. Several numerical methods have been developed to study properties of nanoelectronic systems, such as the Recursive Green's function^[1-3]. Figure 1.1 shows a typical nanostructure simulated by one of the established methods, a finite central region connected to one or several (three in our case) electrodes. The central region could be of an arbitrary shape and can simulate a variety of materials, e.g. insulators or superconductors, but is of finite size with usual methods. The conducting electrodes are infinite in length and, in established methods, of a finite width. In the following sections the electrodes will usually be referred to as “leads” and the central region as a “scattering region”, hence paving the way to a more mathematical description.

However, despite the plethora of efficient methods available, there are

two bottlenecks that remains in most simulations of quantum transport. The first one is that typical general and exact numerical algorithms that simulate generic three-dimensional devices scale as L^7 , where L is the size of the system, which is a prohibitive cost to simulate realistic systems. The second one is that the electrodes geometry is limited to quasi-1d, so that electrons are confined in all but one direction. In this thesis we develop numerical methods to lift these two limitations, and we are able for instance to simulate the geometry displayed in Fig. 1.2a, where the central region is a 3D half-space (infinite in two directions and semi-infinite in one) connected to two semi-infinite leads.

There is a conceptual difference between our methods and usual approaches. For instance, the recursive Green's function is a bottom-up approach, i.e. the system elements, which can be sites^[4] or stacks of sites^[2], are assembled one by one from the vacuum. This necessarily implies a computational cost that increases monotonously with the system size. This feature is shared by many other approaches, such as the kernel polynomial^[5,6]. Reference 6 is a recent description of the approximate algorithms that scale linearly with the system size.

In this thesis we elaborate numerical methods following a top-bottom design to avoid finite size effects. In a nutshell, we simulate first a bulk system, i.e. a translationally invariant system (TIS), and then modify elements to obtain a *mostly* translationally invariant system (MTIS). In Fig. 1.2, the TIS is a Weyl semimetal infinite in three directions. In the final MTIS, the translational invariance is broken by the two quasi-1d leads. Using this approach, we overcome the limitations of finite size for the central region (which is of $10^5 - 10^6$ sites for exact simulations and of 10^9 sites for approximate methods) and of finite width for electrodes. With the novel methods developed here we are able to access local quantities, e.g. local density of states, and non-local quantities, such as the conductance, of MTIS where the finite size effects are a severe limitation with established algorithms. Formally, we simulate nanoelectronic devices that are infinite in one or several dimensions, i.e. provide a numerical solution to the multidimensional scattering problem.

We start the manuscript by a short note about open-source implementation, followed by an introduction to relevant scales in nanoelectronics.

1.2 Note about free software implementation

In this thesis, we developed two numerical methods. This implies not only to describe the algorithm mathematically, but also to implement it in a programming language. The mathematical walk-through of algorithms is the subject of two papers and is rather expansive, but only a little amount of text is dedicated on the implementation itself, although it can be considered

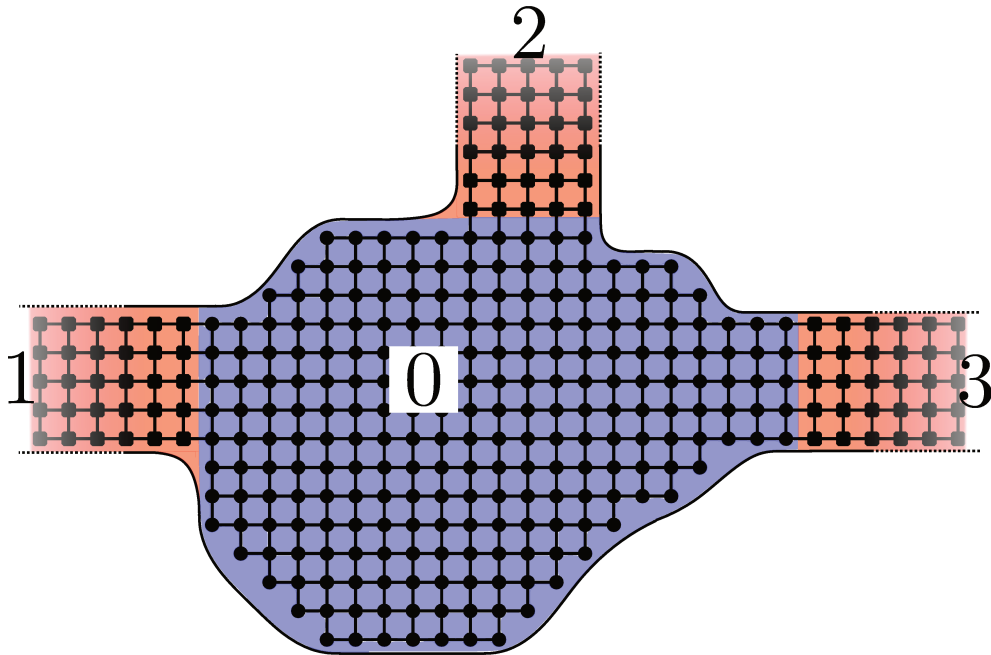


Figure 1.1: Sketch of a typical nanoelectronic device. The central section (in blue) labeled by 0 is the scattering region. The leads (in red) are labeled by 1, 2, and 3 and stretch to infinity.

equally important. This short section argues the importance of a good implementation, and why the methods developed here will be incorporated in Kwant.

Kwant^[7] is a free (open-source) software that simulates quantum transport of nanoelectronic systems. It uses the BSD permissive free software license, which allows people to copy, use or modify the source code. It is so permissive that the source code could even be incorporated in a proprietary software at no cost, so that Kwant could almost be considered as falling in "public domain".

The motivation to write the code under this permissive license is twofold. The first one is the philosophical aspect, recalling that the "free" in free software does not stand for free of charge but rather for freedom. Namely, the freedom of: (i) running the program, (ii) studying and modifying the program, (iii) redistributing original or modified copies of the program. These are considered by the GNU movement as fundamental liberties that should not be repealed^[8]. The second motivation is more pragmatic. Many research groups are writing code for internal use only, usually passing it down between students with a few modifications at each step and with very little documentation. This implies the existence of many similar codes scattered

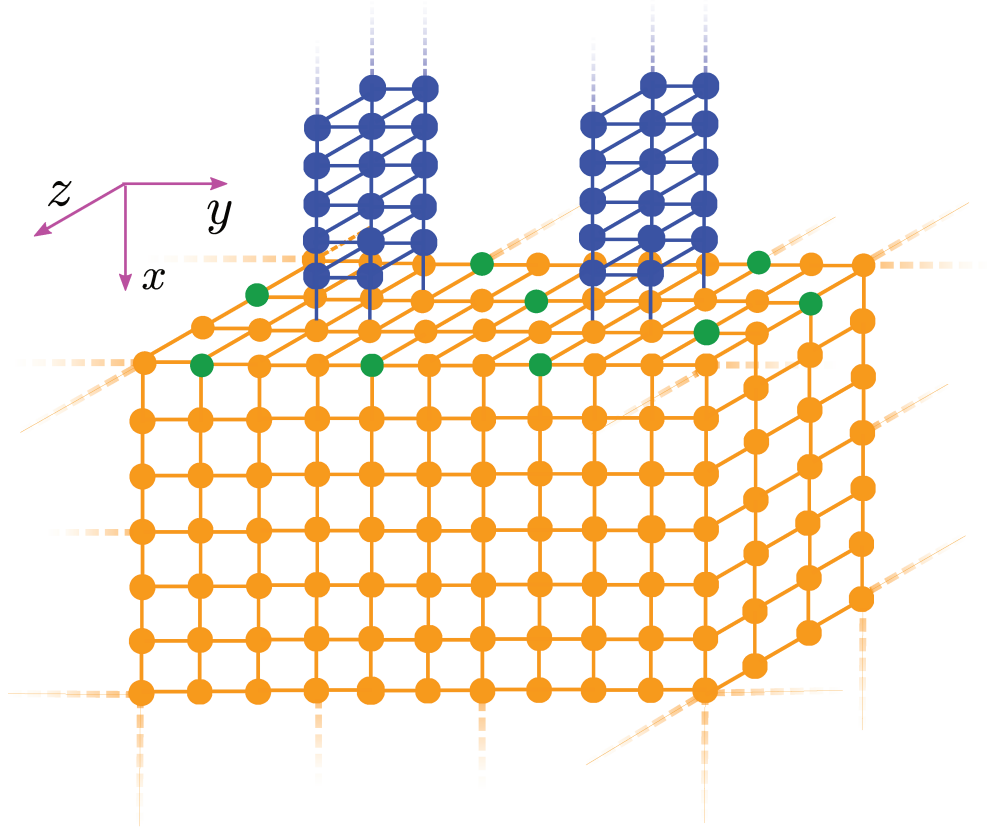


Figure 1.2: Schematic drawing of a typical MTIS (mostly translationally invariant system) simulated in this thesis. Similarly for Fig. 1.1, the device is modeled by a lattice that encompasses from one to many atoms in a site. The lines represent the connexions between the sites. The orange part is a complex topological material that is infinite in the y - and z -directions, and semi-infinite in the x -direction. The leads (in blue) are a simple metal, extending to infinity in the negative x .

in different groups and may be considered inefficient since exchanging codes is a very simple task with today's means.

These are the different principles Kwant is following: (i) having an interface close to the mathematics describing the problem, (ii) including a well furnished documentation and tutorials, (iii) writing the code in an easy to learn and widespread programming language, namely Python. It should also provide access to the concepts and algorithms, either pedagogically in the tutorials or through articles, not to be a black-box software where the user has no information about the operations or eventual approximations performed in the calculation.

1.3 Quantum transport at the mesoscopic scale

This section introduces the concept of coherent quantum transport mentioned in the introduction and used throughout the thesis. A crude approximation of the typical device scale where coherent effects happens is called by the old-fashioned word “mesoscopic”, which stands for a length in between the atomic scale and the scale of bulk physics. The length of these devices is such that in one hand some dimension of the device is much bigger than the De Broglie wavelength but in the other smaller than the phase-relaxation length. In a simple picture, devices smaller than the latter scale enhance the possibilities for quantum effects to be observed. Notice that quantum effects can also be present at longer scales, a notable example being the weak localization.

The phase-relaxation length is defined as the average length for which an electron keeps its phase. This is a purely quantum phenomena that can be understood with interference experiments. For instance, splitting a beam of electrons in a perfect crystal and recombining them after a certain distance traveled results in an interference pattern. If we introduce impurities in the crystal that randomly (and dynamically) scatter electrons then the interference obtained shows random variations that average to zero. The phase-relaxation length not only depends on the density and nature of the impurities, but also strongly depends on the temperature. Cooling down the device reduces and then suppresses the phonon density, so that the last main source of decoherence left is the electron-electron scattering. The phase coherence length therefore sets a scale where behavior becomes *qualitatively* different, from electrons behaving mostly classically beyond that scale to electrons showing interference effects below it. In this thesis we study systems that are fully coherent, so that we assume the phase coherence length to be bigger than all other scales.

Due to impurities, lattice vibrations or collisions with other electrons, deviations in the electron trajectories occur, which result in a change of its

momentum. The length an electron travels without losing its initial momentum is defined as the mean free path. Below that scale, the behavior of electrons is ballistic, so that the electrical resistivity of the device is negligible. The leads, despite being much bigger than the device (they are assumed to be infinite in one direction), are considered ballistic. Indeed, they are simply regarded as means to inject current, so we assume the (super)conductor of the lead to be coherent and ballistic.

The phase relaxation length and the mean free path provide two scales to the device. The former length sets a limit at which a nanoelectronic sample exhibits quantum behavior, while the latter defines a ballistic conductor.

A typical nanoelectronic device made of a scattering region (in blue) and three leads (in red) is pictured in Fig. 1.1. A lattice is made apparent on all regions, where the dots represent the tight-binding sites and the lines connexions between the neighboring sites. This representation is formally introduced in the next sections and used throughout the thesis. The leads are made of a unit cell (e.g. in lead 1 it encompasses 5 sites) that repeats periodically to infinity. Because of the periodicity, the wavefunctions of the lead can be expanded in a plane wave basis, so that the behavior of the (super)conductor is fully ballistic.

A very common problem in nanoelectronics is to describe the scattering of an incoming wave into the other leads. In the absence of inelastic scattering, this field has matured to the point that many softwares can solve this problem for arbitrary scattering regions and leads^[9-11]. Chapter 2 derives the problem of quantum transport in quasi-1d leads and scattering regions as a set of linear equations, readily to be implemented.

The focus in these transport calculations is on the propagating states, as they are the states injecting and carrying current. However, the full spectrum of the Hamiltonian also includes evanescent states, which are of utmost importance in some setup, e.g. Josephson junctions. Chapter 3 derives a general and robust method that can calculate the bound states properties in setup consisting in a central region connected to semi-infinite electrodes.

The two length scales introduced in this section may vary from a few nanometers, to a hundred of μm in some systems^[12]. Systems with long coherence and collision times include for instance the quantum spin Hall effect in HgTe quantum wells^[13], where backscattering events are prohibited, or graphene deposited on boron nitride^[14]. For graphene, the ratio between the smallest length scale, namely the intervalley length, can be therefore 5 orders of magnitude smaller than the phase-relaxation length. In three dimensions simulations of realistic devices often involve systems with more than a billion sites. The scaling of the most efficient established algorithms does not allow one to make exact numerical simulations of such systems. To address this problem in this thesis we study the multidimensional scattering,

which generalizes the standard scattering problem. The developments in this thesis allows one to simulate ballistic electrodes that are infinitely wide, instead of quasi-1d leads that confine electrons in two directions. This thesis renders simulations of fully coherent scattering regions that are infinite in several directions (and/or semi-infinite in one) possible, as in Fig. 1.2a. From these simulations it is possible to extract numerous quantities, such as the conductance of the density of states of a coherent quantum device.

Chapter 2

Introduction to numerical quantum transport

This section introduces central concepts in quantum transport and the necessary tools to understand the thesis. By transport, we mean coherent transport of electrons in between perfect electrodes. We describe an idealized situation which does not take into account electron-electron interactions or dissipation. We start by solving a simple system for pedagogical reasons in Sec. 2.1, a free particle confined in a waveguide. This allows us to introduce the concept of modes and momenta. Most of the rest of the chapter is dedicated to the implementation of numerical techniques to simulate quantum transport. To that end, we construct the discretized version of a one-dimensional Hamiltonian in Sec. 2.2 and introduce the tight-binding models, the cornerstone of numerical recipes. Section 2.3 is devoted to the formulation of the lead problem, a general version of the waveguide problem.

In the next sections we consider a more general problem, a central region connected to electrodes (whose eigenmodes are computed in Sec. 2.3). The two following sections introduce two equivalent formalisms, the scattering matrix approach in Sec. 2.4 and the Green's function in Sec. 2.5. Both sections are accompanied by two subsections, sections 2.4.4 and 2.5.4, that provide a mathematical formulation of the scattering problem that can readily be implemented on a computer. These subsections also introduce the necessary elements to prove the equivalence of the scattering and the Green's function formalisms, the so-called Fisher-Lee relations. Both subsections are very technical and can be skipped without hindering the understanding of the thesis. We conclude this part with a derivation of the Fisher-lee relation in Sec. 2.6 for tight-binding models, that gives explicit relations between the scattering matrix and the Green's function, hence demonstrating the equivalence of both approaches.

2.1 The wave guide problem

As a first simple example, we study a quasi-1D waveguide, the simplest form of a lead, such that electrons are confined in the y - and z -directions, and move freely in the x -direction. We assume that the waveguide is free of impurities.

The starting point of the derivation in this thesis is the time-independent Schrödinger equation, a wave equation which reads for a free particle,

$$-\frac{\hbar^2}{2m}\Delta\psi(\mathbf{r}) = E\psi(\mathbf{r}). \quad (2.1)$$

Our electron is subject to confinement, which we impose with boundary conditions on the wavefunction, $\psi(0, y) = \psi(L, y) = 0$. We also assume that the electron is situated in the (x, y) plane, i.e. $z = 0$. Solving this simple example illustrates some of the central concepts to the thesis. The system is invariant in the x -direction, therefore solutions of Eq. (2.1) are plane waves that respects the boundary condition,

$$\psi(x, y) = e^{ik_x x} \sin(k_y y), \quad (2.2)$$

where we introduce the continuous momenta k_x and the discrete momenta k_y that correspond to the transverse mode. Since the system is infinite in the x -direction, k_x is a real number taking continuous values ranging in $[-\pi, \pi]$. On the other hand, the momenta k_y can only take discrete values that respects the boundary conditions, i.e. $k_y = \frac{n\pi}{L}$ where n is an integer that labels the solution. The energy is given by $E = (k_x^2 + k_y^2)\frac{\hbar^2}{2m}$, so that the possible values of k_y are bounded by the energy, $k_y^2 < \frac{2m}{\hbar^2}E$. The number of possible solutions increases with the energy, an important feature that is also true for more complex waveguides. The solutions can be labeled with n and are referred to as modes of the lead.

If k_x had an imaginary part in Eq. (2.2), the wavefunction would be diverging exponentially in one direction. However, k_x can have a non zero imaginary part in a semi-infinite lead, for instance $\Im m k_x > 0$ with an electrode that exists only for $x > 0$ (i.e. because of the new boundary condition $\psi(x, y) = 0$ for $x < 0$). This state is decaying exponentially away from the boundary,

$$|\psi(x, y)| \sim e^{-\Im m(k_x)x}. \quad (2.3)$$

We call these states evanescent, while the states with real k_x are the propagating states. In Chap. 3 we study bound states, a type of states that are a linear combination of evanescent modes.

In the quantum transport field, electrons in solid are not free as they are subject to a potential $U(\mathbf{r})$ arising from the crystal, from impurities or from

the environment, so that Eq. (2.1) equation reads

$$\left(-\frac{\hbar^2}{2m}\Delta + U(\mathbf{r})\right)\psi(\mathbf{r}) = E\psi(\mathbf{r}), \quad (2.4)$$

where $\mathbf{r} = (x, y, z)$. The potential $U(\mathbf{r})$ is a consequence of the nucleus and/or the core electrons of the solid. In the (finite) scattering region, the potential $U(\mathbf{r})$ suffers no restriction. The leads are made of a unit cell that repeats periodically in one direction so that the potential arising from the lattice satisfy $U(\mathbf{r}+a) = U(\mathbf{r})$, where a is equal to the length of the unit cell. The rest of the chapter is dedicated to methods that can solve this problem for an arbitrary scattering region connected to electrodes.

In the second part of this thesis, we will study mostly translationally invariant systems (MTIS). These systems are constructed from translationally invariant systems (TIS), whose potential satisfies $U(\mathbf{r} + \mathbf{R}) = U(\mathbf{r})$, where \mathbf{R} is any Bravais vector of the lattice. The difference with usual leads is that the TIS are now invariant by translation in several directions. Mostly translationally invariant systems are a larger class of systems that satisfy this condition on all but a finite set of points. The formal introduction and definition is given in Sec. 2.5.

2.2 Discretization of a one-dimensional Hamiltonian

Most numerical techniques dedicated to find solutions of Eq. (2.4) introduce some type of finite differences. In this section we derive a discretized version of a real-space 1D Hamiltonian,

$$\hat{H}_{1D} = \left(-\frac{\hbar^2}{2m}\Delta + U(x)\right)\psi(x). \quad (2.5)$$

The discretized Hamiltonian is written as a matrix, such that its eigenstates are solutions of \hat{H}_{1D} . In a first step we approximate the Laplacian operator, simply using a three points scheme. The action of the derivative in the x -direction is expressed as

$$\partial_x^2\psi(x) = \frac{1}{a^2}(\psi(x+a) + \psi(x-a) - 2\psi(x)) + \mathcal{O}(a^4) \quad (2.6)$$

where a is the lattice constant, a finite distance small enough so that the error in the approximate derivative is small enough. In higher dimensions, a lattice constant is defined in each direction, but the principle is similar.

The lattice parameter length depends a lot on the system, it should be at maximum of the order of the smallest length scale. For instance in graphene,

cell (of 5 sites in each lead in Fig. 1.1) that is repeated in a periodic fashion to infinity.

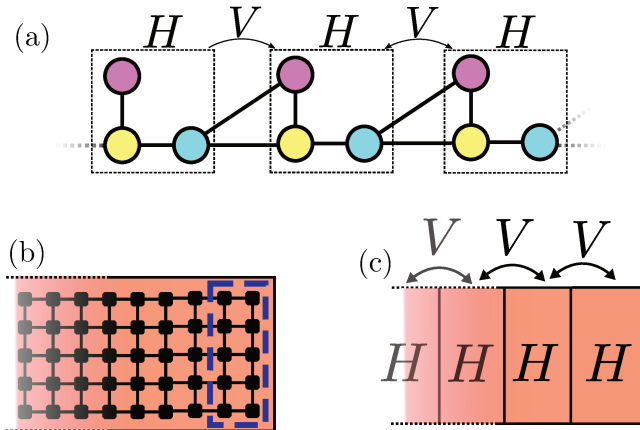


Figure 2.1: Isolated infinite leads. (a) A generic lead is represented with three similar unit cells (dashed boxes) containing three orbitals each. The unit cell is repeated to infinity. (b) The isolated semi-infinite lead from Fig. 1.1, where the dashed blue line includes a unit cell. (c) Same semi-infinite lead where the onsite and hopping matrices H and V are explicitly shown.

To compute the eigenmodes of that system, we implement a numerical routine that can compute the modes of a lead described by complex tight-binding systems. However, one cannot directly solve Eq. (2.8) for the lead problem. Indeed, the electrodes are mathematically described as semi-infinite waveguides, hence the corresponding Hamiltonian is semi-infinite. In this section, using the translational invariance of the lead, the calculations of its eigenmodes is formulated as a *finite* generalized eigenproblem. To that end, we first express the discretized Hamiltonian of a quasi 1d lead. Then the lead eigenmodes are expanded as a combination of plane waves.

For a translationally invariant system, the potential $U(x)$ of the Hamiltonian in Eq. (2.4) satisfies $U(x+a) = U(x)$. The only difference for a semi-infinite lead is that the Hamiltonian is truncated such that $\hat{H}_{1D}(x) = 0$ for $x < 0$.

Using the result of the previous section renders us with

$$\hat{H}_{\text{lead}} = \begin{pmatrix} \ddots & \ddots & \ddots & & & & \\ & V & H & V^\dagger & & & \\ & & V & H & V^\dagger & & \\ & & & V & H & V^\dagger & \\ & & & & \ddots & \ddots & \ddots \end{pmatrix}, \quad (2.11)$$

which is similar to Eq. (2.11) except that all subblocks are similar due to translational invariance. In the previous equation, the matrix H , called the onsite matrix, correspond to the Hamiltonian of one unit cell and the other matrix V is called the hopping matrix. These matrices are of size $N_t \times N_t$, where N_t is the number of orbitals contained in each site. It seems that the Hamiltonian in Eq. (2.11) is not suited to describe semi-infinite electrodes as it modelizes an infinite lead. However, the truncation of the Hamiltonian in a semi-infinite one only affects the modes by including evanescent solutions as in the waveguide case. Note that several physical leads can always be described by one single effective lead, a fact that simplifies notations for the future scattering problem.

2.3.1 The mode equation

In this subsection we formulate a finite set of equations that gives the eigenvectors of the translationally invariant Hamiltonian from Eq. (2.11) using Bloch theorem. This theorem is the corner stone of band theory, and greatly simplifies the study of electrons confined in periodic potentials. Compared to the free electron case, constraining the electrons to a lattice may seem like an substantial constraint, but a surprising result of the Bloch theorem is that the electron wavefunction is still modulated by a plane wave, like in Sec. 2.1.

In the case of a translationally invariant potential $U(x)$, the eigenstates $\psi(x)$ of an Hamiltonian can be decomposed into the product of a phase and a wavefunction with the same periodicity as the lattice,

$$\psi_k(x) = \phi_k(x)e^{ikx}. \quad (2.12)$$

A proof of this theorem can be found in Ref. 18. This introduces the quasimomentum k (which can be generalized in several dimensions, $\mathbf{k} = (k_x, k_y, k_z)$), where k takes continuous (discrete) values in $[-\pi, \pi]$ for infinite (finite) systems. This theorem is central to the second part of the thesis, as one of the algorithms simulate systems that are invariant by translation in several directions.

Let us apply this theorem to an eigenvector $\hat{\psi}$ of the discretized infinite lead Hamiltonian in Eq. (2.11)

$$\hat{H}_{\text{lead}}\hat{\psi} = E\hat{\psi}. \quad (2.13)$$

which can be expressed with sub-vectors ψ_x of length N_t

$$\hat{\psi} = \begin{pmatrix} \vdots \\ \psi_{-1} \\ \psi_0 \\ \psi_1 \\ \vdots \end{pmatrix}. \quad (2.14)$$

These subvectors are solutions of

$$(H - E)\psi_x + V\psi_{x-1} + V^\dagger\psi_{x+1} = 0. \quad (2.15)$$

These wavefunctions obey Bloch theorem, and we obtain the mode equation, one of the central equation of this thesis,

$$(H - E)\phi\lambda^x + V\phi\lambda^{x-1} + V^\dagger\phi\lambda^{x+1} = 0, \quad (2.16)$$

with $\lambda = e^{ik}$. This simplifies to

$$(H - E)\phi + V\phi\lambda^{-1} + V^\dagger\phi\lambda = 0. \quad (2.17)$$

For compactness, we introduce the Bloch Hamiltonian,

$$\mathcal{H}(k) \equiv H + V/\lambda + V^\dagger\lambda. \quad (2.18)$$

Equation (2.17) can be solved in two ways, either looking for E at a given k , or calculating the different possible k for a fixed E . In this thesis, we will only solve the latter: at a given energy E , we look for the real or complex momentums k that satisfy Eq. (2.17).

2.3.2 Solutions to the mode equation (2.17)

To solve the quadratic eigenproblem of Eq. (2.17), notice that it can be recast to the following equivalent generalized eigenproblem,

$$\begin{pmatrix} -V & 0 \\ 0 & 1 \end{pmatrix} \begin{pmatrix} \phi \\ \xi \end{pmatrix} = \lambda \begin{pmatrix} H - E & V^\dagger \\ 1 & 0 \end{pmatrix} \begin{pmatrix} \phi \\ \xi \end{pmatrix} \quad (2.19)$$

with $\xi = \lambda\phi$. If the hopping matrix V is full rank, then the previous equation can be written as a standard eigenvalue problem,

$$\frac{1}{\lambda} \begin{pmatrix} \phi \\ \xi \end{pmatrix} = \begin{pmatrix} -V^{-1}(H - E) & -V^{-1}V^\dagger \\ 1 & 0 \end{pmatrix} \begin{pmatrix} \phi \\ \xi \end{pmatrix}. \quad (2.20)$$

Notice that it is common to have non-invertible hopping matrices, examples include graphene with first neighbor hoppings, or the three orbital model

of Fig. 2.1a. From any tight-binding model for the lead, one can then solve equations (2.19) and (2.20) using standard libraries like `scipy`^[19] or `numpy`^[20]. Stabilization of this eigenproblem is discussed in Ref. 21.

If H is a $N_t \times N_t$ matrix, then the eigenproblems (2.19) and (2.20) have $2N_t$ (including the degeneracies) solutions. Hereafter we suppose we know the different solutions of the eigenproblem, which can be classified in three categories according to the value of $|\lambda|$.

Propagating modes: these are the solutions such that $|\lambda| = 1$, that can be splitted into two categories. The outgoing (+) ones with a positive velocity and the incoming (−) ones with negative velocity, which is given by

$$v(k) \equiv \frac{\partial E}{\partial k} \quad (2.21)$$

$$= i\phi^\dagger(V^\dagger\lambda - V\lambda)\phi. \quad (2.22)$$

There is an equal number of incoming and outgoing propagating modes; which we call N_p . The reason comes from the 2π -periodicity and the continuity of the bands $E(k)$. Any given energy E must cross each band an even number of times, with half of the crossings at a positive slope and the other half at a negative slope, hence we have an equal number of modes with positive and negative velocities.

Evanescent modes: these are solutions with $0 < |\lambda| < 1$ and $|\lambda| > 1$, so that any wavefunction made of evanescent modes

$$\psi(x) = \sum_e \phi_e \lambda_e^x \quad (2.23)$$

is not normalizable in our infinite lead since $|\lambda_e|^x$ diverges at $x = \infty$ or $x = -\infty$. Even though these solutions seem unphysical at first glance, they are important in both parts of the thesis. In part II, the wavefunction of a bound state is expanded on the evanescent basis. In part III they also give a contribution in the Green's function calculation, e.g. outside of the bandwidth, the response to an excitation comes in the form of decaying waves.

The number of outgoing and incoming evanescent modes are also equal^[22]. Indeed, hermitian conjugate of Eq. (2.17)) holds

$$\phi^\dagger \left[(H - E) + V^\dagger \lambda^{-1*} + V\lambda^* \right] = 0. \quad (2.24)$$

There also exists a right eigenvector ϕ' of Eq. (2.24) associated with the same eigenvalue

$$\left[(H - E) + V^\dagger \lambda^{-1*} + V\lambda^* \right] \phi' = 0. \quad (2.25)$$

Equation (2.25) implies that for each solution of Eq. (2.17) with eigenvalue λ , there is an associated solution with eigenvalue λ^{-1*} .

Kernel modes: the last category of solutions are not physical and satisfy $\lambda = 0$ or $\lambda = \infty$. If V is not invertible, then there is -at least- one eigenvector ϕ with $\lambda = 0$ that satisfies $V\phi = 0$ and is therefore a trivial solution of Eq. (2.17). The solution $\lambda = \infty$ can be understood if we rewrite Eq. (2.17) as

$$(H - E + V\lambda' + V^\dagger/\lambda')\phi = 0 \quad (2.26)$$

with $\lambda' = 1/\lambda$, then any vector such that $V^\dagger\phi = 0$ with an eigenvalue $\lambda' = 0$ is a trivial solution to the previous equation. Using an abuse of notation, these solutions are designated by $\lambda = \infty$. There is N_o solutions with $\lambda = 0$ and again an equal number of solutions with $\lambda = \infty$. This equality comes from the equal ranks of V and V^\dagger .

To finish the section, we introduce some notations to compactify equations. The matrix Φ whose columns correspond to the eigenstates ϕ is

$$[\Phi]_{ij} = (\phi_j)_i. \quad (2.27)$$

We can then introduce the submatrix Φ_p (Φ_{p+} , Φ_e , Φ_o, \dots) of Φ that contains only the columns of the propagating (outgoing propagating, evanescent, kernel...) modes. See table 2.1 for a list of the possible matrices. We also introduce the diagonal matrices Λ which contains the eigenvalues λ , i.e.

$$[\Lambda]_{ii} = \lambda_i. \quad (2.28)$$

Similarly, we define Λ_p (Λ_{p+} , Λ_e, \dots) as the matrix that contains only the propagating (outgoing propagating, evanescent...) modes. We have the equalities $N_t = N_p + N_e = N_{\bar{t}} + N_o$ and $N_e = N_{\bar{e}} + N_o$. Using the new notations Eq. (2.17) reads

$$((H - E)\Lambda + V + V^\dagger\Lambda^2)\Phi = 0. \quad (2.29)$$

2.4 Scattering formalism

Having computed the eigenmodes of a lead, we turn to a more complex but also richer object of study, a device (modeled by a scattering region) attached to one or several electrodes (modeled by the leads of the previous section).^[12,23] Many physical devices can be described by this simple picture, such as a quantum point contacts^[24], a quantum Hall bar or a graphene nanoribbon^[25].

In this section we develop tools to relate how an incoming electron arriving into the scattering region in the form of a plane wave from a lead is

Symbol	Modes, direction	Identification
Φ_t	all	any solution
$\Phi_{\bar{t}+}$	all outgoing but kernel modes	$\lambda \neq 0, \infty$
Φ_p	propagating	$ \lambda = 1$
Φ_{p+}	propagating, outgoing	$ \lambda = 1$ and $v(k) > 0$
Φ_{p-}	propagating, incoming	$ \lambda = 1$ and $v(k) < 0$
Φ_{e+}	evanescent, outgoing	$ \lambda < 1$
$\Phi_{\bar{e}+}$	evanescent, outgoing, no kernel	$0 < \lambda < 1$
Φ_{e-}	evanescent, incoming	$ \lambda > 1$
Φ_{o+}	kernel, “outgoing”	$\lambda = 0$

Table 2.1: Summary of the different classifications of the leads modes. The letter subscript labels the modes, e for evanescent, p for propagating and o for the super-evanescent modes. The $+$ or $-$ sign indicates the direction of propagation of the modes. The matrices $\Lambda_t, \Lambda_{\bar{t}+} \dots$ follow the same classification.

scattered into the different leads. Understanding the behavior of the incoming and outgoing waves into the leads requires the knowledge about the lead eigenmodes but also depends on the specifications of the scattering region. Indeed, the scattering region material, shape or the eventual defects act as scatterers for electrons. The conductance of the nanostructure is therefore affected by an enormous number of parameters. More precisely, the number of elements of a microscopic Hamiltonian that describes the central region grows as the volume of it. Fortunately, as long as the electron scattering events are only elastic, the transport properties are fully characterized by the *scattering matrix* at each energy, whose size grows only as the contact surface between the electrodes and the central region. We first review some properties of this matrix in Sec. 2.4.2, e.g. how this matrix gives a direct access to the transmissions probabilities between the different channels of the system. We then relate this matrix to the conductance of a system using the Landauer formula in Sec. 2.4.3. The last subsection 2.4.4 derives a numerical method to compute the scattering matrix itself.

2.4.1 The scattering matrix definition

Even though the expression of the wave function into the scattering region can be nontrivial, its form into the leads (far enough to neglect the evanescent modes) consists in a plane wave superposition because of Bloch theorem.

In that section we assume that we know the eigenmodes of each lead, having calculated them using Eq. (2.19) or by other means. The wavefunction

in a lead can be expanded in the eigenmode basis,

$$\psi(x) = \Phi_{t+}(\Lambda_{t+})^x q_{t+} + \Phi_{p-}(\Lambda_{p-})^x q_{p-}, \quad (2.30)$$

where we introduced the vectors q_{t+} and q_{p-} of respectively N_t and N_p coefficients for the expansion on the lead incoming and outgoing modes.

At each energy, we define a scattering matrix that captures the physics of the central device to relate the incoming coefficients q_{t+} to the outgoing ones q_{p-} ,

$$q_{t+} = S_{tp} q_{p-}. \quad (2.31)$$

Equation (2.31) implicitly assumes that there is no inelastic scattering process happening in the scattering region. Indeed, the leads eigenmodes depend on energy, so that the wavefunction in Eq. (2.30) is valid only if the energy of the outgoing modes is the same as the incoming modes. This assumption is crucial, otherwise a simple matrix would not be enough to describe the scattering events, and an integral over the energy of scattering states would be necessary^[26]. Elastic scattering is usually present under certain circumstances, typically at low temperature (so that the phonons are absent), low voltage and if a screening of the Coulomb interaction is present.

The usual definition of the scattering matrix^[12,23] is slightly different, as it does not contain the outgoings evanescent modes, i.e. the usual definition discards the last N_e columns of S_{tp} . From a practical point of view, the scattering matrix is used to calculate the conductance of a device, and the current transmitted into the leads depends only on the propagating modes. One can prove different properties of the scattering matrix without explicitly computing the evanescent modes. However, in practice, the calculation of the matrix must account for the complete basis of the modes to be correct. Therefore, Sec. 2.4.2 will use the standard definition of the scattering matrix (the one without evanescent modes) to derive some of its basic properties, while the derivation of a practical method to compute the scattering matrix done in Sec. 2.4.4 relies on the full scattering matrix.

2.4.2 Properties of the scattering matrix

A typical nanoelectronic system is pictured in Fig. 1.1, with a device located in the center and three electrodes connected to the macroscopic world. The scattering region is a microscopic system (a size varying from a quantum dot to a tens of μm) which has quantized energy levels. Assembling the different parts mixes most of the discrete energy levels present in the scattering region with the continuum of states from the lead. There exists states that do not hybridize with the continuum, the so-called bound states, which keep a discrete energy. Due to their finite spatial extent, they do not contribute to transport so we discard them for that section. Their properties are extensively described in part II.

In the special case of a nanostructure connected to 2 leads, the scattering matrix has the following block structure

$$S = \begin{pmatrix} r & t \\ t' & r' \end{pmatrix}. \quad (2.32)$$

The blocks (r, r') and (t, t') are respectively known as the *reflection* matrices and the *transmission* matrices. The scattering matrix coefficients have a rather intuitive interpretation. The probability of the process "an electron comes in channel n and is reflected in the same lead in channel m " is given by the coefficient $|r_{mn}|^2$. Likewise, the coefficients t_{mn} give the amplitude of being transmitted from channel n to channel m . Therefore, current conservation implies

$$\sum_m^{N_t} |r_{mn}|^2 + \sum_m^{N'_t} |t_{mn}|^2 = 1, \quad (2.33)$$

since an electron coming in channel n is either reflected or transmitted in one of the existing channels. This ensures the unitarity of the scattering matrix

$$\hat{S}^\dagger \hat{S} = \mathbb{1}. \quad (2.34)$$

This relation is true for an arbitrary number of leads, if probability currents are normalized to unity.

2.4.3 From the scattering matrix to conductance

The scattering matrix gives a direct access to the transmission and reflection amplitudes. However, these quantities are hard to probe experimentally, so we introduce the Landauer formula that calculates the current flowing between two leads. Each lead is assumed to be at equilibrium and with small (compared to the thermal and Fermi energies) voltage differences in between them. It formally reads

$$I = \frac{e}{h} \int dE \sum_{m,n=1}^{N_p} |t_{mn}(E)|^2 [f_L(E) - f_R(E)], \quad (2.35)$$

where $f_{L/R}(E)$ is the Fermi function of lead L/R . It is given by $f_{L/R}(E) = 1/(e^{(E-\mu_{L/R})/(k_B\Theta_{L/R})} + 1)$, with $\Theta_{L/R}$ the temperature in each lead and $\mu_{L/R}$ the chemical potential. The sum is only taken on the propagating modes, as the evanescent modes do not carry current. The right hand side of Eq. (2.35) essentially sums up the transmission probabilities in each channel, ponderated by the filling difference in between the leads. Throughout

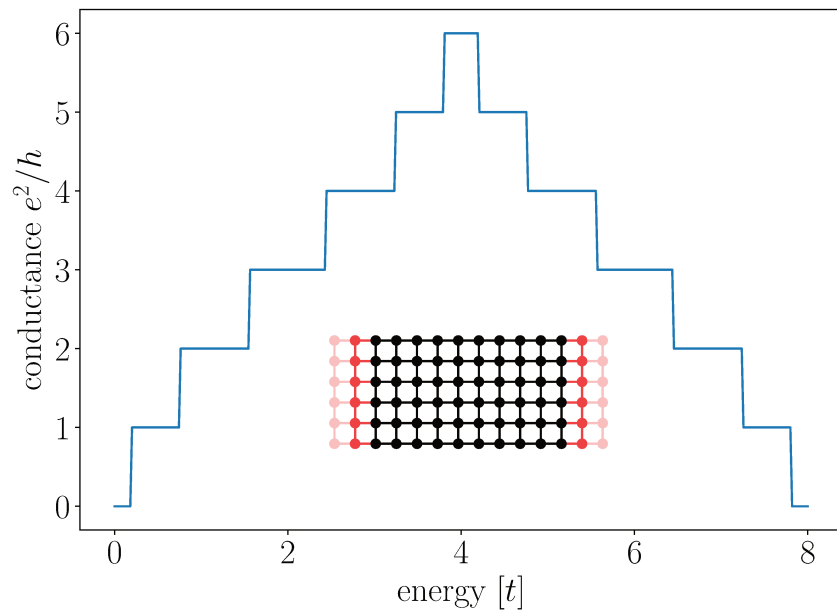


Figure 2.2: Conductance quantization of an infinite nanowire as a function of the energy. The units are normalized to the conductance quantum and to the hopping parameter t . The inset shows the system and the lattice of the tight-binding model. The tight-binding model is defined with $U = 0$ and $t = 1$ in Eq. (2.5).

the thesis we assume the temperature to be zero in all regions, which simplifies the Landauer formula. The Fermi function then becomes a heavyside function, equal to 1 below the Fermi energy and 0 otherwise. Introducing the bias voltage V_b such that $\mu_{L/R} = E_F \pm eV_b$, the integrand in Eq. (2.35) is then only non-zero in $[E_F - eV_b, E_F + eV_b]$. If we further assume that the transmission $|t_{mn}(E)|$ does not vary for small variations around E_F , then the current can be expressed as

$$I = \frac{e^2}{h} V_b \sum_{m,n} |t_{mn}|^2. \quad (2.36)$$

The differential conductance $g = dI/dV_b$ is then given in compact matrix notations by

$$g = \frac{e^2}{h} \text{Tr}(tt^\dagger(E_F)). \quad (2.37)$$

Here g is the conductance of the system, and E_F the Fermi energy. This formula gives a relation between a macroscopic quantity (the conductance) and the transmission matrices that are deduced from the microscopic model. A perhaps even more important point is that this formula gives a simple explanation for the conductance quantum plotted in Fig. 2.2. Indeed, if there is no scatterers inside the scattering region all opened channels are perfectly transmitted¹, then the matrix tt^\dagger is simply the identity in the space of open channels. This formula therefore predicts that even a scatterer-free device has a finite conductance which shows steps of e^2/h ($2e^2/h$ if there is spin degeneracy) each time a transmission channel is opened. A result first observed in Ref. 27.

The conductance plotted in Fig. 2.2 also illustrates a limit of the discretized models, already mentioned in Sec. 2.2. In a perfect waveguide, Sec. 2.1 it was shown that the number of modes increases indefinitely with the energy. Therefore, the conductance of our discretized wire, which is simply proportional to the number of modes, decreases for energies larger than $4t$. This is a general feature, the tight-binding models are only valid for small energies. Note that this is not a limitation in our case, since we assume a low bias so that the interactions are treated on the mean-field level.

2.4.4 The scattering problem as a set of linear equations

There is many dedicated numerical techniques that simulate the conductance of nanoelectronics systems, for instance based on the non-equilibrium Green's function formalism^[10,11]. In this section we derive the scattering matrix as the solution to a linear system, similar to the approach used in Kwant^[7,21].

¹One may argue that this is not really a “scattering region” anymore

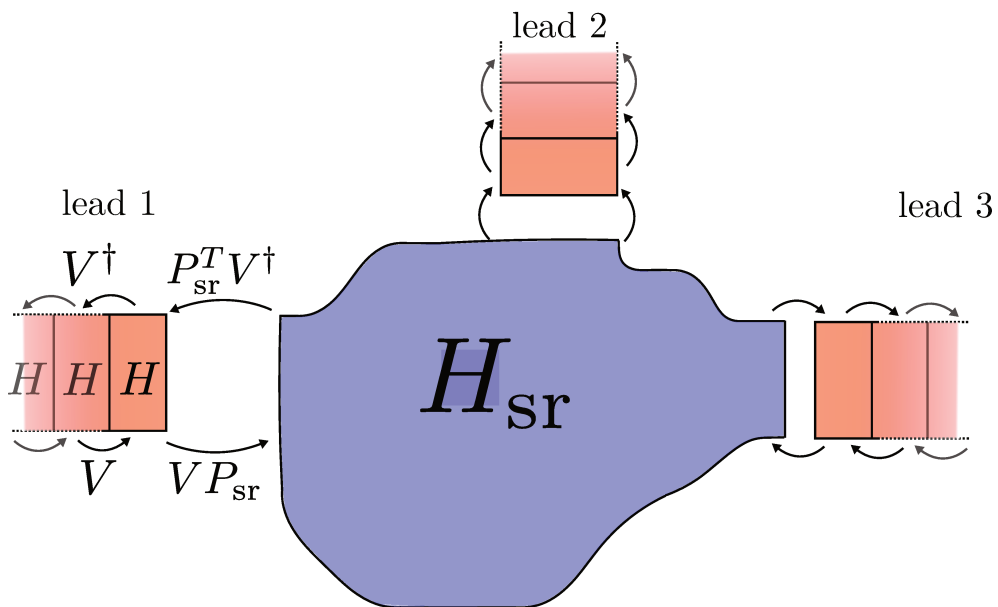


Figure 2.3: Modelization of a nanoelectronic device. The Hamiltonian H_{sr} describes the central region (in blue) of the device. The leads are made of unit cells (in red), which repeats to infinity. In lead 1, the onsite and hopping matrices are explicitly written, as well as the hopping matrix $P_{\text{sr}}V$ that connects the lead to the scattering region. Each lead can have a different unit cell.

Our typical system plotted in Fig. 1.1 can be split in several parts, a scattering region and several leads as in Fig. 2.3. Hereafter, we suppose that there is only one lead². The different parts are described by the Hamiltonian of a scattering region \hat{H}_{sr} , the Hamiltonian of the lead \hat{H}_{lead} and the connexion in between the scattering region and the leads \hat{V} , so that the total Hamiltonian reads

$$\hat{H}_{\text{tot}} = \hat{H}_{\text{sr}} + \hat{H}_{\text{lead}} + \hat{V} + \hat{V}^\dagger. \quad (2.38)$$

The first unit cell of the lead can be included in the scattering region, so that the hopping \hat{V} that connects the central region and the electrode is equal to the hopping in between the different cells of the lead. The lead is semi-infinite and invariant by translation, so that the hamiltonian can be

²As aforementioned, several leads that can be merged into one bigger effective lead.

written as

$$\hat{H}_{\text{lead}} = \begin{pmatrix} H & V^\dagger & & \\ V & H & V^\dagger & \\ & V & H & \ddots \\ & & \ddots & \ddots \end{pmatrix}, \quad (2.39)$$

where H and V are the onsite and hopping matrices introduced in the Sec. 2.3, identical in each unit cell. The previous equation is very similar to Eq. (2.11), except that the lead is semi-infinite instead of infinite. This condition allows for the existence of outgoing evanescent modes on the boundaries of the lead. Indeed, these modes are now normalizable due to their exponential decay, that is, $\sum_{x=0}^{\infty} |\phi_e(x)| \simeq \sum_{x=0}^{\infty} e^{-\kappa x} < \infty$ where κ is a real number.

The leads are assumed to be quasi-1d, i.e. they are semi-infinite in one direction (the x -direction) and confined in the others (the y - and z -directions). In the case of a single lead, it is straightforward to write the total Hamiltonian of Eq.(2.38) as

$$\hat{H}_{\text{tot}} = \begin{pmatrix} H_{\text{sr}} & P_{\text{sr}}^T V^\dagger & & \\ V P_{\text{sr}} & H & V^\dagger & \\ & V & H & \ddots \\ & & \ddots & \ddots \end{pmatrix}. \quad (2.40)$$

where we introduce the connexion matrix P_{sr} . P_{sr} is a rectangular matrix with N_t lines, that labels the sites in the unit cells of the leads, and N_{sr} columns that labels the sites of the scattering region. The matrix entries satisfy

$$[P_{\text{sr}}]_{i,j} = 1, \quad (2.41)$$

if the site i from the lead is connected to the site j in the scattering region and 0 otherwise. In Eq. (2.40) we assumed the Hamiltonian H_{sr} encompasses the first unit cell of the leads so that its connexion to them is the hopping matrix V .

The Schrödinger equation for this problem reads

$$\begin{pmatrix} H_{\text{sr}} & P_{\text{sr}}^T V^\dagger & & \\ V P_{\text{sr}} & H & V^\dagger & \\ & V & H & \ddots \\ & & \ddots & \ddots \end{pmatrix} \begin{pmatrix} \psi_{\text{sr}} \\ \psi(1) \\ \psi(2) \\ \vdots \end{pmatrix} = E \begin{pmatrix} \psi_{\text{sr}} \\ \psi(1) \\ \psi(2) \\ \vdots \end{pmatrix}. \quad (2.42)$$

This expression cannot be computed numerically as the matrices involved are infinite, so in the rest of the section we derive analytically a practical and general formulation for the scattering problem. To that end, we express

the wavefunction in the lead ($\psi(1), \psi(2) \dots$) as a linear combination of the lead eigenmodes computed in the last section. The general form for the wavefunction reads

$$\psi(x) = \begin{cases} \psi_{\text{sr}} & \text{for } x = 0 \\ \Phi_{\text{t}+}(\Lambda_{\text{t}+})^x q_{\text{t}+} + \Phi_{\text{p}-}(\Lambda_{\text{p}-})^x q_{\text{p}-} & \text{for } x > 0 \end{cases}$$

Here x labels the cell of the lead. As a convention, the first unit cell (the one connected to the scattering region) is labeled by one and the label increases as we look at cells further away from the central region. As mentioned in the previous section, we include a generalized scattering matrix which also contains the outgoing scattering modes, $q_{\text{t}+} = S_{\text{tp}} q_{\text{p}-}$. The generalized scattering matrix is a $N_{\text{t}} \times N_{\text{p}}$ rectangular matrix, so that the usual scattering matrix is recovered by taking the first N_{p} columns of the matrix. We introduce the matrix Ψ_{sr} such that its columns correspond to the different solutions ψ_{sr} corresponding to the different incoming propagating modes. Then Eq. (2.42) combined with the mode equation (Eq. (2.29)) gives the general formulation of the scattering problem

$$\begin{pmatrix} H_{\text{sr}} - E & P_{\text{sr}}^T V^\dagger \Phi_{\text{t}+} \Lambda_{\text{t}+} \\ V P_{\text{sr}} & -V \Phi_{\text{t}+} \end{pmatrix} \begin{pmatrix} \Psi_{\text{sr}} \\ S_{\text{tp}} \end{pmatrix} = \begin{pmatrix} -P_{\text{sr}}^T V^\dagger \Phi_{\text{p}-} \Lambda_{\text{p}-} \\ V \Phi_{\text{p}-} \end{pmatrix}. \quad (2.43)$$

The right hand side contains the incoming modes and can be interpreted as a source or an excitation, and the scattering matrix is the response to that excitation. The scattering problem is now reduced to a set of linear equations, and is ready to be implemented and solved using standard routines^[19,20]. In the case of non-invertible hopping matrix V , the last columns of the left hand side of Eq. (2.43) corresponding to the kernel ($\lambda_\alpha = 0$) modes can be discarded. Indeed the matrix $\Phi_{\text{o}+}$ lies on the kernel of V so that the discarded columns are filled with zeros.

In practise, the left hand side is usually very sparse for big systems. Indeed, the total size of H_{sr} grows as N_{sr}^2 , where N_{sr} is the numbers of sites in the scattering region, while the number of non-zero elements scales as $2(d+1)N_{\text{sr}}$, where d is the number of hoppings between each site. The vectors Φ are the only non sparse matrix of the linear system, however as the number of elements in the lead scales linearly with the system size (instead of quadratically for the scattering region), they only represent a fraction of the elements in Eq. (2.43).

2.5 Green's function formalism

Even though the scattering matrix developed in Sec. 2.4 completely characterizes the transport, there is another equivalent (for non-interacting transport) formalism based on the Green's functions. Depending on the situations, the Green's function formalism can be more suited for some numerical

calculations than the scattering matrix approach. The scattering formalism was introduced first in the thesis because of its intuitive approach. Indeed, the scattering matrix approach provides a natural explanation for the conductance steps and gives a direct access to the transmission amplitudes. On the other hand, the physical understanding of the Green's function formalism is less intuitive than the S-matrix. A very important advantage of the Green's function is that it allows one to access local quantities at any point. This is a crucial property for the second part of the thesis.

As for the scattering matrix, we introduce the Green's function definition, properties and a formulation of the Green's function problem in this section. Specifically, Sec. 2.5.1 gives the Green's function definition and a physical understanding of it. Sec. 2.5.2 displays a few properties of the Green's function that are used throughout the thesis. Sec. 2.5.3 introduces the glueing sequence, a very important set of equations that allows one to add perturbations to the Green's function. The last section 2.5.4 derives a linear set of equations that allows one to calculate the Green's function and the self-energy of an arbitrary scattering region. However, this section is very technical, and should be skipped by non-specialists. Its understanding is not necessary for the rest of the thesis, except for the demonstration of the Fisher-lee relation in Sec. 2.6.

2.5.1 Definition and interpretation

Conceptually, the S-matrix elements describe the response in one channel to an excitation in another channel. The Green's function is a concept that describe the response at one point to an excitation in any other point, so this can be considered as a more powerful formalism. More specifically, we consider only the *retarded* Green's function in this thesis, which contains the causal response due to the excitation. To use the parallel with the S-matrix again, the response to the incoming wave is only made of outgoing waves. Similarly, the retarded Green's function describes waves that travel outward from the point of excitation. That is, the retarded Green's function of a 1D wire with a constant potential is proportional to^[12]

$$G^{\text{R}}(x, x') \propto -i \exp(ik|x - x'|). \quad (2.44)$$

The advanced Green's function would be proportional to $\exp(-ik|x - x'|)$. The superscript R will be dropped in the rest of the thesis as we *always* refer to the retarded Green's function.

A more general but still intuitive way of understanding the Green's function is to introduce it using the time evolution operator. The formal solution to the time dependent Schrödinger equation for a time-independent Hamil-

tonian is given by the time evolution operator,

$$\hat{U}(t) = e^{-i\hat{H}t}, \quad (2.45)$$

which acts on the a state $\psi(t)$ as

$$\hat{U}(t)\psi(0) = \psi(t) \quad (2.46)$$

The Green's function, also called the propagator, is defined as

$$G(x, x', t) = -i \langle x' | e^{-iHt} | x \rangle \theta(t), \quad (2.47)$$

where $\theta(t)$ is the heavyside function. The interpretation of the previous expression gives meaning to the name propagator. Given a state located in $|x\rangle$ at the $t = 0$, the state evolve according to the time evolution operator, and the left projection gives the amplitude to find the state in $\langle x' |$ at a later time t . The step function ensures that for an excitation done at $t = 0$, the response at earlier times ($t < 0$) is always zero, i.e. we computed the retarded (causal) Green's function.

Doing a Fourier transform of Eq. (2.47) gives the retarded GF (Green's function) in energy domain for a time-independent quadratic Hamiltonian,

$$\hat{G} = \lim_{\eta \rightarrow 0} \frac{1}{E - \hat{H}_{\text{tot}} + i\eta}, \quad (2.48)$$

where the term $i\eta$ can be seen as an absorbent boundary condition. Equivalently, the GF obeys the following equation

$$(E - \hat{H}_{\text{tot}})\hat{G} = \mathbb{1}. \quad (2.49)$$

The only difference between equations (2.48) and (2.49) is that in the latter the retarded Green's function is not the unique solution due to the absence of the infinitesimal term $i\eta$.

2.5.2 Properties of the Green's function

As stated in the beginning of the section we can extract more physical quantities from the Green's function than from the scattering matrix. The main difference is that the Green's function can be computed between any points, instead of the S -matrix that only gives information between channels. It especially contains local quantities in its diagonal, the submatrix $N_t \times N_t$ of $G_{\mathbf{r},\mathbf{r}}(E) = \langle \mathbf{r} | \hat{G}(E) | \mathbf{r} \rangle$. One can then extract quantities from the diagonal elements such as the Local Density of States (LDOS)

$$\rho(\mathbf{r}, E) = -\frac{1}{\pi} \text{Im}(\text{Tr}(G_{\mathbf{r},\mathbf{r}}(E))), \quad (2.50)$$

where Tr represent the trace over all degrees of freedom at site \mathbf{r} . This can be generalized to other type of LDOS, e.g. the LDOS of a single specie of spin (by tracing on all degrees of freedom but the spin).

As mentioned in the introduction and derived formally in the next section, Sec. 2.6, there exists relations in between the scattering matrix and the Green's function elements. These relations can be used to compute handy formulas for the transmissions and reflections in between leads. Skipping the demonstrations, the transmission in between two different leads l and l' reads

$$T_{ll'} = \text{Tr}(\hat{G}\Gamma_l\hat{G}^\dagger\Gamma_{l'}). \quad (2.51)$$

This non-intuitive formula involves the calculation of \hat{G} , the Green's function of the total system, and the quantity Γ_l that plays the role of a current operator. \hat{G} is the Green's function in between leads, i.e. it contains all elements $G_{\mathbf{r},\mathbf{r}'}$ such that \mathbf{r} and \mathbf{r}' are sites respectively situated on leads l and l' . The matrix Γ_l is computed from the self-energies,

$$\Gamma_l = i(\Sigma_l - \Sigma_l^\dagger), \quad (2.52)$$

which are in turn computed using the GF on the boundary of the lead,

$$\Sigma_l = V_l^\dagger G_l V_l. \quad (2.53)$$

In the above definition, G_l is the surface Green's function of the electrode only, while the matrix V_l is the hopping matrix between lead l and the conductor. Similarly, the reflection at a lead is computed as

$$R_l = N_l + \text{Tr}(\Gamma_l\hat{G}\Gamma_l\hat{G}^\dagger) + i(\text{Tr}(\Gamma_l\hat{G}) - \text{Tr}(\Gamma_l\hat{G}^\dagger)). \quad (2.54)$$

where N_l is the number of channels in the leads.

2.5.3 Adding perturbations in the Green's function formalism

One serious advantage of the Green's function approach is the simplicity of equations and the low computational cost necessary to add a perturbation to the system. With the scattering approach, computing the S-matrix after adding a (even small) modification to the Hamiltonian requires to perform the calculation from the beginning. In this section we introduce the Dyson equation, which allows one to compute the Green's function from a perturbed Hamiltonian. In the single electron picture this equation can be solved exactly using basic linear algebra.

Suppose we know the Green's function \hat{g} of a Hamiltonian \hat{H} ,

$$\hat{g} = \frac{1}{E - \hat{H} + i\eta}, \quad (2.55)$$

We then add a perturbation \hat{W} to the Hamiltonian \hat{H} , and wish to compute

$$\hat{G} = \frac{1}{E - (\hat{H} + \hat{W}) + i\eta}, \quad (2.56)$$

without restarting the calculation from scratch. Using this simple equation for two matrices A and B ,

$$\frac{1}{A+B} = \frac{1}{A} - \frac{1}{A}B\frac{1}{A+B}, \quad (2.57)$$

we derive the Dyson equation which express \hat{G} as a function of \hat{g} ,

$$\hat{G} = \hat{g} + \hat{g}\hat{W}\hat{G}. \quad (2.58)$$

To illustrate the previous equation, consider a single impurity placed on site $|0\rangle$ that shifts the energy of w , i.e. $\hat{W} = w|0\rangle\langle 0|$, so that Eq. (2.58) projected on sites \mathbf{r} and \mathbf{r}' reads,

$$G_{\mathbf{r},\mathbf{r}'} = g_{\mathbf{r},\mathbf{r}'} + g_{\mathbf{r},0}wG_{0,\mathbf{r}'}. \quad (2.59)$$

To solve the previous equation, we first need to calculate $G_{0,\mathbf{r}'}$. Writing the Dyson equation between sites 0 and \mathbf{r}' renders us with

$$G_{0,\mathbf{r}'} = g_{0,\mathbf{r}'} + g_{0,0}wG_{0,\mathbf{r}'}, \quad (2.60)$$

$$G_{0,\mathbf{r}'} = (\mathbb{1} - g_{0,0}w)^{-1}g_{0,\mathbf{r}'}. \quad (2.61)$$

Equation (2.61) displays a general feature of the glueing sequence. Solving Eq. (2.58) always start by an inversion. The explicit solution for \hat{G} between any points \mathbf{r} and \mathbf{r}' is

$$G_{\mathbf{r},\mathbf{r}'} = g_{\mathbf{r},\mathbf{r}'} + g_{\mathbf{r},0}w(\mathbb{1} - g_{0,0}w)^{-1}g_{0,\mathbf{r}'}. \quad (2.62)$$

The procedure used to add arbitrary impurities W is called the *glueing sequence*. The previous equation illustrates two features that are general to the glueing sequence. (i) It is independent of the Hamiltonian \hat{H} , that is, the computational cost involved to solve the Dyson equation does not depend on the size of the original system, but only on the number of impurities and time to extract values of \hat{g} . (ii) Changing the value of w does not require to compute additional elements of \hat{g} . Formally, the computational time to compute \hat{G} for many realizations of the disorder does not depend on the time to compute \hat{g} (except for the first step).

Eq. (2.59) has a nice interpretation in terms of paths. For a small perturbation Eq. (2.59) is approximated as

$$G_{\mathbf{r},\mathbf{r}'} \simeq g_{\mathbf{r},\mathbf{r}'} + g_{\mathbf{r},0}wg_{0,\mathbf{r}'}. \quad (2.63)$$

The term $G_{\mathbf{r},\mathbf{r}'}$ gives the amplitude to go from \mathbf{r} to \mathbf{r}' with the impurity. On the right hand side, we sum the amplitude go from \mathbf{r} to \mathbf{r}' in the impurity-free system and the amplitude of passing once through the impurity.

Similarly to an impurity, a lead can be added to a system using the same sets of equations. Consider a system made of two independent parts, a scattering region and a lead. Let us introduce the set S which correspond to points at the boundary of the scattering region and the set of points L in the first unit cell of the lead. We assume that we know the Green's functions of the isolated scattering region at the boundary, g_{SS} , and of the isolated leads in the first unit cell g_{LL} , but not of the connected system. We can use the Dyson equation to obtain the GF of the full system. At the boundary of the scattering region, we get

$$G_{SS} = g_{SS} + g_{SS}V G_{LS}, \quad (2.64)$$

where V is the hopping matrix connecting the scattering region to the lead. Writing the Dyson equation for the term G_{LS} gives a close set of equations

$$G_{LS} = g_{LS}V^\dagger G_{SS}. \quad (2.65)$$

Introducing Eq. (2.65) in Eq. (2.64) gives

$$G_{SS} = g_{SS} + g_{SS}\Sigma G_{SS}, \quad (2.66)$$

where we introduced the self-energy from Eq. (2.53). We can then deduce a way to compute the GF of a finite scattering region due to the leads,

$$G_{sr} = \frac{1}{E - H_{sr} - \sum_l \Sigma_l}, \quad (2.67)$$

where the sum runs on the different leads. Note that Eq. (2.67) requires the knowledge of the lead Green's function, but not on the Green's function in the scattering region. The Green's function of a lead may be determined analytically in some simple cases. In other cases, the Green's function of complex systems can be computed using the tools derived in the following section.

2.5.4 General formulation of the Green's function as a linear problem

In this section we derive a linear set of equations to compute the Green's function of a system composed of a scattering region connected to one or several leads. In this thesis, we do not use this system to compute the Green's function directly, but to prove the equivalence between the Green's function

and the scattering matrix formalisms. This derivation is made in analogy with Sec. 2.4.4, which derives a formulation of the scattering problem.

We are looking to compute the green's function of the Hamiltonian from Eq. (2.40). Let us define $G(j, k)$ as a subblock of the matrix $\hat{G}(E)$, where the indices j and k label the position with the convention that $j = 0$ corresponds to the scattering region and $j > 0$ to unit cells. It is only possible to compute a finite number of elements of the infinite matrix $\hat{G}(E)$, so we will focus on the elements $G(j, 0)$.

We apply equation (2.49) on the subblocks $G_{\text{sr}} \equiv G(0, 0)$ and $G(j, 0)$,

$$[E - H_{\text{sr}}]G_{\text{sr}} - P_{\text{sr}}^T V^\dagger G(1, 0) = 1, \quad (2.68)$$

$$-V P_{\text{sr}} G_{\text{sr}} + [E - H]G(1, 0) - V^\dagger G(2, 0) = 0, \quad (2.69)$$

$$-VG(j-1, 0) + [E - H]G(j, 0) - V^\dagger G(j+1, 0) = 0. \quad (2.70)$$

In the previous expression $G(j, 0)$ labels the GF between j th unit cell of the lead and 0. The label convention is such that the scattering region is labeled as 0, the first unit cell of the lead as 1 and the further cells are labeled with an increasing number as one drives away from the scattering region. Physically the element $G(j, 0)$ is the response in cell j to a perturbation in the scattering region. Since we are only considering the retarded GF, this element of the total Green's function only depends on the outgoing modes,

$$G(j, 0) = \Phi_{t+}(\Lambda_{t+})^j G_{t+}. \quad (2.71)$$

As for the scattering problem, G_{t+} and G_{sr} can be written as the solution to a linear problem,

$$\begin{pmatrix} E - H_{\text{sr}} & -P_{\text{sr}}^T V^\dagger \Phi_{t+} \Lambda_{t+} \\ -V P_{\text{sr}} & V \Phi_{t+} \end{pmatrix} \begin{pmatrix} G_{\text{sr}} \\ G_{t+} \end{pmatrix} = \begin{pmatrix} 1 \\ 0 \end{pmatrix}, \quad (2.72)$$

where we used equations (2.68)-(2.70). This linear system has a similar left hand side but a different right hand side compared to the scattering problem in Eq. (2.43). However it is not so different if one realizes that the right hand side correspond to the excitation, that is to incoming waves for the S-matrix and to a discrete Dirac distribution in this case.

The previous system, can be used to formally derive an expression for the self-energy present in Eq. (2.67). Suppressing the $\lambda_\alpha = 0$ modes from Eq. (2.72) and multiplying the second line by $\Lambda_{t+}^* \Phi_{t+}$ gives

$$\begin{pmatrix} E - H_{\text{sr}} & -P_{\text{sr}}^T V^\dagger \Phi_{t+} \Lambda_{t+} \\ -\Lambda_{t+}^* \Phi_{t+}^\dagger V P_{\text{sr}} & \Lambda_{t+}^* \Phi_{t+}^\dagger V \Phi_{t+} \end{pmatrix} \begin{pmatrix} G_{\text{sr}} \\ G_{t+} \end{pmatrix} = \begin{pmatrix} 1 \\ 0 \end{pmatrix}. \quad (2.73)$$

The second line of the previous system reads

$$G_{t+} = \frac{1}{\Phi_{t+}^\dagger V \Phi_{t+}} \Phi_{t+}^\dagger V P_{\text{sr}} G_{\text{sr}}, \quad (2.74)$$

which, introduced in the first lines of Eq. (2.73) proves Eq. (2.67),

$$[E - H_{\text{sr}} - P_{\text{sr}}^T \Sigma(E) P_{\text{sr}}] G_{\text{sr}} = 1 \quad (2.75)$$

Where we introduced the self-energy

$$\Sigma(E) = V^\dagger \Phi_{\bar{t}+} \Lambda_{\bar{t}+} \frac{1}{\Phi_{\bar{t}+}^\dagger V \Phi_{\bar{t}+}} \Phi_{\bar{t}+}^\dagger V. \quad (2.76)$$

In the previous relation, the energy dependence is implicitly contained in the matrices $\Phi_{\bar{t}+}$ and $\Lambda_{\bar{t}+}$. Due to the inversion of the term $\Phi_{\bar{t}+}^\dagger V \Phi_{\bar{t}+}$, one may ask if the Self-energy is always well defined. V can be a rank deficient matrix, however the rectangular matrix $\Phi_{\bar{t}+}$ only spans the image of V (the kernel modes are dismissed in Eq. (2.73)), so that $\Phi_{\bar{t}+}^\dagger V \Phi_{\bar{t}+}$ is full rank. The only exception is when a bound state is present at the boundary of the lead at a given energy. Indeed in that case the matrix $V \Phi_{e+}$ is not invertible^[21].

The previous expression (2.76) for the self-energy can be simplified using $\Sigma(E) \Phi_{\bar{t}+} = V^\dagger \Phi_{\bar{t}+} \Lambda_{\bar{t}+}$ along with $\Sigma(E) \Phi_{o+} = 0$ and $V^\dagger \Phi_{o+} = 0$ so that $\Sigma(E) \Phi_{t+} = V^\dagger \Phi_{t+} \Lambda_{t+}$ and

$$\Sigma(E) = V^\dagger \Phi_{t+} \Lambda_{t+} (\Phi_{t+})^{-1}. \quad (2.77)$$

The previous relation gives the self-energy as a function of the outgoing modes. We now derive the usual expression of the self-energy in terms of the Green's function, Eq. (2.53). Let us first consider Eq. (2.75) in the case of a simple lead

$$[E - H - \Sigma(E)] G_{\text{lead}} = 1. \quad (2.78)$$

Using equations (2.29) and (2.77) we get

$$\Sigma(E) V^\dagger \Phi_{t+} \Lambda_{t+} = (E - H) \Phi_{t+} \Lambda_{t+} - V \Phi_{t+}. \quad (2.79)$$

Combining Eq. (2.78) with the previous relation gives

$$\Phi_{t+} \Lambda_{t+} = G_{\text{lead}} V \Phi_{t+}. \quad (2.80)$$

To arrive at the desired relation, one must include Eq. (2.77) in Eq. (2.80),

$$\Sigma(E) = V^\dagger G_{\text{lead}} V. \quad (2.81)$$

This section derived several equations that allow to either compute the Green's function of system from the knowledge of the eigenmodes of the lead (equation (2.73)) or with the closed set of equations (2.75), (2.78) and (2.81). These two approaches can be used to write different methods. However, it does not seem obvious how these equations could be generalized to simulate systems infinite in several directions. Indeed, the computation the

lead eigenmodes (i.e. a system infinite in one direction), extensively uses the very simple form of the Hamiltonian in Eq. (2.11), and already in two dimensions a translationally invariant Hamiltonian would not be tridiagonal.

Previously the matrix $\Gamma = i(\Sigma - \Sigma^\dagger)$ was referred to as a velocity or a current operator. We now derive the expressions to support that statement. Using Eq. (2.81) in the definition of Γ holds

$$\Gamma = i(V^\dagger G_{\text{lead}} V - V^\dagger G_{\text{lead}}^\dagger V). \quad (2.82)$$

Projecting the velocity operator between two propagating modes ϕ_p and $\phi_{p'}$ reads

$$\phi_{p'}^\dagger \Gamma \phi_p = i \phi_{p'}^\dagger (V^\dagger \lambda_p - \lambda_{p'}^* V) \phi_p \quad (2.83)$$

where we used Eq. (2.80). In the last expression, we recognize the velocity operator defined in Eq. (2.22) for $p = p'$.

2.6 The Fisher-Lee relation for arbitrary tight-binding systems

We introduced two common approaches to solve scattering problems, one is the scattering matrix formalism, and the other is the Green's function approach. Each approach has its own advantages. In a nutshell, the former has the advantage of being quite intuitive, while the latter contains local information about the system. We conclude this chapter by a proof of the Fisher-Lee relations for general tight-binding models. These relations demonstrate the equivalence of the scattering approach to the Green's function formalism, originally demonstrated in [28].

The proof depends on sections 2.4.4 and 2.5.4. The relations read

$$\Psi_{\text{sr}} = G_{\text{sr}} P_{\text{sr}}^T (\Sigma^\dagger(E) - \Sigma(E)) \Phi_{\text{p-}}, \quad (2.84)$$

$$S_{\text{tp}} = G_{\text{t+}} P_{\text{sr}}^T (\Sigma^\dagger(E) - \Sigma(E)) \Phi_{\text{p-}} + 1_{\bar{\text{t}} \times \text{t}} \Phi_{\text{t+}}^{-1} \Phi_{\text{p-}}, \quad (2.85)$$

where $1_{\bar{\text{t}} \times \text{t}}$ is a rectangular matrix equal to the identity on one block and zero and the other. Formally,

$$1_{\bar{\text{t}} \times \text{t}} = \left(\begin{array}{cccc|ccc} & \overbrace{\hspace{2cm}}^{N_{\bar{\text{t}}}} & & & \overbrace{\hspace{2cm}}^{N_{\text{t}}} & & \\ 1 & 0 & 0 & \dots & 0 & \dots & \\ 0 & 1 & 0 & & \vdots & & \\ 0 & 0 & 1 & & & & \\ \vdots & & & \ddots & & & \end{array} \right). \quad (2.86)$$

The calculations involved in the proof are slightly cumbersome, and can be skipped for the non-specialist reader. The important point of these relations is that one can compute the elements of the Green's function from the scattering matrix, or the other way around.

Proof: Equation (2.73) holds

$$\begin{pmatrix} E - H_{\text{sr}} & -P_{\text{sr}}^T U_{\text{t}+}^\dagger \\ -U_{\text{t}+} P_{\text{sr}} & U_{\text{t}+} \Phi_{\text{t}+} \end{pmatrix} \begin{pmatrix} G_{\text{sr}} \\ G_{\text{t}+} \end{pmatrix} = \begin{pmatrix} 1 \\ 0 \end{pmatrix} \quad (2.87)$$

with

$$U_{\text{t}+} \equiv \Lambda_{\text{t}+}^* \Phi_{\text{t}+}^\dagger V, \quad (2.88)$$

$$U_{\text{p}-} \equiv \Lambda_{\text{p}-}^* \Phi_{\text{p}-}^\dagger V. \quad (2.89)$$

On the other hand, taking out the modes $\lambda_\alpha = 0$ of Eq. (2.43) and multiplying the second line by $\Lambda_{\text{t}+}^* \Phi_{\text{t}+}^\dagger$ gives

$$\begin{pmatrix} E - H_{\text{sr}} & -P_{\text{sr}}^T U_{\text{t}+}^\dagger \\ -U_{\text{t}+} P_{\text{sr}} & U_{\text{t}+} \Phi_{\text{t}+} \end{pmatrix} \begin{pmatrix} \Psi_{\text{sr}} \\ S_{\text{tp}} \end{pmatrix} = \begin{pmatrix} P_{\text{sr}}^T U_{\text{p}-}^\dagger \\ -U_{\text{t}+} \Phi_{\text{p}-} \end{pmatrix} \quad (2.90)$$

where S_{tp} is the generalized scattering matrix with the last N_o lines removed. To demonstrate the equivalence between the scattering matrix and the Green's function approach we use that the matrices on the left hand side of equations (2.90) and (2.87) are equals.

The generalized scattering matrix can be expressed as

$$S_{\text{tp}} = \frac{1}{U_{\text{t}+}^\dagger \Phi_{\text{t}+}} U_{\text{t}+} (P_{\text{sr}} \Psi_{\text{sr}} - \Phi_{\text{p}-}) \quad (2.91)$$

and the wavefunction as

$$(E - H_{\text{sr}}) \Psi_{\text{sr}} = P_{\text{sr}}^T (U_{\text{t}+}^\dagger S_{\text{tp}} + U_{\text{p}-}^\dagger). \quad (2.92)$$

Putting Eq. (2.91) in Eq. (2.92) gives

$$[(E - H_{\text{sr}}) - P_{\text{sr}}^T \Sigma(E) P] \Psi_{\text{sr}} = P_{\text{sr}}^T (U_{\text{p}-}^\dagger - \Sigma(E) \Phi_{\text{p}-}), \quad (2.93)$$

where we used Eq. (2.76) to keep notations compact. In a similar fashion, Eq. (2.87) holds

$$G_{\text{t}+} = \frac{1}{U_{\text{t}+} \Phi_{\text{t}+}} U_{\text{t}+} P_{\text{sr}} G_{\text{sr}}, \quad (2.94)$$

$$(E - H_{\text{sr}}) G_{\text{sr}} = 1 + P_{\text{sr}}^T U_{\text{t}+}^\dagger G_{\text{t}+}, \quad (2.95)$$

so that combining the two previous equations gives

$$[(E - H_{\text{sr}}) - P_{\text{sr}}^T \Sigma(E) P_{\text{sr}}] G_{\text{sr}} = 1, \quad (2.96)$$

where we recognize the usual equation for the Green's function expressed with the self-energy.

Using the similarity between the left hand sides of equations (2.96) and (2.93) it is straightforward to write a relation between the two generalized scattering matrix and the Green's function in the scattering region

$$\Psi_{\text{sr}} = G_{\text{sr}} P_{\text{sr}}^T (U_{\text{p}-}^\dagger - \Sigma(E) \Phi_{\text{p}-}). \quad (2.97)$$

The same can be done with equations (2.91) and (2.94) to obtain the same relation in the leads,

$$S_{\bar{t}\text{p}} = G_{\bar{t}+} P_{\text{sr}}^T (U_{\text{p}-}^\dagger - \Sigma(E) \Phi_{\text{p}-}) - \frac{1}{U_{\bar{t}+} \Phi_{\bar{t}+}} U_{\bar{t}+} \Phi_{\text{p}-}. \quad (2.98)$$

The two previous relations between the Green's function and the scattering matrix are similar to the Fisher-Lee relation^[28] but for tight-binding models. To simplify the expressions, notice that

$$\Phi_{\text{t}+} = \Phi_{\bar{t}+} 1_{\bar{t} \times \text{t}} + \Phi_{\text{o}+} 1_{\text{o} \times \text{t}} \quad (2.99)$$

where

$$1_{\text{o} \times \text{t}} = \left(\begin{array}{ccc|ccc} \overbrace{0 & 0 & \dots}^{N_{\bar{t}}} & \overbrace{1 & 0 & 0 & \dots}^{N_{\text{o}}} \\ 0 & 0 & & 0 & 1 & 0 & \\ \vdots & & & 0 & 0 & 1 & \\ & & & \vdots & & & \ddots \end{array} \right) \quad (2.100)$$

are rectangular matrices made of sizes $N_{\bar{t}} \times N_{\text{t}}$ and $N_{\text{o}} \times N_{\text{t}}$ in equations 2.86 and 2.100 respectively. Each matrix is divided into an identity block and a null block. We assume that the modes in $\Phi_{\text{t}+}$ have been ordered such that the modes $\lambda_\alpha = 0$ are located on the last N_{o} columns. $V \Phi_{\text{o}+} = 0$ implies that

$$V \Phi_{\text{t}+} = V \Phi_{\bar{t}+} 1_{\bar{t} \times \text{t}} \quad (2.101)$$

we obtain

$$\frac{1}{U_{\bar{t}+} \Phi_{\bar{t}+}} U_{\bar{t}+} = 1_{\bar{t} \times \text{t}} \Phi_{\text{t}+}^{-1}, \quad (2.102)$$

where the inverse on the right hand side contains all modes, including the modes $\lambda_\alpha = 0$. We rewrite Eq.(2.98) with this relation

$$S_{\bar{t}\text{p}} = G_{\bar{t}+} P_{\text{sr}}^T (V^\dagger \Phi_{\text{p}-} \Lambda_{\text{p}-} - \Sigma(E) \Phi_{\text{p}-}) + 1_{\bar{t} \times \text{t}} \Phi_{\text{t}+}^{-1} \Phi_{\text{p}-}. \quad (2.103)$$

Following the same steps to prove Eq. (2.76), we have for the advanced self-energy

$$\Sigma^\dagger(E) \Phi_{\text{t}-} = V^\dagger \Phi_{\text{t}-} \Lambda_{\text{t}-}. \quad (2.104)$$

The previous expression may contain some ill-defined modes Λ_{0-} if V is not full-rank. Fortunately, they do not give any contribution to the self-energy as the vectors Φ_{0-} lie on the kernel of V^\dagger .

Discarding the $\lambda_\alpha = 0$ modes,

$$\Sigma^\dagger(E)\Phi_{p-} = V^\dagger\Phi_{p-}\Lambda_{p-} \quad (2.105)$$

we obtain^[22] the desired expression

$$\Psi_{sr} = G_{sr}P_{sr}^T(\Sigma^\dagger(E) - \Sigma(E))\Phi_{p-}, \quad (2.106)$$

$$S_{\bar{t}p} = G_{\bar{t}+}P_{sr}^T(\Sigma^\dagger(E) - \Sigma(E))\Phi_{p-} + 1_{\bar{t}\times t}\Phi_{t+}^{-1}\Phi_{p-}. \quad (2.107)$$

In the case we do not know the Green's function in the leads, the previous equation can be rewritten in the more convenient form

$$S_{\bar{t}p} = 1_{\bar{t}\times t}\Phi_{t+}^{-1}(P_{sr}G_{sr}P_{sr}^T(\Sigma^\dagger(E) - \Sigma(E))\Phi_{p-} + \Phi_{p-}). \quad (2.108)$$

Part II

A general algorithm for computing bound states in infinite tight-binding systems

Chapter 3

A general formulation for the bound state problem

We propose a robust and efficient algorithm for computing bound states of infinite tight-binding systems that are made up of a finite scattering region connected to semi-infinite leads. Our method uses wave matching in close analogy to the approaches used to obtain propagating states and scattering matrices. We show that our algorithm is robust in presence of slowly decaying bound states where a diagonalization of a finite system would fail. It also allows to calculate the bound states that can be present in the middle of a continuous spectrum. We apply our technique to quantum billiards and the following topological materials: Majorana states in 1D superconducting nanowires, edge states in the 2D quantum spin Hall phase, and Fermi arcs in 3D Weyl semimetals.

3.1 Introduction

Simulating quantum devices that are connected to infinite leads is a commonly occurring problem in quantum nanoelectronics. In particular, finding the propagating states in the leads and coupling them to the device allows to evaluate transport properties such as the conductance of the device^[12]. Numerical methods for solving this scattering problem have a long history^[29–31]. Modern stable algorithms are available in several software packages, e.g. Refs. 7,32,33.

The focus of this work is identifying bound states: states, that are localized inside the central region and decay exponentially in the leads or any other translationally invariant bulk of the material (see Fig. 3.1). Although these states do not contribute to transport, they frequently are the central object of study. Examples of bound states relevant to current research include the quantum well states in semiconductor heterostructures, surface

states in metals, impurity states (phosphorus donors in silicon, nitrogen-vacancy centers in diamond^[34], Shiba states due to magnetic impurities in superconductors), Andreev states^[35] in Josephson junctions, and various kinds of protected edge states in topological materials (e.g. Majorana states in superconducting nanowires^[36–38], chiral edge states in quantum spin Hall systems or Fermi arcs in Weyl semi-metals). Computing the bound states can also be desirable from a mathematical or technical perspective: the calculations of Feynman diagrams due to electron-electron interactions requires the full basis of the system (see for instance Ref. 39).

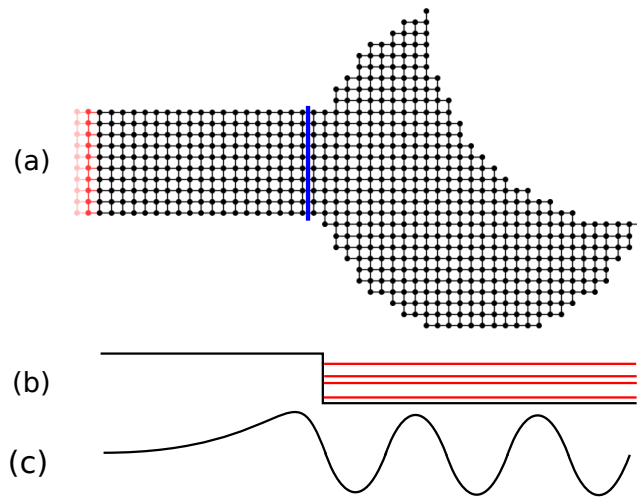


Figure 3.1: Panel (a): an example system considered in this work consisting of a scattering region (right of the blue line) connected to a semi-infinite lead (on the left, the red cells are to be repeated up to infinity). (b): The energy spectrum shows several discrete levels next to the continuous spectrum of the bands. (c): A schematic representation of a bound state wavefunction, decaying exponentially fast in the lead.

Closed-form solutions of the bound state problem exist for several regimes, such as the strong coupling (or short junction) limit of superconducting junctions^[40,41], or the semiclassical approach to impurity bound states^[42].

To solve that problem, one could also use a brute-force method, by cutting out a finite part of the infinite system and diagonalizing the corresponding sub-Hamiltonian. A more evolved numerical method using the boundary element method has been developed in Ref 43, but its drawback is that the scattering region must consist of several homogeneous region and only compute the bound states at negative energies, while our algorithm does not bear these constraints. If the state decays fast enough in the leads and a

sufficiently large portion of them has been included, this results in a precise determination of the bound states. This approach is however not always satisfactory due to its significant computational overhead when the decay length of the bound state diverges. In addition, this brute-force method by itself does not allow to distinguish the bound states from the continuum spectrum when an exact bound state coexists with the continuum spectrum^[44]. We present an algorithm for calculating the bound state spectrum directly for the infinite system. Compared to the brute force method, our approach has the following advantages:

- It is typically more efficient because it operates with smaller matrices than a truncated finite system.
- It provides an exact asymptotic form of the bound states inside the lead.
- Its performance is not hindered by the presence of slowly decaying modes.
- It allows to reliably distinguish bound states from scattering states including the situation when the scattering states exist at the same energy as a bound state.

The outline of this part is as follows. Sec. 3.2 introduces the generic model and the formulation of the bound state problem. The algorithm is developed in Sec. 3.3. The first application, a quantum non-homogeneous discretized billiard, as opposed to continuous ones like in Ref. 45, is presented in Sec. 4.1 where we study the difference between integrable and chaotic billiards and show that in the former there exist bound states in the continuum (BICs) as in Ref. 46. (Indeed, the ability of our algorithm to isolate bound states from the continuum is one of its strengths.) Sections 4.2.1, 4.2.2, and 4.2.3 continue with further applications: the calculation of edge states for three different kinds of topological phases. These are, respectively, a 1D Majorana bound state in a superconducting wire, a 2D quantum spin Hall phase within the Bernevig-Hughes-Zhang (BHZ) model, and Fermi arcs in a 3D Weyl semimetal.

3.2 The bound state problem

3.2.1 General model

A typical system of interest is sketched in Fig. 3.1: a central system of N_{sr} orbitals is connected to one or more leads. The leads themselves are semi-infinite and periodic. They consist of unit cells that contain N_{t} orbitals each

where $\lambda = e^{ik}$ characterizes the momentum in the lead and j labels its unit cells (the index grows with increasing distance from the scattering region). The Schrödinger equation in the lead takes the form

$$V\phi + \lambda(H - E)\phi + \lambda^2 V^\dagger \phi = 0 \quad (3.3)$$

or alternatively

$$H(k)\phi = E\phi,$$

where we have introduced the Bloch Hamiltonian

$$H(k) = H + Ve^{-ik} + V^\dagger e^{ik}. \quad (3.4)$$

Introducing $\xi \equiv \lambda\phi$ we transform the Eq. (3.3) the generalized eigenstate problem

$$\begin{pmatrix} H - E & V^\dagger \\ 1 & 0 \end{pmatrix} \begin{pmatrix} \phi \\ \xi \end{pmatrix} = \frac{1}{\lambda} \begin{pmatrix} -V & 0 \\ 0 & 1 \end{pmatrix} \begin{pmatrix} \phi \\ \xi \end{pmatrix}, \quad (3.5)$$

that can, be solved using standard linear algebra routines (in practice this step requires some care and will be discussed extensively in Ref. ?). Solutions of the Eq. (3.5) with $|\lambda| = 1$ (real values of the momentum k) are propagating while those with $|\lambda| < 1$ are evanescent. Finally, modes with $|\lambda| > 1$ diverge exponentially with the distance from the scattering region and therefore they play no role in the bound state problem.

3.2.3 Formulation of the bound state problem

Inside the lead an eigenstate $\hat{\psi}$ can be expressed as a superposition of propagating and evanescent modes. We can now formulate the bound state problem as follows: *a bound state is an eigenstate $\hat{\psi}$ that has no overlap with the propagating modes, i.e. that is purely evanescent.* To be more specific, we gather all the eigenvalues $|\lambda| < 1$ at a given energy E into a diagonal matrix $\Lambda_e(E)$ (of size $N_e \times N_e$) and the corresponding evanescent eigenstates ϕ into the matrix $\Phi_e(E)$ (each column of the $N_t \times N_e$ matrix Φ_e is a vector ϕ corresponding to an evanescent state). With these definitions Eq. (3.3) takes the form

$$V\Phi_e + (H - E)\Phi_e\Lambda_e + V^\dagger\Phi_e(\Lambda_e)^2 = 0. \quad (3.6)$$

Using this notation, an eigenstate $\hat{\psi}$ assumes the following general form in the lead:

$$\psi(j > 0) = \Phi_e(\Lambda_e)^j q_e, \quad (3.7)$$

56A general formulation for the bound state problem

where the vector q_e contains the coefficients of the expansion in terms of the evanescent states. Denoting the subvector of $\hat{\psi}$ inside the scattering region ψ_{sr} , we arrive at the following equation with unknown (ψ_{sr}, q_e) :

$$\begin{pmatrix} H_{\text{sr}} - E & P_{\text{sr}}^T V^\dagger \Phi_e(E) \Lambda_e(E) \\ V P_{\text{sr}} & -V \Phi_e(E) \end{pmatrix} \begin{pmatrix} \psi_{\text{sr}} \\ q_e \end{pmatrix} = 0. \quad (3.8)$$

Here we have reinstated the explicit energy dependence of the mode matrices, and this result is very similar to Eq.D2 of Ref. 49, but the authors did not look for a way to formulate this nonlinear problem in an efficient and practical algorithm. We therefore reduce the bound state problem to finding E , ψ_{sr} , and q_e satisfying the Eq. (3.8).

Eliminating q_e from the Eq. (3.8) yields an equivalent equation

$$[H_{\text{sr}} + \Sigma(E)]\psi_{\text{sr}} = E\psi_{\text{sr}}, \quad (3.9)$$

where the self-energy Σ is

$$\Sigma(E) = P_{\text{sr}}^T V^\dagger \Phi_e \Lambda_e \frac{1}{V \Phi_e} V P_{\text{sr}}. \quad (3.10)$$

] In the remainder, we focus on the formulation Eq. (3.8) and do not make use of the alternative self-energy formulation. Note that Eq. (3.10) is only defined when the matrix V is invertible. A better definition of the self-energy is given in the next section.

3.3 Numerical algorithm for finding bound states

We now turn to the construction of practical algorithms that use Eq. (3.8) to calculate the bound states of an infinite system. For completeness and pedagogical purposes, we present three different algorithms of increasing effectiveness. Algorithm III is numerically superior to the other two.

3.3.1 Algorithm I: non-Hermitian formulation

The first algorithm is formulated directly in the non-Hermitian representation of Eq. (3.8). The first thing to notice is that when the matrix V is not invertible, it admits trivial solutions. As an example, let us consider

$$V = \begin{pmatrix} 0 & 1 \\ 0 & 0 \end{pmatrix}.$$

One immediately sees that this leads to the last row of Eq. (3.8) to be made up of zeros, so that the equation admits solutions for any energy E . However, while one can find a non-zero vector q_e , it corresponds to a

vanishing eigenvalue λ for a vector ϕ that belongs to the kernel of V (i.e. $V\phi = 0$) so that the actual state given by Eq. (3.7) vanishes everywhere and is therefore not a true solution.

To remove these spurious solutions, we perform a singular value decomposition of V that we write as $V = U_V D W_V^\dagger$, where U_V and W_V are unitary matrices while D is diagonal. We order the matrices D and Λ_e such that their vanishing eigenvalues are placed in the lower right part of the matrix. It can be noted that the number of eigenvalues $\lambda = 0$ is equal to the dimension of the kernel of V , as seen from Eq. (3.3). Discarding the zero-valued trailing rows of Eq. (3.8) and an equal number of columns, that are either made of zeros or correspond to modes associated with $\lambda = 0$ contributions, we arrive at

$$\begin{pmatrix} H_{\text{sr}} - E & P_{\text{sr}}^T V^\dagger \tilde{\Phi}_e \tilde{\Lambda}_e \\ \tilde{D} \tilde{W}_V^\dagger P_{\text{sr}} & -\tilde{D} \tilde{W}_V^\dagger \tilde{\Phi}_e \end{pmatrix} \begin{pmatrix} \psi_{\text{sr}} \\ \tilde{q}_e \end{pmatrix} = 0, \quad (3.11)$$

where $\tilde{\Phi}_e$, $\tilde{\Lambda}_e$, \tilde{q}_e , \tilde{D} and \tilde{W}_V^\dagger are the truncated versions of Φ_e , Λ_e , q_e , D and W_V^\dagger , where the elements that play no role are removed. The matrix in Eq. (3.11) has the size $(N_{\text{sr}} + N_V) \times (N_{\text{sr}} + N_e)$, where N_V is the rank of V . Note that the matrix is square if and only if there are no propagating modes.

The bound state problem is now reduced to finding the values of E for which the left-hand side $Q(E)$ of Eq. (3.11) is not invertible. However, $Q(E)$ is in general not Hermitian and not even a square matrix. Singular value decomposition provides a solution to this problem: we form the matrix $Q^\dagger(E)Q(E)$ and obtain its lowest eigenvalues using a sparse solver (we use the Arpack implementation of the Lanczos algorithm using the shift-invert technique). Since the matrix $Q^\dagger Q$ is positive definite its eigenvalues are also positive (see an example in Fig. 3.2b), we are hence looking for zero singular values using standard one-dimensional minimization algorithms. They are however less efficient than the root-finding algorithms that we apply in algorithms II and III.

Algorithm I is similar to the algorithm introduced in Refs. 50,51 which maps the bound state problem on the solution of a non-linear eigenvalue problem of a non-Hermitian matrix. There is, however, a notable difference: Refs. 50,51 looks for a vanishing determinant instead of the lowest singular value. This is less numerically efficient since determinant calculations can easily overflow/lose precision for large matrices and they do not exploit the matrix sparsity structure.

3.3.2 Hermitian formulation

To improve on algorithm I, we slightly reformulate Eq. (3.8) which is in general overcomplete since the matrix on the left-hand side is $(N_{\text{sr}} + N_t) \times$

58A general formulation for the bound state problem

$(N_{\text{sr}} + N_e)$. By multiplying the second line of Eq. (3.8) by $\Lambda_e^* \Phi_e^\dagger$ we obtain a set of *necessary* conditions for a bound state to occur:

$$\begin{pmatrix} H_{\text{sr}} - E & P_{\text{sr}}^T V^\dagger \Phi_e \Lambda_e \\ \Lambda_e^* \Phi_e^\dagger V P_{\text{sr}} & -\Lambda_e^* \Phi_e^\dagger V \Phi_e \end{pmatrix} \begin{pmatrix} \psi_{\text{sr}} \\ q_e \end{pmatrix} = 0, \quad (3.12)$$

with the explicit dependence on energy E removed for clarity. The matrix on the left-hand side of Eq. (3.12) now has a square $(N_{\text{sr}} + N_e) \times (N_{\text{sr}} + N_e)$ shape and is moreover Hermitian, a desirable property for numerical purposes. Indeed, as we show in App. A.2, Eq. (3.6) leads to

$$\Lambda_e^* \Phi_e^\dagger V \Phi_e = \Phi_e^\dagger V^\dagger \Phi_e \Lambda_e, \quad (3.13)$$

and therefore to Hermiticity of Eq. (3.12).

The next step is to get rid of the spurious $\lambda = 0$ solutions that can be present in Λ_e . We reorder the Λ_e matrices so that their vanishing eigenvalues are placed in the lower right part of the matrix. After this reordering the corresponding last rows of Eq. (3.12) vanish, and we therefore remove them from the matrix. Similarly, by using Eq. (3.13), we also remove the last columns of the matrix. Introducing truncated quantities $\tilde{\Phi}_e$, $\tilde{\Lambda}_e$, and \tilde{q}_e where the zero entries due to the $\lambda = 0$ contributions have been disregarded, we finally arrive at

$$\begin{pmatrix} H_{\text{sr}} - E & P_{\text{sr}}^T V^\dagger \tilde{\Phi}_e(E) \tilde{\Lambda}_e(E) \\ \tilde{\Lambda}_e^*(E) \tilde{\Phi}_e^\dagger(E) V P_{\text{sr}} & -\tilde{\Lambda}_e^*(E) \tilde{\Phi}_e^\dagger(E) V \tilde{\Phi}_e(E) \end{pmatrix} \begin{pmatrix} \psi_{\text{sr}} \\ \tilde{q}_e \end{pmatrix} = 0, \quad (3.14)$$

the central result of this part, where we show the explicit energy dependence to emphasize the non-linearity of the eigenproblem.

Eliminating \tilde{q}_e from the Eq. (3.14) we also obtain an alternative expression of the self-energy that is defined even when V is not invertible:

$$\Sigma(E) = P_{\text{sr}}^T V^\dagger \tilde{\Phi}_e \tilde{\Lambda}_e \frac{1}{\tilde{\Lambda}_e^* \tilde{\Phi}_e^\dagger V \tilde{\Phi}_e} \tilde{\Lambda}_e^* \tilde{\Phi}_e^\dagger V P_{\text{sr}}. \quad (3.15)$$

Combining this expression with Eq. (3.9) provides an equivalent alternative to the algorithms presented below. We do not pursue this route because there is no a-priori indication of any benefits from using the self-energy formulation, either by solving directly Eq. (3.9) or using an iterative scheme.

3.3.3 Algorithm II: root finder in the Hermitian formulation

The problem is now set in a Hermitian form suitable for numerical computation. Let us abbreviate Eq. (3.14) as

$$H_{\text{eff}}(E) \psi_{\text{eff}} = 0 \quad (3.16)$$

with

$$H_{\text{eff}} \equiv \begin{pmatrix} H_{\text{sr}} - E & P_{\text{sr}}^T V^\dagger \tilde{\Phi}_e \tilde{\Lambda}_e \\ \tilde{\Lambda}_e^* \tilde{\Phi}_e^\dagger V P_{\text{sr}} & -\tilde{\Lambda}_e^* \tilde{\Phi}_e^\dagger V \tilde{\Phi}_e \end{pmatrix}, \quad (3.17)$$

and

$$\psi_{\text{eff}} \equiv \begin{pmatrix} \psi_{\text{sr}} \\ \tilde{q}_e \end{pmatrix}. \quad (3.18)$$

The E -dependence has not been written explicitly in Eq. (3.17), but the solutions $\tilde{\Lambda}_e(E)$ and $\tilde{\Phi}_e(E)$ of Eq. (3.6) are nontrivial functions of E , which makes the eigenproblem a nonlinear one. We are interested in finding the values of E and the corresponding eigenvectors at which Eq. (3.16) admits nontrivial solutions. A necessary condition for this is the presence of a zero eigenvalue of $H_{\text{eff}}(E)$. For any given E , the eigenvalues of $H_{\text{eff}}(E)$ that are close to zero can be computed using a sparse solver (again, we use the Arpack implementation of the Lanczos algorithm using the shift-invert technique). The values of E where any eigenvalue vanishes can be then found using one of the many standard root-finding algorithms for one-dimensional functions.

Once a vanishing eigenvalue has been found, a check is necessary in order to avoid a solution that is not a physical bound state. A trivial example of such a false positive is an eigenstate of H_{sr} at an energy E such that there are no evanescent states. In that case the matrices Φ_e and Λ_e are empty and Eq. (3.16) is nothing but the Schrödinger equation for the scattering region alone. Hence, once a candidate solution has been found one checks that

$$V P_{\text{sr}} \psi_{\text{sr}} - V \Phi_e q_e = 0 \quad (3.19)$$

to verify that the solution indeed satisfies the original set of equations.

Figure 3.2a shows an example of the eigenvalues of $H_{\text{eff}}(E)$ as a function of E for an integrable billiard [the specific Hamiltonian is introduced later in Eq.(4.1)]. The vanishing eigenvalues correspond to possible bound states solutions, while the arrows indicate those that are true bound states.

3.3.4 Algorithm III: improved convergence thanks to gradient calculation

To improve the convergence of the root finder algorithm we expand $H_{\text{eff}}(E)$ up to a linear order in E . Since $H_{\text{eff}}(E)$ is a Hermitian matrix, we use first-order perturbation theory to obtain the gradient of its eigenvalues with respect to E ,

$$\frac{d\varepsilon_\alpha}{dE} = \psi_{\text{eff},\alpha}^\dagger \frac{dH_{\text{eff}}}{dE} \psi_{\text{eff},\alpha}, \quad (3.20)$$

where ε_α is an eigenvalue of H_{eff} and $\psi_{\text{eff},\alpha}$ the corresponding eigenvector. Knowing the gradient allows to use root-finding algorithms that converge much faster, such as the Newton-Raphson method.

60A general formulation for the bound state problem

When implementing this algorithm, one needs to evaluate dH_{eff}/dE which amounts to calculating the derivatives $d\Lambda_e/dE$ and $d\Phi_e/dE$. These matrices are built from the non-Hermitian generalized eigenproblem (3.5). To compute these derivatives, we follow Ref. 52 for a general eigenproblem of the form

$$Ax = \kappa Bx, \quad (3.21)$$

where A and B are the matrices on the left and right-hand side of Eq. (3.5), $x = \begin{pmatrix} \phi \\ \xi \end{pmatrix}$ and $\kappa = 1/\lambda$. We assume the eigenvalue κ to be non-degenerate. Since the matrix B does not depend on energy, taking the first derivative of Eq. (3.21) gives

$$A \frac{dx}{dE} - \kappa B \frac{dx}{dE} - \frac{d\kappa}{dE} Bx = -\frac{dA}{dE} x.$$

The left-hand side of the above equation can be rewritten as an extended matrix-vector product of the form

$$(A - \kappa B \quad -Bx) \begin{pmatrix} \frac{dx}{dE} \\ \frac{d\kappa}{dE} \end{pmatrix} = -\frac{dA}{dE} x. \quad (3.22)$$

This system cannot be solved directly since there are $2N_t + 1$ unknowns but only $2N_t$ equations. An additional constraint arises from the normalization of the eigenvector x . We choose to set the value of the largest component of x to unity: writing m for the index of the largest component of x , we have $x_m \equiv 1$ therefore $\frac{dx_m}{dE} = 0$ and we can remove the corresponding m -th column from the left-hand side of Eq. (3.22). We are left with a system which, unless κ corresponds to a degenerate eigenvector, has linearly independent columns^[52] and can be solved numerically.

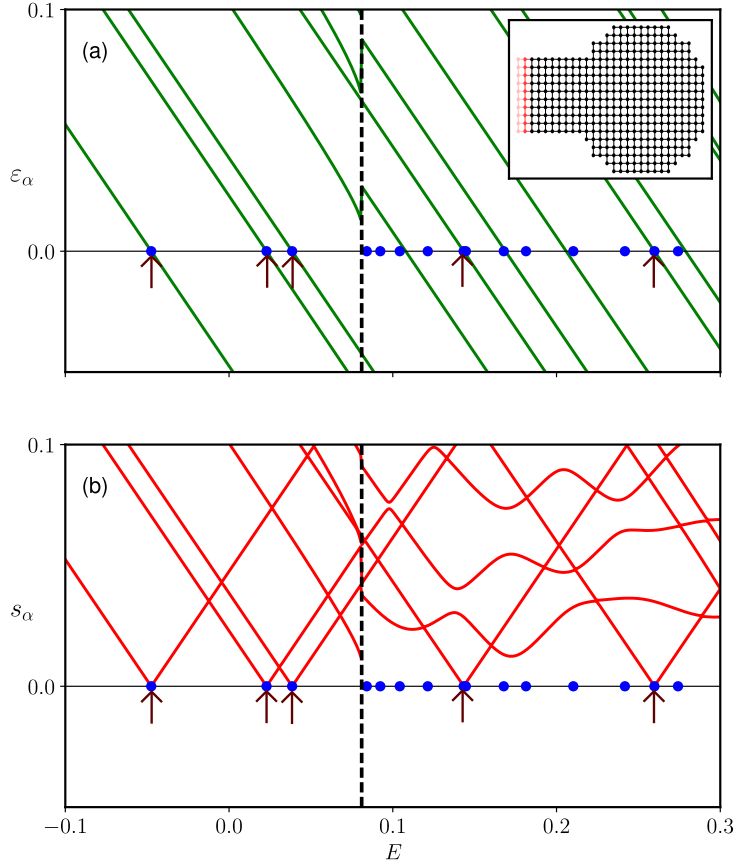


Figure 3.2: (a): eigenvalues $\varepsilon_\alpha(E)$ of Eq. (3.17) as a function of E for a quantum billiard. (b): lowest singular values $s_\alpha(E)$ of the left-hand side of Eq. (3.11) for the same billiard. Inset: schematic of the billiard, described by Eq. (4.1) with $v_g = -0.1$. The blue dots correspond to the eigenenergies of a truncated system that consists of the billiard plus a finite fraction of the lead. The arrows indicate the positions of the actual bound states of the infinite system. The black dashed line corresponds to the opening of the first mode of the lead, which is marked by a discontinuity in the eigenvalues $\varepsilon_\alpha(E)$ and the singular values $s_\alpha(E)$.

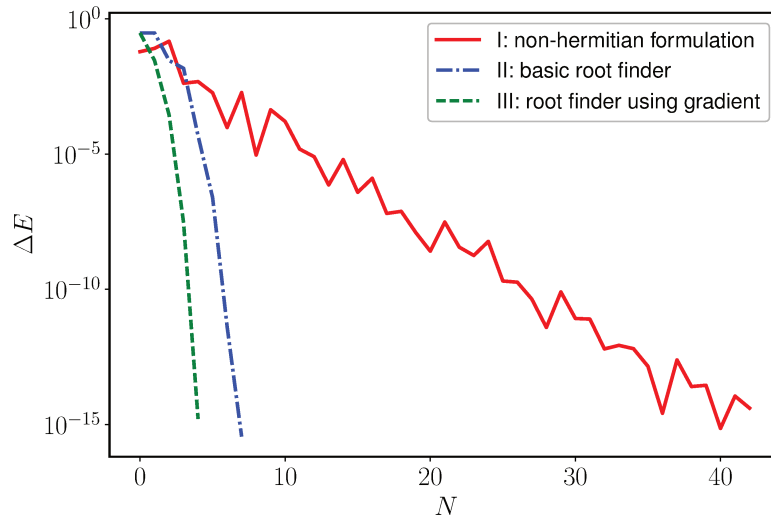


Figure 3.3: Convergence of the bound state energy as a function of the number of iterations for the three algorithms presented in the text.

3.3.5 Visualization of algorithms I, II and III

Figure 3.2 shows the eigenvalues of Eq. (3.14) and the lowest singular values of Eq. (3.11) for an integrable quantum billiard (to be introduced in the next section) as a function of E . At energies below the band bottom, when there are no propagating modes (left of the vertical dashed line), we observe a one-to-one correspondence between eigenvalues going through zero, zero-valued minima of singular values, as well as eigenstates of a truncated system. Due to the finite size of the truncated system there is a small mismatch between its eigenenergies and the zero crossings/minima. For energies (right of the vertical dashed line), the scattering region is connected to a continuum of states. The transition is marked by a discontinuity in the eigenvalues of Eq. (3.14). In this regime there exist eigenstates of the truncated system that do not match a vanishing singular value. These states correspond to the continuum and more of them appear as more lead cells are included in the truncated system. The eigenvalues of Eq. (3.14) have more zeros than the singular values of Eq. (3.11) because some solutions of Eq. (3.14) are false positives that can be eliminated using Eq. (3.19).

The convergence rate of the different approaches is shown in Fig. 3.3, which confirms that algorithm III is the fastest. Since perfect convergence is achieved after only a few iterations, this algorithm is capable of obtaining the bound states for a cost comparable to that of calculating the propagating modes (scattering matrix).

Chapter 4

Applications of the bound state solver

4.1 Application to quantum billiards

We consider a circular (integrable) quantum billiard discretized on a square lattice with nearest neighbor hoppings:

$$H = 4t - t \sum_{\langle i,j \rangle} |i\rangle \langle j| + v_g \sum_{i \in \text{sr}} |i\rangle \langle i|, \quad t = 1. \quad (4.1)$$

Here, $\langle i, j \rangle$ stands for a summation over nearest neighbours. The summation in the last term is restricted to the scattering region, applying an onsite potential v_g inside it, while this potential is equal to 0 in the lead.

We compute the density of states (DOS) of this system using Kwant^[7], and the bound state spectrum using our algorithm. The results are shown in Fig. 4.1. We observe that there is an energy range in which bound states coexist with the continuum without mixing with it. At a certain energy a second propagating channel opens in the lead and washes out the remaining bound states. Below the bottom of the band, only bound states are present in the system. We emphasize that the bound states inside the continuum (BICs) present in the intermediate energy range $0.03 \leq E \leq 0.15$ are very difficult to observe with a direct diagonalization of a finite system, since there is no simple way to distinguish eigenstates that originate from the continuum from actual bound states. Two examples of wavefunctions corresponding to particular bound states are shown in Fig. 4.2.

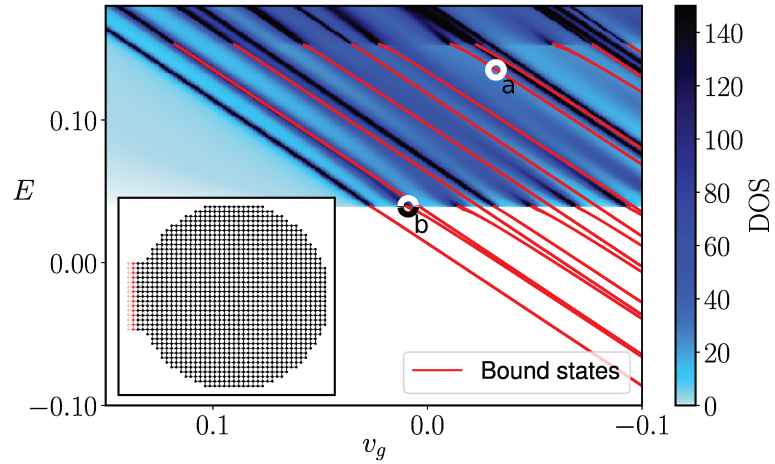


Figure 4.1: Color plot: density of states in the scattering region, from zero (white) to 150 (dark blue) as a function of v_g . Red lines: energies of bound states calculated using our algorithm. Inset: the scattering region (black) and a few cells of the lead (red). This system consists of about one thousand sites. The wavefunctions corresponding to the two circles (a) and (b) are shown in Figures 4.2a) and 4.2b).

The presence of the BICs is a consequence of the symmetry of the circular billiard and of the corresponding lead: the lowest propagating mode is symmetric with respect to the y -axis while the BICs are antisymmetric, as shown in Fig. 4.2a), hence the absence of hybridization. On the other hand, the BICs do not appear in the chaotic billiard of Fig. 4.3 which does not have reflection symmetry.

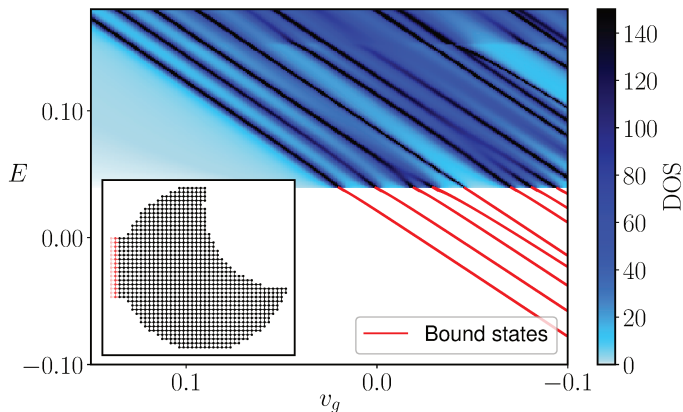


Figure 4.3: Same as Fig. 4.1, but with a chaotic scattering region.

4.2 Topological materials

We now present applications to topological materials where our algorithm is used to illustrate the bulk-boundary correspondence. In these three examples, we consider infinite systems of different dimensionality that are cut at $x = 0$ to form, respectively, a semi-infinite wire (with 0D Majorana), a half plane (with 1D edge state), and half space (with a 2D Fermi arc surface state). In all these examples we consider a lattice termination boundary with $H_{\text{sr}} = H$, and $P_{\text{sr}} = 1$.

4.2.1 One-dimensional superconducting nanowire, Majorana bound states

The starting point for the topological superconducting nanowire is the Bloch Hamiltonian from Ref. 37:

$$H(k) = \tau_z(\mu - 2t) + \sigma_z B + \tau_x \Delta + \tau_z t \cos(k) + \tau_z \sigma_x \alpha_{\text{so}} \sin(k), \quad (4.2)$$

where the Pauli matrices $(\tau_0, \tau_x, \tau_y, \tau_z)$ and $(\sigma_0, \sigma_x, \sigma_y, \sigma_z)$ act in the Nambu (electron-hole) space and spin space, respectively. The parameter Δ is the superconducting gap, μ the chemical potential, α_{so} the strength of the spin-orbit coupling and B the Zeeman magnetic field. Equation (4.2) corresponds to a tight-binding Hamiltonian with $N_t = 4$,

$$H = \tau_z(\mu - 2t) + \sigma_z B + \tau_x \Delta, \quad (4.3)$$

$$V = \tau_z t + i\tau_z \sigma_x \alpha_{\text{so}}. \quad (4.4)$$

In Fig. 4.4 we compare diagonalization of a finite system with the output of our algorithm. The upper panel shows the spectrum of a superconducting wire of finite length as a function of the chemical potential. The region with a dense set of energies corresponds to the continuum while the Majorana bound states are isolated. The lower panel displays the bound states as calculated with our algorithm and the DOS obtained with Kwant^[7]. Both panels match perfectly, but the bound state algorithm has the advantage of working directly in the thermodynamic limit which enables it to distinguish bound states from the continuum.

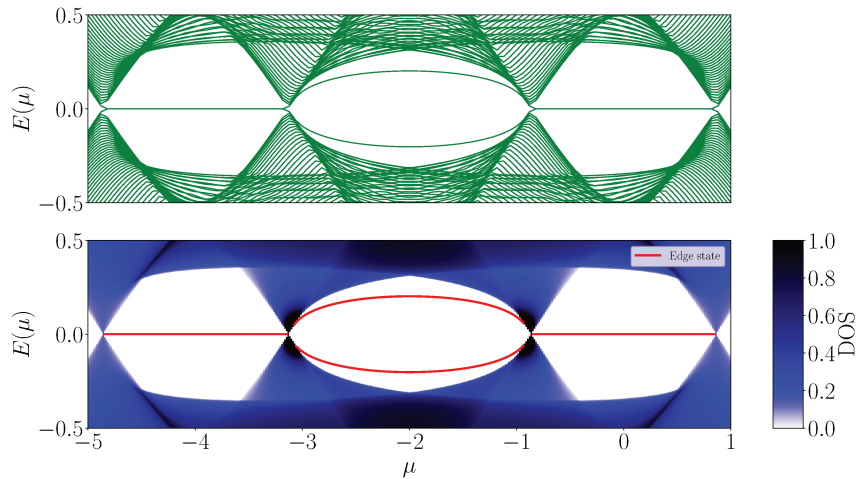


Figure 4.4: Spectrum of a superconducting nanowire as a function of chemical potential μ . Upper panel, the eigenvalues of a finite wire of 100 sites obtained using direct diagonalization. Lower panel, color plot of the local DOS (blue) together with the bound states calculated directly in the thermodynamic limit (red lines). The Hamiltonian is given in Eq. (4.2) with $B = 1$, $t = -1$, $\alpha_{\text{so}} = 0.5$ and $\Delta = 0.5$.

In Fig. 4.5 we compute the wave function $\psi_{\text{sr}}^\dagger \psi_{\text{sr}}$ at the boundary of the topological region. Close to the quantum phase transition between the topological and non-topological phases the brute force diagonalization exhibits finite size corrections.

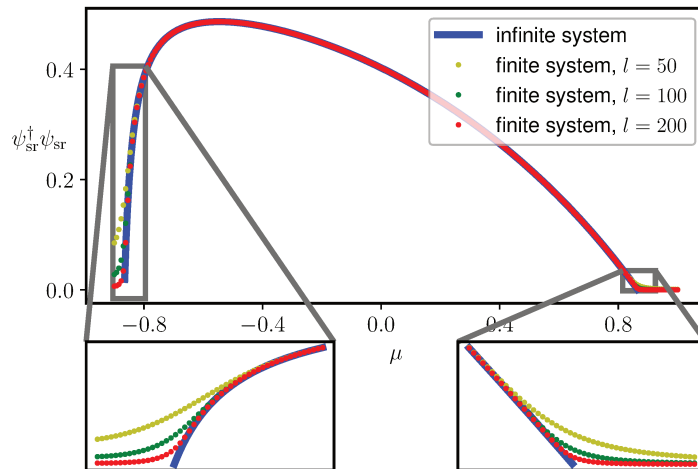


Figure 4.5: Weight of the Majorana bound state at the system boundary $\psi_{\text{sr}}^\dagger \psi_{\text{sr}}$ as a function of the chemical potential μ . The solid line is computed using our algorithm, i.e., simulating a semi-infinite system, while the dotted lines correspond to the diagonalization of finite systems with sizes $l = 50, 100$ and 200 . The finite size effects are more pronounced close to the critical point where the gap closes, while our algorithm is only limited by machine precision. Insets: zoom of the main curve.

Another application of the bound state algorithm to the same Hamiltonian, illustrated in Fig. 4.6, is the calculation of the Andreev bound states of a Josephson junction. The hopping term between the left superconductor and the normal metal is described by Eqs. (4.3) and (4.4) but acquires a phase difference φ such that

$$V_{\text{SN}} = \exp(i\varphi\tau_z)(\tau_z t + i\tau_z\sigma_x\alpha_{\text{SO}}). \quad (4.5)$$

The normal section in the center consists of one site where the gap $\Delta = 0$ and an onsite potential $V_N\tau_z$ is added. The Fig. 4.6 shows the energy of the Andreev bound states as a function of the phase difference φ in the topological (a) and trivial (b) case. As expected, one recovers the 4π and 2π periodicity of the respective spectrum.

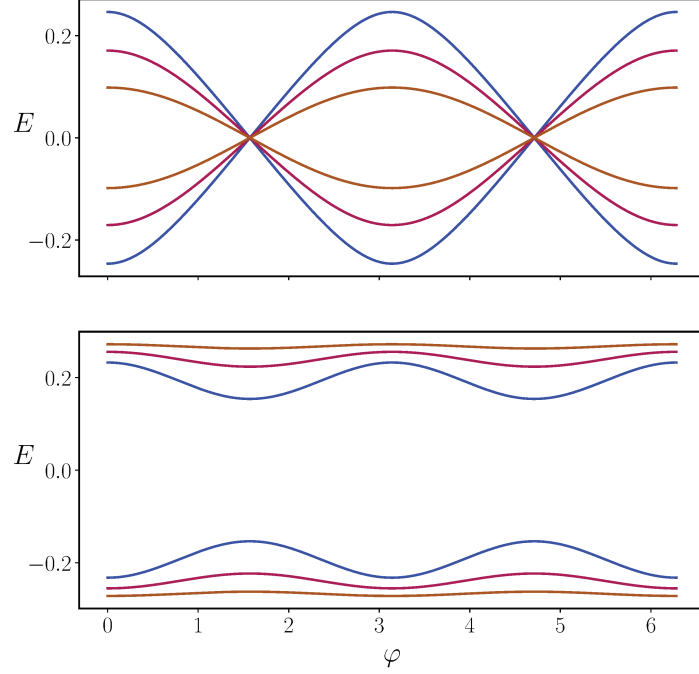


Figure 4.6: Andreev bound states in a Josephson junction as a function of the superconducting phase difference φ . Parameters are set to $\Delta = 0.5$, $\mu = 0.5$, $V_N = 1.25$ (blue), 2.5 (red) and 5 (orange), $\alpha_{\text{so}} = 0.5$. $B = 1$ in the topological regime (panel a) and $B = 0.4$ in the trivial one (panel b).

4.2.2 Quantum spin Hall effect

We continue with the two-dimensional BHZ model for the quantum spin Hall effect^[53]:

$$H(\mathbf{k}) = \begin{pmatrix} h(\mathbf{k}) & 0 \\ 0 & h^*(-\mathbf{k}) \end{pmatrix}, \quad (4.6)$$

where

$$h(\mathbf{k}) = \epsilon(\mathbf{k}) + \vec{d}(\mathbf{k}) \cdot \vec{\sigma},$$

and

$$\begin{aligned} \epsilon(\mathbf{k}) &= C - D(k_x^2 + k_y^2), \\ \vec{d}(\mathbf{k}) &= (Ak_x, -Ak_y, M - B(k_x^2 + k_y^2)). \end{aligned}$$

The vector $\vec{\sigma} = (\sigma_x, \sigma_y, \sigma_z)$ contains the Pauli matrices. The constants A , B , C , D and M are material parameters. The tight-binding model is two-dimensional with the onsite Hamiltonian

$$H_0 = (C - 4D)\sigma_0 + (M - 4B)\sigma_z, \quad (4.7)$$

and hopping matrices

$$\begin{aligned} V_x &= D\sigma_0 + B\sigma_z + \frac{1}{2i}A\sigma_x, \\ V_y &= D\sigma_0 + B\sigma_z - \frac{1}{2i}A\sigma_y \end{aligned} \quad (4.8)$$

along the two directions.

We apply the Bloch theorem in the x -direction, and compute the bound state spectrum and the DOS as a function of k_x . We calculate the bound state of the effective quasi-one-dimensional system (parametrized by k_x) given by

$$\begin{aligned} H &= H_0 + V_x e^{-ik_x} + V_x^\dagger e^{ik_x}, \\ V &= V_y, \end{aligned} \quad (4.9)$$

for which our algorithm can be applied directly. The results are shown in Fig. 4.7 where the DOS in the topological insulating phase is shown together with the positions of the bound states. As expected, the helical edge states appear in the gap.

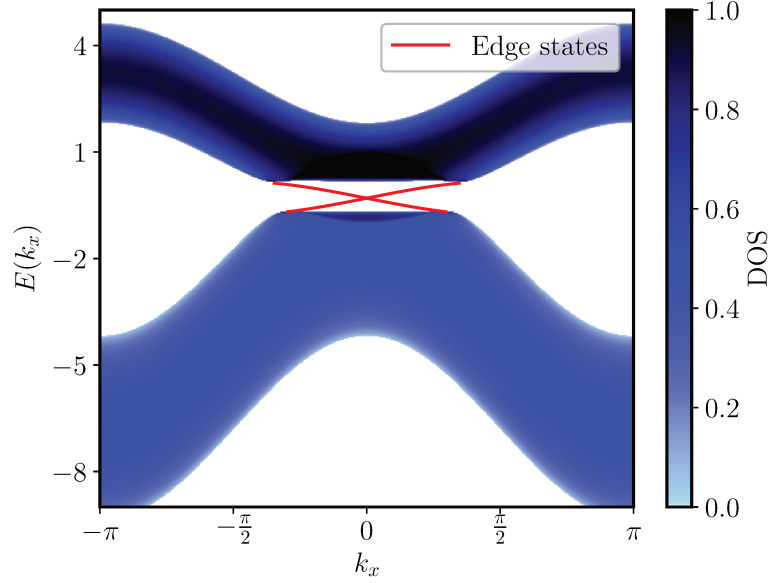


Figure 4.7: Color map of the density of states in the quantum spin Hall effect (blue) and corresponding edge states (red). The parameters have been fixed so that the model is in the topologically non-trivial insulating phase, $A = 0.5, B = 1, C = 0, D = 0.3, M = -1$.

4.2.3 Fermi arcs in Weyl semimetals

We conclude with a last example that uses the same procedure for a three-dimensional Weyl semimetal whose Bloch Hamiltonian is given by^[54]

$$H(\mathbf{k}) = \tau_z [t\sigma_x \sin(k_x) + t\sigma_y \sin(k_y) + t_z\sigma_z \sin(k_z)] + \mu(\mathbf{k})\tau_x\sigma_0 + \frac{1}{2}b_0\tau_z\sigma_0 + \frac{1}{2}\beta\tau_0\sigma_z, \quad (4.10)$$

where

$$\mu(\mathbf{k}) = \mu_0 + t(2 - \cos(k_x) - \cos(k_y)) + t_z(1 - \cos(k_z)).$$

This Hamiltonian corresponds to the 3D tight-binding model

$$\begin{aligned} H_0 &= (\mu_0 + 2t + t_z)\tau_x + \frac{1}{2}b_0\tau_z + \frac{1}{2}\beta\sigma_z, \\ V_x &= \frac{1}{2}it\tau_z\sigma_x - \frac{1}{2}t\tau_x\sigma_0, \\ V_y &= \frac{1}{2}it\tau_z\sigma_y - \frac{1}{2}t\tau_x\sigma_0, \\ V_z &= \frac{1}{2}it_z\tau_z\sigma_z - \frac{1}{2}t_z\tau_x\sigma_0. \end{aligned} \quad (4.11)$$

Once again, applying the Bloch theorem in the x -direction and using k_y and k_z as parameters, so that

$$\begin{aligned} H &= H_0 + (V_y e^{-ik_y} + V_z e^{-ik_z} + h.c.), \\ V &= V_x, \end{aligned} \quad (4.12)$$

which can be used directly in our algorithm. The results are shown in Fig. 4.8 and 4.9. As expected, we obtain the Fermi arcs that couple the two Weyl points. Again, our algorithm allows to study a single surface of the Weyl semimetal, in contrast with the finite size calculations (shown in the lower panel of Fig. 4.8) where states belonging to the two surfaces hybridize.

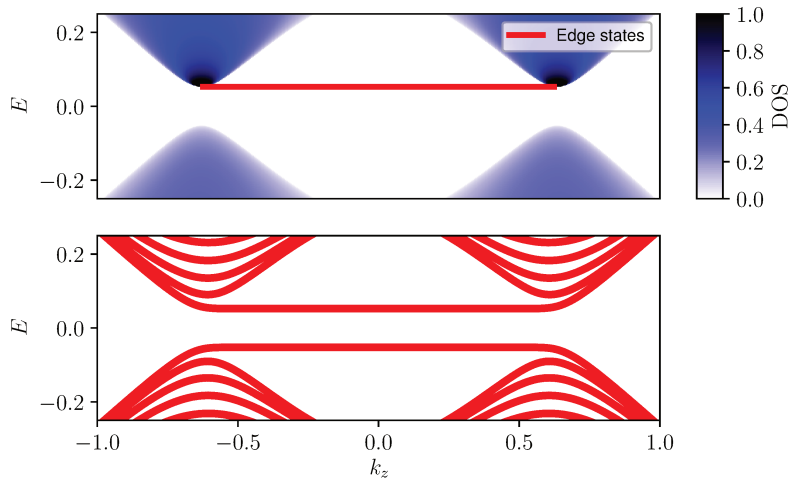


Figure 4.8: Upper panel: Color map of the DOS of the Weyl model and corresponding surface states as a function of energy E and k_z for a fixed value of $k_y = \pi/120$. Lower panel: Corresponding spectrum for a finite stack of 120 layers along the x direction. The parameters were set to $t = 2$, $t_z = 1$, $\mu = -0.3$, $b_0 = 0$, $\beta = 1.2$. A similar simulation is featured in Ref. 55.

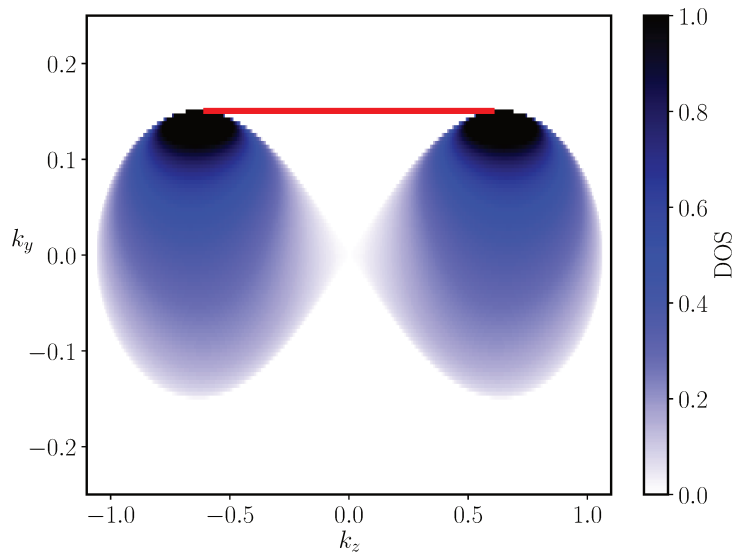


Figure 4.9: Same as the upper panel of Fig. 4.8 with an alternative view: the energy $E = 0.3$ is fixed and the DOS is plotted as a function of (k_y, k_z) .

4.3 Conclusion

We have derived a robust and efficient algorithm to compute the energies and the wavefunctions of the bound states of infinite quasi one-dimensional systems described by general tight-binding Hamiltonians. We have applied our approach to a variety of systems and shown that it can efficiently calculate the bound states, including the situations where other approaches would fail or become computationally prohibitive.

This algorithm can be used on its own to obtain e.g. the Josephson relation of superconducting-normal-superconducting junctions, the properties of quantum wells or characterize topological materials and their interfaces. It may also be used to obtain the properties of perfect surfaces or interfaces (in arbitrary topological, metallic or superconducting materials) that can then be used as the starting point for further calculations.

Acknowledgments

We thank Daniel Varjas for pointing out the need for orthogonalization of the evanescent modes in presence of additional degeneracies.

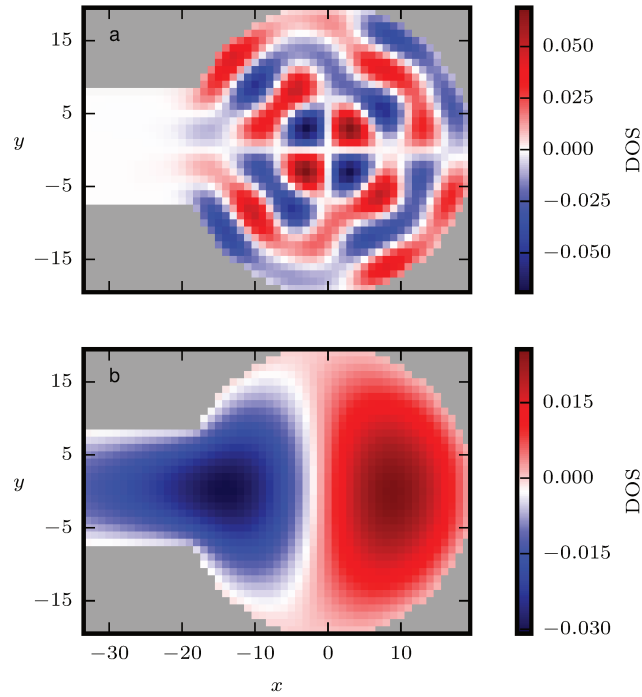


Figure 4.2: Real part of the wavefunction for two bound states of the billiard of Fig. 4.1. The parameters correspond to the white and bicolor circles (a) and (b) of Fig. 4.1. State (a) is a bound states that coexists with the continuum. State (b) was selected at an energy below (but very close to) the opening of the first mode. This way, the bound state decays only slowly in the lead and would be costly to compute by diagonalizing a truncated system.

Part III

Mostly translationally invariant systems

Simulations of quantum transport in coherent conductors have evolved into mature techniques that are used in fields of physics ranging from electrical engineering to quantum nanoelectronics and material science. The most efficient general-purpose algorithms have a computational cost that scales as $L^{6\dots7}$ in 3D, which on the one hand is a substantial improvement over older algorithms, but on the other hand still severely restricts the size of the simulation domain, limiting the usefulness of simulations through strong finite-size effects. Here, we present a novel class of algorithms that, for certain systems, allows to directly access the thermodynamic limit. Our approach, based on the Green's function formalism for discrete models, targets systems which are *mostly* invariant by translation, i.e. invariant by translation up to a finite number of orbitals and/or quasi-1D electrodes and/or the presence of edges or surfaces. Our approach is based on an automatic calculation of the poles and residues of series expansions of the Green's function in momentum space. This expansion allows to integrate analytically in one momentum variable. We illustrate our algorithms with several applications: devices with graphene electrodes that consist of half an infinite sheet; Friedel oscillation calculations of infinite 2D systems in presence of an impurity; quantum spin Hall physics in presence of an edge; the surface of a Weyl semi-metal in presence of impurities and electrodes connected to the surface. In this last example, we study the conduction through the Fermi arcs of the topological material and its resilience to the presence of disorder. Our approach provides a practical route for simulating 3D bulk systems or surfaces as well as other setups that have so far remained elusive.

Chapter 5

The motstly translationally invariant systems concept

5.1 Introduction

Quantum nanoelectronics is changing from a domain of fundamental research into one of the main platforms for development of quantum technologies. The fabrication techniques that are used in this field are related to those employed at industrial scale in microelectronics and thus hold the promise of scalable superconducting or semi-conducting quantum bits. Yet, unlike in microelectronics, where a full simulation stack for the devices is available (from the device layout to its functionalities), the modeling of quantum systems is still a work in progress with various problems remaining unsolved.

The simulation of quantum transport is one of the areas that has a long history, almost as old as quantum nanoelectronics itself^[1,56,57]. Early techniques were mostly based on the recursive Green function algorithm^[1] that was later generalized to various geometries, materials and multi-terminal systems^[2,3]. Other techniques employed wave-functions and the scattering matrix approach^[58]. Such simulations are now rather mature and open source simulation packages are becoming available^[9]. While the computational cost of these calculations is easily affordable in one ($\sim L$) and two ($\sim L^{3..4}$) dimensions, it quickly reaches prohibitive levels in three ($\sim L^{6..7}$) dimensions^[59], a case of high practical interest (L : typical length of the device). There are many situations where one must simulate large three dimensional systems: it is the case in particular for any realistic geometry; or in the presence of different characteristic length scales (such as Fermi wave length and mean level spacing); or in the case of topological materials such as 3D topological insulators or Weyl semi-metals^[60] where well-separated surfaces are important to avoid surface states mixing.

The need to simulate 3D quantum systems has provoked the development

of new methods that scale linearly with the system size. These techniques include the Kernel polynomial expansion^[5,6] and variants of the Lanczos^[61] method like Lanczos recursion method^[62,63]. See Ref. 6 for a recent review. The accuracy of these approaches increases with the number of iterations and very often they focus on local properties such as (semi-classical) conductivities or the local density of state (with exceptions such as the noticeable Ref. 64). The conductance of a coherent quantum conductor is, however, intrinsically a global quantity since it stems from the interference of spatially separated paths and new approaches must be developed to tackle this problem.

Here, we present a set of algorithms for quantum transport that work directly in the thermodynamic limit. Our approach addresses *mostly translationally invariant systems* (MTIS), i.e. systems that are translationally invariant up to a finite number of modifications. MTIS are infinite in size, and hence do not suffer from the finite size effects that often affect traditional approaches. They allow to describe many setups of practical interest such as bulk systems with impurities; bulk systems with line or surface defects; multilayer quantum wells; surfaces (half of the 3D space is filled with the material) with impurities and/or surface (topological) states and or electrodes attached to the surface; etc. Our approach takes advantage of the structure of MTIS: instead of starting from vacuum and adding new parts to the systems (the usual “bottom-up” approach), we first calculate the properties of the true translationally invariant system and then, in a second step, include the modifications (“top-down” approach). A very appealing aspect of this technique is that it naturally handles systems with very different characteristic scales as the computing cost scales as (the third power of) the number of modifications but is independent of distances.

This part is organized as follows. In chapter 5, we provide a mathematical formulation of MTIS and explain our strategy for computing their properties. Chapter 6 describes applications to a few concrete systems of interest together with some benchmarks. We discuss (i) Friedel oscillations in a Two-dimensional electron gas; (ii) the edge state properties of a 2D quantum spin Hall model; (iii) The conductance of an infinite sheet of graphene with a constriction and (iv) the multi-terminal differential conductance of the surface of a Weyl semi-metal to which has been attached quasi-1D electrodes (and impurities). Readers not interested in the technical aspects can stop at the end of Chap. 6. The rest of the chapter explains our algorithm which can be broken down into a collection of separate subproblems. The main technical challenge lies in performing a momentum integral of matrices that contain Dirac and principal part distributions. This is addressed in Sec. 7.1 using an novel algorithm for calculating poles and residues of Green’s function matrices. The other subproblems involve delicate quadrature rules for performing

Fourier transform in presence of integrable singularities (section 7.2), using the Dyson equation (section 7.3) and calculating the contributions due to bound states (section 7.4).

5.1.1 Problem formulation

In this section we introduce the concept of mostly translationally invariant systems (MTIS) and its mathematical formulation. MTIS allow to describe a great variety of quantum systems of high interest that are out of scope of traditional simulation techniques. Examples of MTIS are given in Fig. 5.1 with additional MTIS shown in the application chapter 6. The most advanced system that is studied in this thesis is the disordered surface of a Weyl semi-metal (that spans an entire 3D half-space) to which two semi-infinite quasi-one-dimensional electrodes are attached from above, as shown in Fig. 6.5.

The method presented in this part allows to simulate infinite systems whose Hamiltonians can generically be written as the sum of two terms,

$$\hat{H}_{\text{tot}} = \sum_l \hat{H}_l^\infty + \sum_a \hat{W}_a, \quad (5.1)$$

where the first one contains translationally invariant Hamiltonians, and the second one contains perturbations that break translational invariance along one or several directions and/or connect several infinite systems together. The translationally invariant systems (along one, two or three dimensions) will be called TIS hereafter.

Although not fully general, Eq. (5.1) covers a very large subgroup of tight-binding systems, including multilayer systems or the surface of a bulk material (3D half-space filled with a material). A few examples of MTIS in two dimensions are given in Fig. 5.1d-f: Fig. 5.1d shows an infinite 2D sheet where a finite number of sites have defects (vacancies, missing bonds and/or modified hoppings or on-site energies); Fig. 5.1e shows a semi-infinite 2D sheet (a system of this kind will be used to form graphene electrodes in the application section); Fig. 5.1f shows a semi-infinite sheet with a reconstruction of the edge attached to a molecule that in turn is attached to a quasi-one dimensional electrode. A three dimensional example that generalizes Fig. 5.1f is shown in Fig. 5.2h. Other examples are presented in the application sections.

The Hamiltonian matrix of TIS takes the following generic form (here-

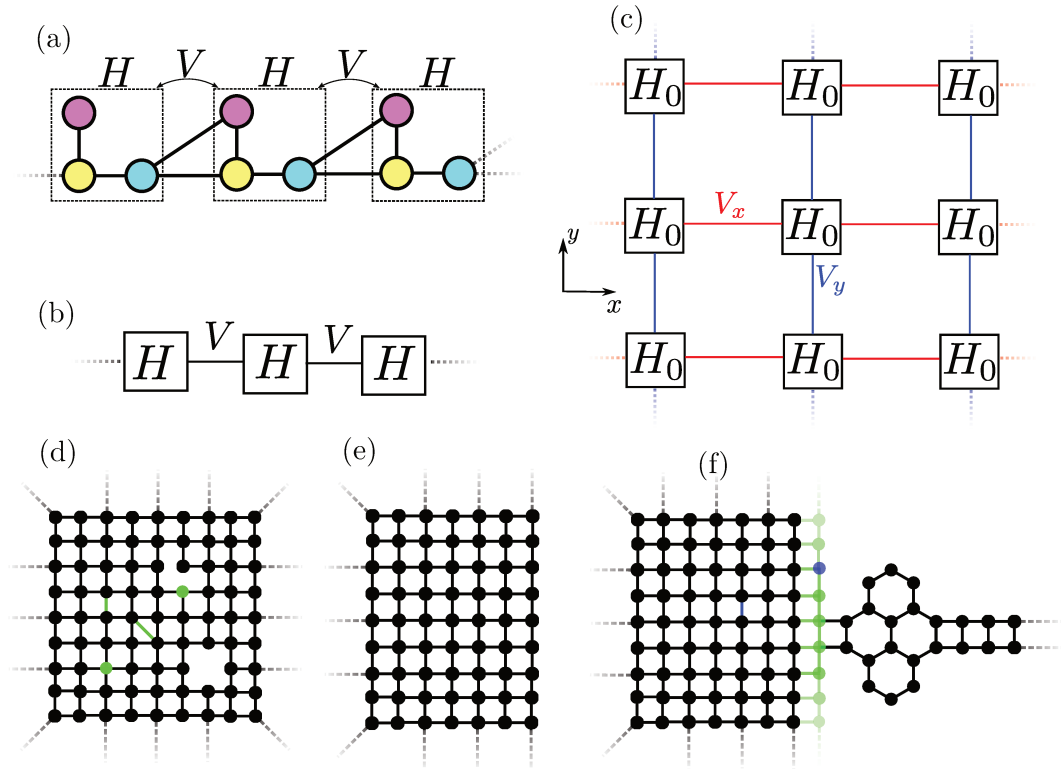


Figure 5.1: Structure and examples of MTIS. (a) Schematic representation of an infinite 1D chain with three atoms per unit cells. H and V are two 3×3 matrices respectively representing the Hamiltonian of one unit cell and the hoppings between two neighboring cells. (b) Simplified view of (a). (c) Schematic of an infinite 2D system, which extends along the x and y directions. (d-f) 2D examples of MTIS systems that can be simulated with our method. (d) A 2D infinite plane with a finite number of local defects/impurities embedded to it. (e) A semi-infinite plane, semi-infinite along x - but infinite along y . (f) A semi-infinite plane with a reconstruction of its edge (green) attached to a benzene like molecule attached to a quasi-one dimensional electrode. An impurity (blue) has been added on the edge.

after, we drop the suffix l unless needed explicitly),

$$\begin{aligned} \hat{H}^\infty = \sum_{\mu\nu} \sum_{x,y,z=-\infty}^{\infty} H_0^{\mu\nu} |x, y, z, \mu\rangle \langle x, y, z, \nu| \\ + (V_x^{\mu\nu} |x-1, y, z, \mu\rangle \langle x, y, z, \nu| \\ + V_y^{\mu\nu} |x, y-1, z, \mu\rangle \langle x, y, z, \nu| \\ + V_z^{\mu\nu} |x, y, z-1, \mu\rangle \langle x, y, z, \nu| + \text{h.c.}) \end{aligned} \quad (5.2)$$

where a ket $|x, y, z, \mu\rangle$ is labeled by the spatial positions x, y, z on the lattice as well as an orbital degree of freedom μ that accounts for spin, particle-hole, different atoms in the unit cell and/or different orbitals. The Hamiltonian matrix Eq. (5.2) contains the on-site matrix H_0 and the nearest-neighbour hopping matrices V_x, V_y and V_z along x, y and z respectively. In general, it should also include nine different diagonal hoppings such as $\hat{V}_{xy} = V_{x-y+}^{\mu\nu} |x-1, y+1, z, \mu\rangle \langle x, y, z, \nu|$. We have omitted them for clarity but the algorithms presented in this part do account for these terms. The case of second-nearest-neighbor hoppings can be represented in the above model by merging two unit cells into a larger unit cell with first-neighbor hoppings only, etc. The matrices H_0, V_x, V_y and V_z account for N_o orbitals per unit cell. Summation over the orbital degrees of freedom will often be implicit in the following. The structure of Eq. (5.2) is shown schematically in Fig. 5.1a,b (1D) and Fig. 5.1c (2D).

The second type of terms, \hat{W}_a in Eq. (5.1), breaks translational invariance along one, two or all directions. Terms that break translational invariance in all directions take the form,

$$\hat{W}_0 = \sum_{ij} W_{ij} |i\rangle \langle j|, \quad (5.3)$$

with $i = (x, y, z, \mu)$. These terms include e.g. impurities or hoppings between two infinite systems. Terms that break translational invariance along all directions but one take the form,

$$\hat{W}_1 = \sum_{z=-\infty}^{\infty} \sum_{i,j} W_{ij} |z, i\rangle \langle z, j| \quad (5.4)$$

with $i = (x, y, \mu)$. These terms describe e.g. an edge reconstruction as in Fig. 5.1f. They are also used to cut an infinite 2D sheet into two separate parts to create systems like the one shown in Fig. 5.1e (by adding the negation of the hopping V_x to the Hamiltonian at the bound to be severed). Terms that break translational invariance along all directions but two are

defined similarly,

$$\hat{W}_2 = \sum_{y,z=-\infty}^{\infty} \sum_{i,j} W_{ij} |y, z, i\rangle \langle y, z, j| \quad (5.5)$$

with $i = (x, \mu)$. The restriction that we impose on the \hat{W} matrices is that only a finite numbers of matrix elements W_{ij} may be non-zero. In practice, up to a few tens of thousand sites can be involved by each of these terms. An important aspect is that these sites need not be placed close to each other spatially. The computational cost for handling a system with e.g. 1000 impurities is independent of the distance between the impurities.

5.1.2 Principle of the technique

We now turn to the description of the method that we have developed to address the MTIS. The approach takes full advantage of the decomposition shown in Eq. (5.2) into an infinite translationally invariant and a finite arbitrary part. While the global algorithm may appear somewhat complex, it decomposes into well-defined subproblems. These subproblems have been (at least partially) resolved in the past except for one that we call the “residue problem”. The chief result of this thesis is an algorithm that solves the residue problem thereby unlocking the development of the present algorithmic suite. Below, we describe the principle of our method. The mathematical details are given in later sections.

The main mathematical object studied in this part is the retarded Green’s function of the system,

$$\hat{G}(E) \equiv \frac{1}{E - \hat{H}_{\text{tot}} + i\eta}, \quad (5.6)$$

where η is an infinitely small positive number. \hat{G} captures the single-particle propagation of the problem. In the absence of electron-electron interactions (or in a mean field treatment), the knowledge of \hat{G} is sufficient to calculate all the observables including out-of-equilibrium^[26,65,66]. Note that \hat{G} is an infinite matrix. However, only a few of its elements need to be computed, typically the matrix elements between the electrodes at the Fermi energy (conductance) or its diagonal elements at sites of interest (local density of states)^[4].

The starting point of our calculation is the Green’s function of the TIS parts,

$$\hat{g}_l(E) = \frac{1}{E - \hat{H}_l^\infty + i\eta}. \quad (5.7)$$

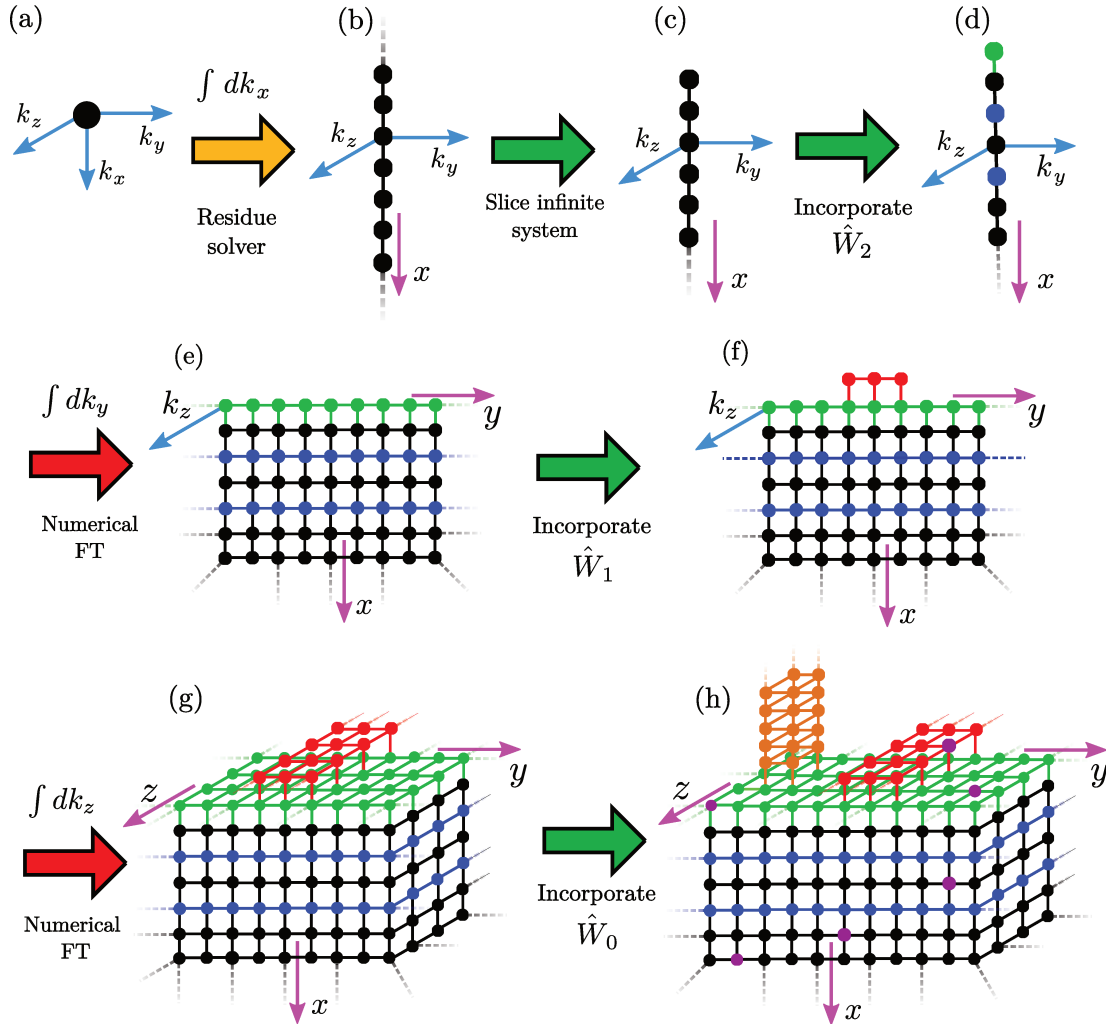


Figure 5.2: Schematic of the step by step construction of a complex 3D MTIS, see the main text for the explanation. Note the step by step passage between momentum space to real space: $k_x \rightarrow x$ (a to b), $k_y \rightarrow y$ (d to e) and $k_z \rightarrow z$ (f to g).

Since the TIS are invariant by translational, \hat{g}_l can be obtained easily in momentum \mathbf{k} -space. To calculate \hat{g}_l in real \mathbf{r} -space, one must perform a Fourier transform which formally reads,

$$\langle \mathbf{r}' | \hat{g}_l(E) | \mathbf{r} \rangle = \int_{-\pi}^{+\pi} \frac{dk_x dk_y dk_z}{(2\pi)^3} e^{i\mathbf{k} \cdot (\mathbf{r} - \mathbf{r}')} \langle \mathbf{k} | \hat{g}_l(E) | \mathbf{k} \rangle. \quad (5.8)$$

Performing this Fourier transform cannot be done using standard FFT or other quadrature approaches since the integrand contains Dirac and principal value distributions. Even using a small finite value of η to regularize the integrand, direct numerical approaches are bound to fail. We solve this problem by using integration in the complex plane and specially design tools to calculate the poles and residues of $\hat{g}(k_x, k_y, k_z, E)$ where k_x is considered as a complex variable while E , k_y and k_z are real parameters. We call the corresponding problem the residue problem. The associated “residue solver” provide the function $\langle x', k_y, k_z, E | \hat{g}_l | x, k_y, k_z, E \rangle$ which is now a well behaved regular function. Subsequent integration over k_y and eventually k_z can be performed using quadrature rules. However, we shall see that the presence of cusps and kinks make these numerical integrals somewhat delicate and they must be handled with care. Once $\langle \mathbf{r}' | \hat{g}_l | \mathbf{r} \rangle$ has been obtained, one can use standard Green’s function techniques to combine these elements with the \hat{W}_0 matrix and calculate the desired elements $\langle \mathbf{r}' | \hat{G} | \mathbf{r} \rangle$. Following Ref. 4, we call this step the glueing sequence. The matrices \hat{W}_1 and \hat{W}_2 are dealt with in a similar way before the integration over k_z (\hat{W}_1) or k_y (\hat{W}_2). During the calculation, for instance when a bond is cut between two parts of the system, new (bound) states may appear. These bound states include in particular edge or surface states present at the boundary of topological systems. We use the bound state algorithm developed in Ref. 67 to address this problem. Altogether, our MTIS algorithm consists of a non-trivial combination of the residue solver, the numerical Fourier transform solver, the glueing sequence solver and the bound state solver.

To make the above discussion more concrete, Fig. 5.2 shows the workflow of a typical 3D calculation. the starting point in Fig. 5.2a is the Green’s function of a 3D TIS given in momentum space. We use our residue solver to integrate over k_x and obtain (b) the Green’s function as a function of space (along x) and momentum (k_y, k_z). The glueing sequence is used to cut this infinite system into two and obtain a semi-infinite system (c). In this step, we also use our bound state solver to incorporate possible surface states. The semi-infinite system is modified on its surface (green) as well as within its bulk (blue) to account for the various layers that form the material. We obtain (d). We use our numerical integrator to perform the Fourier transform along k_y and obtain (e) which now depends on two spatial variables (x, y) and one momentum (k_z). We use the glueing sequence to add

a quasi-one dimensional wire deposited on the surface (red points), we obtain (f). After integration over the last momentum variable k_z , we finally obtain a 3D system in real space (g). This describes a multilayer system on the surface of which a one-dimensional wire has been deposited. This system is infinite in all the directions where shaded dashed lines are shown. We can use the glueing sequence a last time to modify this system and include impurities (purple circles) or attach the system to another MTIS (here the orange quasi-one dimensional electrode. In practice it is often useful to store the result of (g) in memory or on disk so that different kinds of steps (g)-(h) (e.g. average over disorder) can be performed at very low computational cost. A computation that applies a sequence of steps similar to the one shown in the above schematic to the surface of a Weyl semi-metal is presented in the application section 6.

In the next section, we proceed directly to actual numerical calculations for concrete systems and postpone detailed mathematical derivations of the method to Sec. 7.1 and onwards.

Chapter 6

Applications to MTIS systems

In this chapter, we consider four practical applications that demonstrate the power of the MTIS approach. The corresponding flowchart to build these three of these systems of increasing complexity is shown in Fig. 6.1. These four applications are

- *Two dimensional electron gas with an impurity.* An infinite sheet of 2D material described by a simple effective mass Hamiltonian. We introduce an impurity on one site and study the Friedel oscillations that could be observed with a scanning tunneling microscope^[68]. This calculation could actually be performed fully analytically.^[69]

- *Quantum spin Hall.* Our second example involves a 2D topological insulator^[70] that possesses edge states on its boundaries. We calculate the local density of state of a half-plane filled with this material. We emphasize that in our calculation, the system has a unique boundary in contrast with more standard calculations of a finite width ribbon that would have two boundaries (with possible overlap between the edge states due to the effect of finite width).

- *Graphene nanoribbon.* We then turn to a conductance calculation on a graphene nanoribbon. The novelty here is that the electrodes are truly two-dimensional, in contrast to more standard calculations where quasi-one dimensional electrodes are used.

- *Weyl semimetal three-terminal device.* Our last example is a full fledged three dimensional calculation of the disordered surface of a topological Weyl semi-metal to which quasi-one dimensional electrodes are attached. Our conductance calculation provides a direct evidence of the role of the Fermi-arcs which are present at the surface of Weyl semi-metals, a topic that has attracted a lot of attention recently^[71–73]. This three terminal calculation is the most complex MTIS system considered in this thesis.

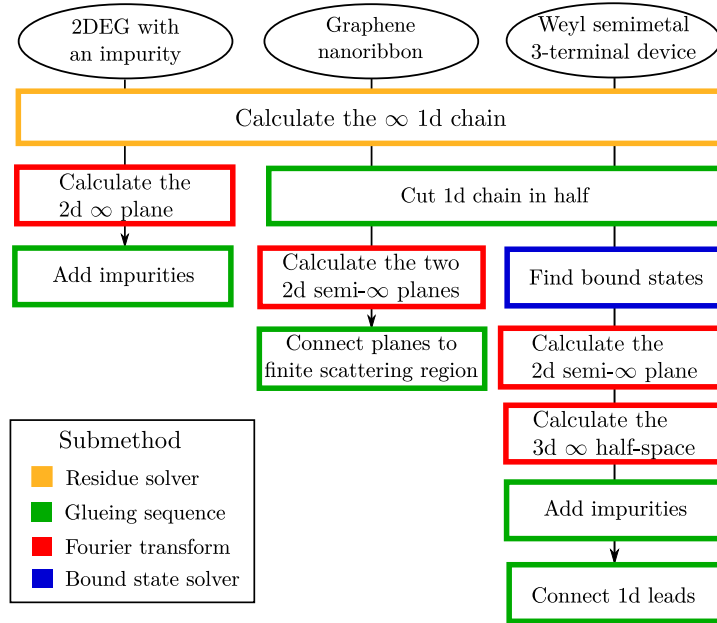


Figure 6.1: Flowchart of three different applications. The impurity in a two-dimensional gas is schematically shown in Fig. 5.1(d) and the corresponding simulation is done in Fig. 6.2. The simulation of a graphene nanoribbon is done in Fig. 6.4(d) and the Weyl device is pictured in the two first insets of Fig. 6.5. The residue solver is derived in Sec. 7.1, the Fourier transform is shown in Sec. 7.2. The glueing sequence is extensively described in Ref. 4 and the idea is pictured in Sec. 7.3. Finally, the bound state solver is derived in Ref. 67.

6.1 Friedel oscillations in a two-dimensional electron gas

For starters, let us consider a very simple Hamiltonian on an infinite 2D square lattice

$$\hat{H}_{2D} = \sum_{x,y} [|x+1, y\rangle \langle x, y| + |x, y+1\rangle \langle x, y|] + \varepsilon |0, 0\rangle \langle 0, 0| \quad (6.1)$$

where ε shifts the on-site energy of the site $|0, 0\rangle$ which describes an impurity. The TIS part of this model is defined with one on-site and two hopping 1×1 matrices

$$\begin{aligned} H_0 &= 0, \\ V_x &= 1, \\ V_y &= 1. \end{aligned} \quad (6.2)$$

We calculate the Local Density Of States (LDOS) close to the impurity. This quantity is directly measured by a scanning tunneling microscope in the tunneling regime^[68]. It is related to the GF with

$$\rho(\mathbf{r}, E) = -\frac{1}{\pi} \text{Im}(\langle \mathbf{r} | G(E) | \mathbf{r} \rangle) \quad (6.3)$$

and is plotted in Fig. 6.2 (after subtraction of its bulk value far from the impurity). A top view at fixed energy is shown in panel (a) for the MTIS (c). Although a finite portion of space (here around 5000 sites, the calculations being easily done on a laptop) is calculated, the system is actually infinite - there are no effects of boundaries that influence the calculation. The LDOS exhibits standard Friedel oscillations $\rho(\mathbf{r}) \sim \cos(2k_F r)/r^2$ where k_F is the Fermi momentum.

The advantage of the MTIS approach is most apparent when the calculation of Fig. 6.2a is contrasted with a more standard approach. In Fig. 6.2b, we used the Kwant software^[9] to calculate the “cross” geometry of panel (d) (a $L \times L$ square to which 4 quasi-one dimensional electrodes of width L are attached). The boundary effects in sample (d) are clearly present near the edges in the colormap (b) and provide a distortion of the Friedel oscillations. In addition, these calculations are much more computationally intensive since the computational effort scales as L^3 . As a benchmark, Fig. 6.2e compares the two calculations for the two line cuts shown in Fig. 6.2a and b. In order to get a quantitative match between the two approaches, a very large value of L must be used, as shown in Fig. 6.2f.

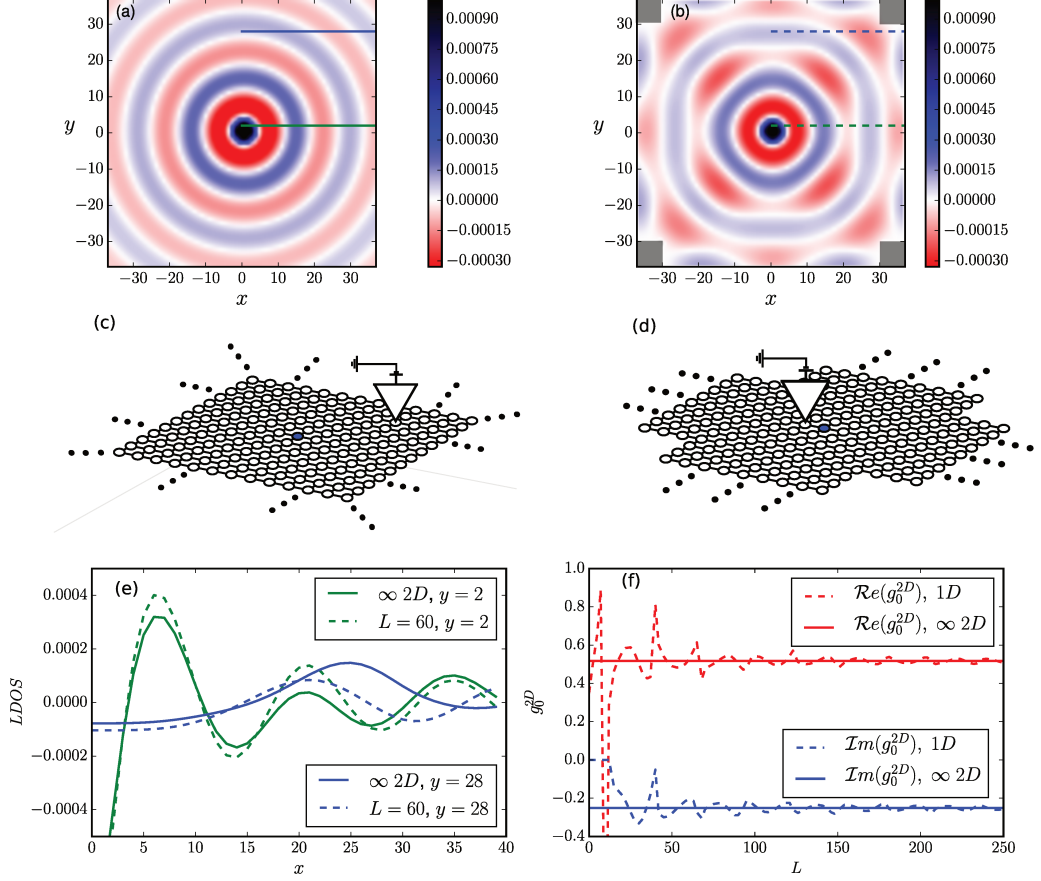


Figure 6.2: Disordered two dimensional electron gas. (a) LDOS due to the impurity of the model from Eq. (6.1), at $E = 3.95$, $\varepsilon = 0.05$. (b) Same LDOS simulated with a quasi-1d system, shown in (d). (c) is a representation of (a), a 2d infinite plane with an impurity on one site. (d) is a representation of (b). The system is shaped like a cross which arms extend to infinity, more precisely a square scattering region with 4 infinite leads attached to it and an impurity in the middle. (e) LDOS of the finite and infinite systems along the green and blue lines in subplots (a) and (b). (f) shows the convergence of g_0^{2D} (computed on the impurity, the furthest point from the edges) in function of the scattering region size l . We emphasize that it is faster (besides being exact) to simulate the system (a) than (b).

6.2 Quantum spin hall effect

We continue with a second model where we now use a non-trivial 4×4 unit cell. We consider the BHZ model^[70] for the quantum spin Hall, a two-dimensional topological insulator. Topological insulators are gapped in the bulk but have conducting edge states on the boundary. It is therefore important to consider a system with an edge to observe these edge states, and we consider a semi-infinite 2D sheet. The continuous BHZ model

$$\mathcal{H}_{\text{BHZ}}(\mathbf{k}) = \begin{pmatrix} h(\mathbf{k}) & 0 \\ 0 & h^*(-\mathbf{k}) \end{pmatrix}, \quad (6.4)$$

with

$$h(\mathbf{k}) = \epsilon(\mathbf{k}) + \vec{d}(\mathbf{k}) \cdot \vec{\sigma},$$

and

$$\begin{aligned} \epsilon(\mathbf{k}) &= C - D(k_x^2 + k_y^2), \\ \vec{d}(\mathbf{k}) &= (Ak_x, -Ak_y, M - B(k_x^2 + k_y^2)). \end{aligned}$$

The vector $\vec{\sigma} = (\sigma_x, \sigma_y, \sigma_z)$ consists of the Pauli matrices while A, B, C, D and M are the parameters of the model.

We consider a discretized tight-binding model that corresponds to \mathcal{H}_{BHZ} in the continuum limit where the momenta $\mathbf{k} \rightarrow 0$. It is given by,

$$\begin{aligned} H_0 &= (C - 4D)\sigma_0 + (M - 4B)\sigma_z, \\ V_x &= D\sigma_0 + B\sigma_z + \frac{1}{2i}A\sigma_x, \\ V_y &= D\sigma_0 + B\sigma_z - \frac{1}{2i}A\sigma_y. \end{aligned} \quad (6.5)$$

The rule for constructing the tight-binding Hamiltonian are as follows: one first perform the transformation $k_{x/y}^2 \rightarrow 1 - \cos k_{x/y}$ and $k_{x/y} \rightarrow \sin k_{x/y}$ for quadratic and linear terms, respectively. In a second step, one identifies the constant terms with H_0 and the terms proportional to e^{-ik_x} (e^{-ik_y}) with V_x (V_y).

We consider a sample made of a pristine semi-infinite sheet of this topological material, as shown in the inset of Fig. 6.3a. Fig. 6.3a shows the local density of states (LDOS) as a function of energy E , $\rho(x, E) = -\text{Tr} \text{Im} \langle \mathbf{r} | G(E) | \mathbf{r} \rangle / \pi$ at three different distances from the edge. We also plot the bulk DOS of the infinite sheet (i.e. the value of the LDOS infinitely far from the edge). The latter shows a vanishing DOS inside the gap $[-0.7, 0.7]$ of the system. The non-zero values of the LDOS inside the gap for the semi-infinite sheet is due to the presence of the propagating edge states. Note that all quantities here are independent of y as all systems are invariant by translation along that

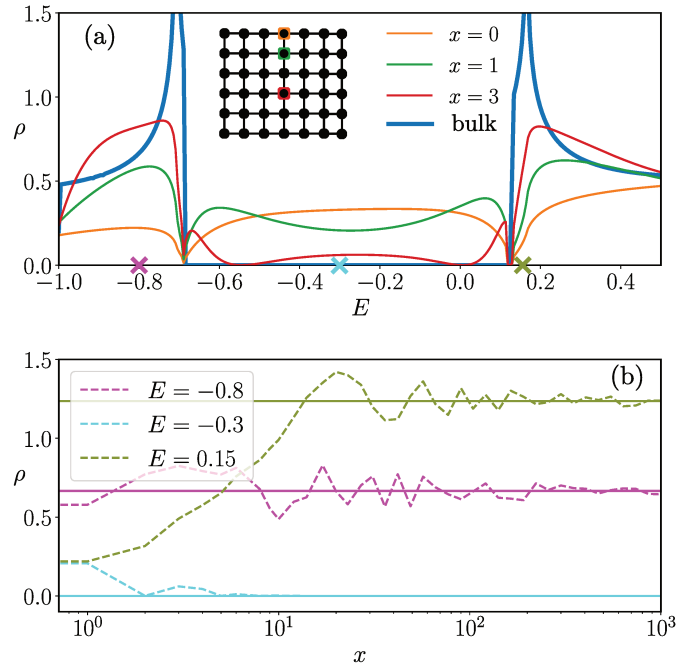


Figure 6.3: The quantum spin hall model on a semi-infinite plane. (a) LDOS of the quantum spin hall in function of energy for a bulk system (infinite in the x - and y -directions) in blue and for a semi-infinite system (semi-infinite in the x -direction) at a position $x = 0, 1$ and 3 from the boundary, as pictured by the colored dots in the inset. The crosses on the E -axis correspond to the energies plotted in (b). (b) LDOS of a semi-infinite system (dashed lines) in function of the distance to the boundary. The horizontal lines represent the LDOS of a bulk system.

direction. As the distance from the boundary is increased, the edge states amplitude decrease exponentially which leads to a corresponding decrease of the LDOS inside the gap.

Figure 6.3b shows a calculation of the LDOS versus x for the three energies marked by crosses in Fig. 6.3a. We observe a slow (algebraic) convergence to the (independently calculated) bulk limit for the two values of energy inside the spectrum, characteristic of the Friedel oscillations created by the presence of the edge. Inside the gap, we observe a much faster exponential convergence towards zero due to the exponential localization of the edge states. We emphasize again that the computational time to obtain this data is totally independent of the value of x used in the calculation, in sharp contrast with standard approaches.

6.3 Graphene nanoribbon

We now turn to a quantum transport problem, the calculation of the conductance of a graphene nanoribbon coupled to two semi-infinite graphene sheet. This calculation is in contrast with standard quantum transport calculations where one uses quasi-1D leads of finite width W . Here, we work directly in the thermodynamic limit $W = \infty$. The geometry of the calculation is shown in Fig. 6.4d. We note that this system could also be addressed with the technique of Ref. 74. It uses an iterative Lanczos like approach that leverages on the existence of the nanoribbon constriction to restrict the Hamiltonian to the states connected to the constriction. It is an orthogonal (possibly complementary) approach to the present one which exploits translational invariance.

The Hamiltonian of the system is the standard nearest neighbor Hamiltonian on a honeycomb lattice restricted to the geometry of Fig. 6.4d,

$$\hat{H}_G = \sum_{\langle i,j \rangle} |i\rangle \langle j|. \quad (6.6)$$

In the algorithm, we first calculate the Green's function of the two semi-infinite 2D graphene sheet and then proceed to connect them to the central nanoribbon using Dyson equation.

Following the standard formalism^[66], the differential conductance $g_{ll'} = dI_{ll'}/dV_{l'}$ between electrode l' and l is given in terms of the total transmission probability $g_{ll'} = (e^2/h)T_{ll'}$ with

$$T_{ll'} = \text{Tr}(\hat{G}\Gamma_l\hat{G}^\dagger\Gamma_{l'}), \quad (6.7)$$

with \hat{G} the GF of the total system,

$$\Gamma_l = i(\Sigma_l - \Sigma_l^\dagger), \quad (6.8)$$

and the lead self energy Σ_l is given by,

$$\Sigma_l = W_l G_l W_l^\dagger. \quad (6.9)$$

In the above definition, G_l is the surface Green's function of the graphene electrode, here a semi-infinite 2D graphene sheet. W_l corresponds to the matrix elements of the Hamiltonian that connect the central ribbon to the electrode l .

Figure 6.4a shows the transmission between the two 2D leads as a function of the energy. The dots show the calculation for electrodes that have a finite width parametrized by W while the plain blue line corresponds to the MTIS calculation with $W = \infty$. The dashed line shows the result of a

calculation with $W = 0$, i.e. for an infinite ribbon. In this case, the conductance is quantized and the total transmission simply counts the number of conducting sub-bands at the Fermi level. The presence of the sharp widening on both sides of the ribbon creates reflexion which in turns creates a Fabry-Perot cavity.^[74] The associated interference pattern is at the origin of the peaks in the conductance versus energy plot.

For large value of the energy (typically $E > 1$), we find that the finite width data is almost undistinguishable from the $W = \infty$ curve. A plot of the convergence at $E = 1.3$ is shown in Fig. 6.4c. In this regime, the MTIS approach has nevertheless a clear computational advantage as the computational cost of the finite width quasi-1D electrodes scales as W^3 . With our current implementation, we find that computing directly the $W = \infty$ limit is faster than the finite width calculation as soon as $W \geq 100$ for $E = 0.5$. For smaller values of the energy, we observe a clear difference between the finite W data and the $W = \infty$ case. This is to be expected since, for small E , the associated wave length $\lambda \sim 1/E$ becomes comparable to W and finite size effect take place. The apparent noise in the finite W data is due to fast oscillations in energy. Fig. 6.4b shows the convergence of the result as a function of W for a fixed energy $E = 0.15$. Unlike the high energy case, we find that the convergence towards the $W = \infty$ limit (blue horizontal curve) is slow and oscillatory. In this limit, accessing the correct large W physics with standard finite W techniques is extremely difficult.

6.4 Weyl semimetal three terminal device

We end this application section with a last calculation that showcase the full power of the MTIS approach. We consider a 3D topological Weyl semi-metal with impurities on its surface and calculate the differential conductance of a three terminal geometry. This calculation combines the difficulties of addressing an infinite 3D system (half of the space is filled with the 3D material) with disorder, in a multiterminal geometry and in presence of surface states (the so-called Fermi arcs). The geometry of the device is shown in Fig. 6.5a with a top view shown in 6.5b.

We consider a 3D 4-band model of a Weyl semimetal defined as^[54]

$$\begin{aligned} \mathcal{H}_{\text{WEYL}}(\mathbf{k}) = & \tau_z [t(\sigma_x \sin(k_x) + \sigma_y \sin(k_y)) + t_z \sigma_z \sin(k_z)] \\ & + \mu(\mathbf{k}) \tau_x \sigma_0 + \frac{1}{2} b_0 \tau_z \sigma_0 + \frac{1}{2} \beta \tau_0 \sigma_z, \end{aligned} \quad (6.10)$$

with

$$\mu(\mathbf{k}) = \mu_0 + t(2 - \cos(k_x) - \cos(k_y)) + t_z(1 - \cos(k_z)),$$

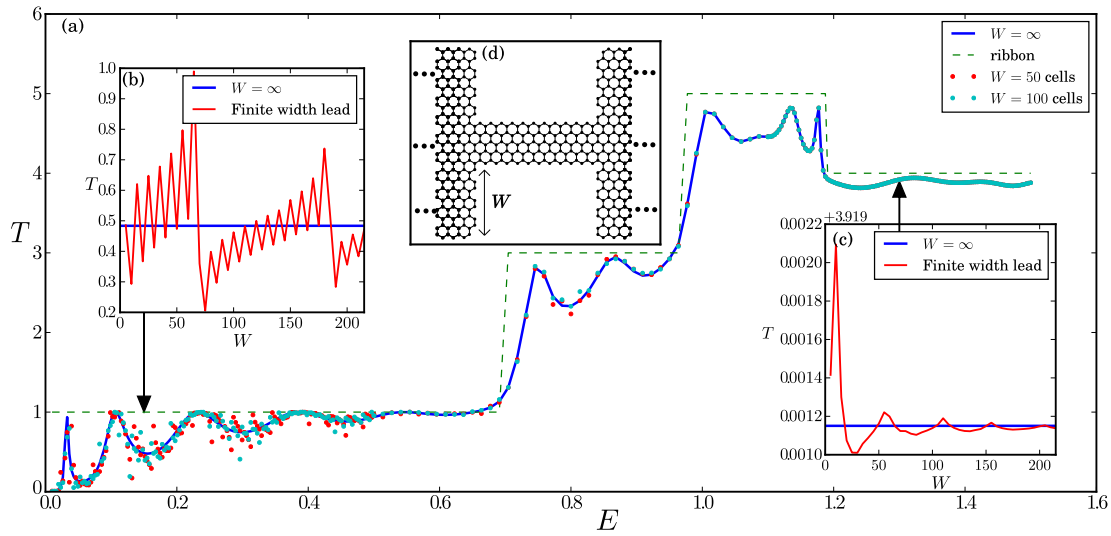


Figure 6.4: Graphene nanoribbon connected to two semi-infinite 2D electrodes (blue line) or to two finite width quasi-1D electrodes (symbols). Main panel (a): Transmission $T(E)$ versus energy E . The dashed line indicates the $W = 0$ situation. (b) Transmission versus width W for the fixed value of the energy $E = 0.15$ shown by the black arrow. The horizontal blue line shows the MTIS calculation $W = \infty$. (c) Same as (b) for $E = 1.3$. (d) Schematic of the system. The electrodes extend to infinity on the right and on the left. In the $W = \infty$ MTIS case, the leads also extend to infinity to the bottom and the top.

and the Pauli matrices τ_i and σ_i ($i = x, y, z$) act respectively on the orbital and spin degree of freedom. We use the parameters $t = 2$, $t_z = 1$, $\mu_0 = -0.1$, $b_0 = 0$ and $\beta = 1$. After discretization, the on-site H_0 and hopping V_x , V_y and V_z matrices are given by,

$$\begin{aligned} H_0 &= (\mu_0 + 2t + t_z)\tau_x + \frac{1}{2}b_0\tau_z + \frac{1}{2}\beta\sigma_z, \\ V_x &= \frac{1}{2}it\tau_z\sigma_x - \frac{1}{2}t\tau_x\sigma_0, \\ V_y &= \frac{1}{2}it\tau_z\sigma_y - \frac{1}{2}t\tau_x\sigma_0, \\ V_z &= \frac{1}{2}it_z\tau_z\sigma_z - \frac{1}{2}t_z\tau_x\sigma_0. \end{aligned} \quad (6.11)$$

The geometry of Fig. 6.5a consists of a Weyl semimetal that fills half of the 3D space (all $x \geq 0$ and all y and z) to which two quasi-1D electrodes are connected. We also add some impurities on the surface. The complex sequence of submethods used to calculate the differential conductance of this geometry is presented in Fig. 6.1. The quasi-1D electrodes are considered to be normal metals described by a hopping and a on-site parameters with respectively $t = 1$ and $\mu = 0$. The transverse width of this electrodes used in the simulations is 5×5 . In the following, the quasi-1D electrodes are labeled as 1 and 2, and the infinite Weyl semi-metal is labeled as 0. The conductance matrix that relates the current I_a to the voltage V_b applied to lead b takes the form,

$$\begin{pmatrix} I_0 \\ I_1 \\ I_2 \end{pmatrix} = \frac{e^2}{h} \begin{pmatrix} T_{02} + T_{01} & -T_{01} & -T_{02} \\ -T_{10} & N_1 - R_{11} & -T_{12} \\ -T_{20} & -T_{21} & N_2 - R_{22} \end{pmatrix} \begin{pmatrix} V_0 \\ V_1 \\ V_2 \end{pmatrix}, \quad (6.12)$$

where $N_a = \sum_j T_{lj} = \sum_j T_{jl}$ is the number of channels in the quasi-1D electrode a . The conductance matrix conserves current and is "gauge invariant" in the Buttiker sense, i.e. raising simultaneously all voltages creates zero current^[75]. Notice the special treatment of the 0 electrode: as R_{00} and N_0 are both infinite, only their difference is well a defined quantity. The total reflection terms R_{aa} are given by,^[22]

$$\begin{aligned} R_{aa} &= N_a + \text{Tr}(\Gamma_a \hat{G} \Gamma_a \hat{G}^\dagger) + \\ & i(\text{Tr}(\Gamma_a \hat{G}) - \text{Tr}(\Gamma_a \hat{G}^\dagger)). \end{aligned} \quad (6.13)$$

where G_a is the Green's function of the full system at the surface of quasi-1D electrode electrode.

We now present the results of the calculation for a clean surface. We suppose the geometry of Fig. 6.5b where one electrode is fixed on the surface (Ohmic contact) while we scan the surface with the second one (tip

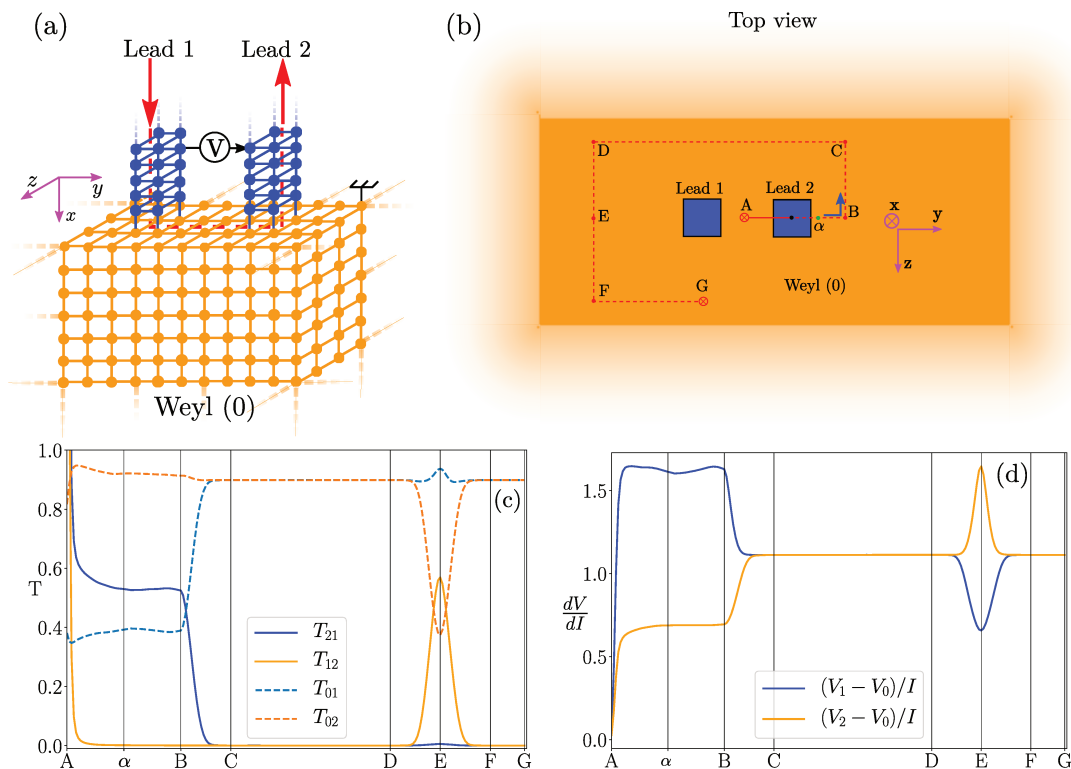


Figure 6.5: Weyl semimetal three-terminal device. (a) Two squared one-dimensional leads (5×5 sites in the simulations) in blue are connected to the surface of a 3D semi-infinite Weyl semimetal (in orange). The Weyl semimetal part spans the yz -plane for all $x \leq 0$. (b) Same as (a) but cut perpendicularly from the z -axis. The dashed line indicates the trajectory followed by lead 2. The green point labeled by α indicates the position of lead 2 in the plot of Fig. 6.7. (c) Transmissions in between the leads (0 is the Weyl semimetal, 1 and 2 the two blue leads) at $E = 0.02$ as the right lead is moved from A, where the two blue leads are in contact, to G following the path shown in (a). The distance AB correspond to 55 sites and BC to 25 sites. (d) Differential resistance plotted along the path shown in (a), where V_1 and V_2 are the tensions in the two leads. The Weyl part is connected to the ground, such that the current can only come in or out in the 1D leads.

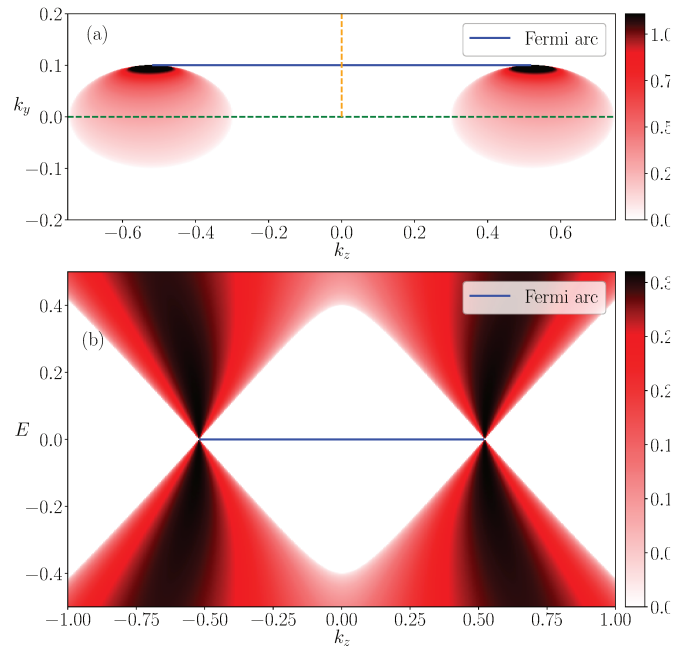


Figure 6.6: LDOS of a semi-infinite Weyl semimetal. (a) LDOS of the semi-infinite system as a function of k_y and k_z , at $E = 0.2$. The blue line connecting the cones is a bound state, the so-called Fermi arc. The orange and green curves respectively correspond to the matrix elements plotted in figures 7.3 and 7.2. (b) LDOS of the semi-infinite system as a function of k_z and E , at $k_y = 0$.

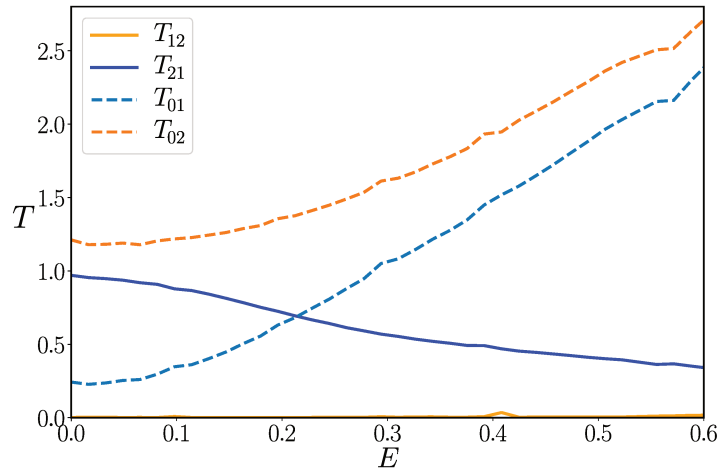


Figure 6.7: Transmission between the two leads as function of the energy. The leads contain 25 sites and are similar to simulations shown in Fig. 6.5c and d. Lead 2 is located 25 sites away from lead 1, as indicated by the point α in Fig. 6.5b, c and d. This length is sufficient to reach the plateau of T_{21} between points A and B.

of a scanning tunneling microscope moving on the surface). The different letters ABCDEFG indicate the trajectory of the STM tip on the surface. Figure 6.5(c) shows the different transmissions between the different electrodes as a function of the position of the STM tip on its trajectory for a value of the energy close to the Weyl points.

At this value of the energy, the bulk density of state is very small and transport is entirely dominated by the surface states, the so-called Fermi arcs. These arcs are extremely anisotropic with a dispersion relation $E = vk_y$ so that they only propagate along the y direction in the *positive* direction. It follows that transport between electrode 1 and 2 is only possible when they are aligned along the y -direction; and only from 1 to 2 not from 2 to 1. This is illustrated by the curves between A and B where $T_{21} \approx 0.55$ and $T_{12} \approx 0$. As soon as this alignment is lost, both T_{21} and T_{12} vanish and all the current goes to the substrate. Note that the above results are closely linked to the band structure of the model considered here which only contains one pair of Weyl points. In real materials, there might be several pairs of such points^[76] and surface reconstruction can also lead to a bending of the Fermi arcs^[77] which would lead to a decrease of the extreme anisotropy observed in our numerics.

Intermediate steps in the calculation of the above transport curve involve the computation of the Fermi arcs wavefunction, first in momentum space and then in real space. This information is necessary to analyze the

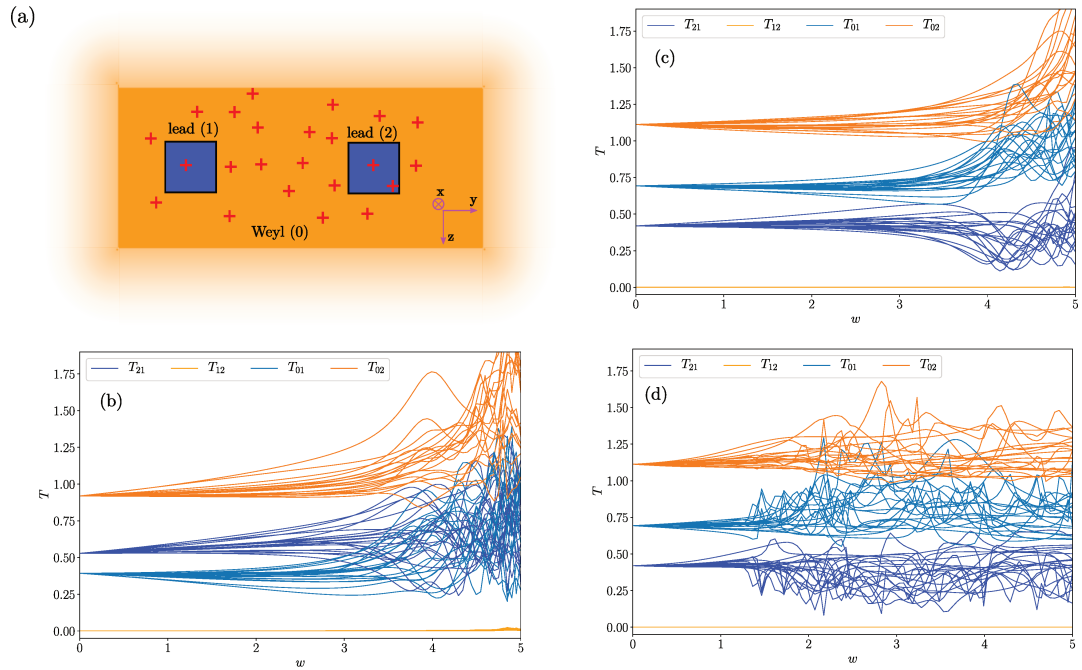


Figure 6.8: Transmission of the disordered Weyl surface. (a) The two leads are placed on the surface at $r_1 = (0, -20, 0)$ and $r_2 = (0, 20, 0)$. 30 impurities are scattered randomly on the surface around the leads in the rectangle $-6 < z < 6$ and $-30 < y < 30$, so that the impurity density is 5% in that rectangle. (b) Transmissions between the leads and the bulk as a function of the strength of the impurity at $E = 0.02$. Same color correspond to the same transmissions for 20 different samples (distribution of impurities). (c) Same as (b), for $E = 0.2$, (d) Same as (c), but a random impurity matrix is chosen on each site.

final calculation of observables. Fig. 6.6 shows the local density of state of the pristine surface $\rho(x, k_y, k_z, E) = -\text{Tr} \text{Im} \langle x, k_y, k_z | G(E) | x, k_y, k_z \rangle / \pi$ (colorplot) while the blue line indicates the position of the Fermi arc. From such plots, one can read e.g. the dispersion relation of the Fermi arcs.

Figure 6.7 shows the different transmissions as a function of energy E when the STM tip is positioned at point A'. The transmission towards the bulk increases quadratically which is consistent with a linear density of state in the bulk (dashed lines). More interestingly the transmissions T_{21} and T_{12} are very weakly affected by the presence of the bulk states and remain very anisotropic ($T_{12} \approx 0$). Hence, transport on the surface is very weakly affected by the presence of the bulk states and remains dominated by the Fermi arcs^[78].

Figure 6.5d shows the differential conductance measured across the two top contacts in the following setup: one inject a current I in electrode 1 and retrieve the same current in electrode 2 (vanishing current leaves electrode 0). The strong anisotropy observed in the two non-local resistances $(V_1 - V_0)/I$ and $(V_2 - V_0)/I$ bears the signature of the Fermi arc anisotropy.

We now turn to the study of the resilience of the above picture to the presence of disorder. While disorder in bulk Weyl semimetal has been the focus of several studies^[79–82] the effect on the surface has received much less attention^[73]. We consider discrete impurities randomly scattered at the surface in the region around the leads, see Fig. 6.8a

We model the impurities by modifying 5% of the on-site Hamiltonian matrices located around the leads (20 to 30 sites) which to we add a shift in energy $w \cdot \mathcal{K}_4$ (Fig. 6.8b and c) or a fully random on-site matrix $w \sum_{i,j} h_{i,j} \sigma_i \tau_j$ where $h_{i,j}$ are randoms number in $[-1, 1]$ (Fig. 6.8d). Different traces correspond to different samples.

In the low energy regime of Fig. 6.8b, $E = 0.02$, the effect of the impurities is only significant for a large value of w comparable to the bandwidth of the model (equal to ~ 5), which indicates that the anisotropic transport on the surface is resistant to the presence of disorder. This is not unexpected since at this energy the density of bulk states to scatter to is very low. However, the same behaviour is observed in Fig. 6.8b for an energy ten times larger, $E = 0.2$. The resilience to disorder remains when we use the random matrix disorder of Fig. 6.8d that breaks all possible symmetries. We conclude that the topological protection of the Fermi arcs can directly be observed in the differential conductance which is not perturbed by the presence of the bulk states. Our observations are compatible with the statement that disorder only renormalizes the dispersion relation^[73], which persist to be non zero even close to Anderson localization.

Chapter 7

Analytical and numerical techniques in MTIS solver

7.1 The Residue problem

We now turn to the detailed derivation of our formalism and algorithms. Our first goal is to calculate a finite set of matrix elements for the Green's function of a TIS, i.e. $\langle \mathbf{r}', \mu | \hat{g}_l(E) | \mathbf{r}, \nu \rangle$ for a set of values $(\mathbf{r}', \mu, \mathbf{r}, \nu)$. The Green's function of the TIS is formally defined as the inverse of the Hamiltonian (shifted in energy),

$$\hat{g}_l(E) = \frac{1}{E - \hat{H}_l^\infty + i\eta}. \quad (7.1)$$

Since the TIS is invariant by translational, \hat{H}_l^∞ can be diagonalized in momentum space. The momentum states $|\alpha\mathbf{k}\rangle$ satisfy $\hat{H}_l^\infty|\alpha\mathbf{k}\rangle = E|\alpha\mathbf{k}\rangle$ and take the form,

$$|\alpha\mathbf{k}\rangle = \sum_{\mathbf{r}, \mu} \Psi_{\alpha\mathbf{k}}(\mu) e^{i\mathbf{k}\cdot\mathbf{r}} |\mathbf{r}, \mu\rangle \quad (7.2)$$

where the eigenvectors $\Psi_{\alpha\mathbf{k}}$ are eigenstates

$$\mathcal{H}(k)\Psi_{\alpha\mathbf{k}} = E(\mathbf{k})\Psi_{\alpha\mathbf{k}} \quad (7.3)$$

of the momentum Hamiltonian,

$$\begin{aligned} \mathcal{H}(k) \equiv & H_0 + V_x^\dagger e^{ik_x} + V_x e^{-ik_x} + \\ & V_y^\dagger e^{ik_y} + V_y e^{-ik_y} + V_z^\dagger e^{ik_z} + V_z e^{-ik_z} \end{aligned} \quad (7.4)$$

We arrive at the following expression for $\langle \mathbf{r}', \mu | \hat{g}_l(E) | \mathbf{r}, \nu \rangle$,

$$\langle \mathbf{r}', \mu | \hat{g}_l(E) | \mathbf{r}, \nu \rangle = \sum_{\alpha} \int_{-\pi}^{+\pi} \frac{d^3\mathbf{k}}{(2\pi)^3} e^{i\mathbf{k}\cdot(\mathbf{r} - \mathbf{r}')} \frac{\Psi_{\alpha\mathbf{k}}(\mu)\Psi_{\alpha\mathbf{k}}^*(\nu)}{E - E(\mathbf{k}) + i\eta} \quad (7.5)$$

7.1.2 Solution to the residue problem

Here we provide without justification the solution of the Residue problem. The proof of this result is given in the rest of the section. The first step of the algorithm is to solve the generalized eigenvalue problem

$$[E - \mathcal{H}(k)]\phi = 0, \quad (7.14)$$

where E is an *input* and we seek the values of k for which the above equation has a solution ϕ . We emphasize that this is a very different problem from diagonalizing $\mathcal{H}(k)$ for a given value of k . Introducing explicitly the form of $\mathcal{H}(k)$, Eq. (7.14) takes the form,

$$\begin{pmatrix} H - E & V^\dagger \\ 1 & 0 \end{pmatrix} \begin{pmatrix} \phi \\ \xi \end{pmatrix} = \frac{1}{\lambda} \begin{pmatrix} -V & 0 \\ 0 & 1 \end{pmatrix} \begin{pmatrix} \phi \\ \xi \end{pmatrix} \quad (7.15)$$

which is indeed a generalized eigenproblem. Here, we have introduced $\lambda = e^{ik}$. Solving this problem numerically can be handled by e.g. the Kwant numerical package^[9]. The second step is to sort the corresponding set of eigenvectors/eigenvalues (ϕ_a, λ_a) into two categories *left* goers and *right* goers. Eigenstates with $\lambda_a < 1$ ($\lambda_a > 1$) go into the right (left) goers category. Eigenstates with $|\lambda_a| = 1$ are classified according to the velocity v_a ,

$$v_a = \phi_a^\dagger V^\dagger e^{ik_a} - V e^{-ik_a} \phi_a. \quad (7.16)$$

States with positive (negative) velocity are right (left) goers. The third step is to construct the projectors P_λ on the different subspaces spanned by the ϕ_a

$$P_\lambda = \sum_{\lambda_a = \lambda} \phi_a \phi_a^\dagger. \quad (7.17)$$

The special case of the projector P_0 corresponds to the projector onto the kernel of V ($VP_0 = 0$). Introducing the matrix,

$$\partial_k \mathcal{H}(k) = i(V^\dagger e^{ik} - V e^{-ik}), \quad (7.18)$$

the result of the calculation reads,

$$g_x^{\text{1D}}(E) = \sum_{\lambda} i\lambda^x P_\lambda \frac{1}{E - \mathcal{H}(\lambda) - \partial_k \mathcal{H}(\lambda) P_\lambda} + \delta_{x,0} P_0 \frac{1}{[(E - H)P_0 + V]}. \quad (7.19)$$

where the sum is extended onto the right goers for $x \geq 0$ and onto the left goers for $x < 0$. Eq. (7.19) is the chief analytical result of this thesis. It provides a fast and stable solution to the Residue problem. The computation of a set of different values of x involves only some linear algebra on small $N_o \times N_o$ matrices. The matrices in front of the λ^x terms can be cached so that the computational effort to obtain N_x different values of x (for a fixed energy) scales as $N_o^4 + N_o^2 N_x$.

7.1.3 Proof of Eq. (7.19)

In the first step of the proof, we extend the integral of Eq. (7.12) onto the complex k -plane. For $x \geq 0$, we use the red contour shown in Fig. 7.1 which consists of four branches: the integral over Γ_1 is the original integral, the integrals over Γ_2 and Γ_4 compensate by symmetry of the integrand and the integral over Γ_3 is evaluated in the limit where the horizontal segment Γ_3 goes to infinity. For $x < 0$, we use the mirror green contour. For $x \neq 0$, the factor λ^x in the integrand is exponentially small which makes the integral over Γ_3 to vanish in the limit $\kappa \rightarrow \infty$, where κ is the imaginary part of the momentum. Applying Residue theorem to this contour integral, we arrive at,

$$g_x^{\text{1D}}(E) = \sum_{\lambda} \text{Res} \left(\frac{i\lambda^x}{E - \mathcal{H}(\lambda)} \right) - \lim_{\kappa \rightarrow \infty} \int_{-\pi}^{\pi} \frac{dk}{2\pi} \frac{\delta_{x,0}}{E - \mathcal{H}(k + i\kappa)} \quad (7.20)$$

where the first term accounts for the residues of the integrand evaluated at its poles and the second to the integral over the Γ_3 segment.

Let us focus on the first part of this expression, the residues. The first step consists in finding the poles of the integrand of Eq. (7.12). These poles correspond to the values k_a solution of Eq. (7.14). These poles are either in the upper half plane $\Im m k_a > 0$ (right goes) or lower half plane $\Im m k_a < 0$ (left goes). The fate of the non-evanescent solutions with $\Im m k = 0$ is found by remembering the existence of the infinitely small positive η . To obtain the residues, we need to calculate the expansion of the integrand close to the pole. We start by expanding $\mathcal{H}(k)$ around k_a ,

$$E - \mathcal{H}(k_a + q) = [E - \mathcal{H}(k_a)] - \partial_k \mathcal{H}(k_a) q - \partial_k^2 \mathcal{H}(k_a) \frac{q^2}{2} + \dots \quad (7.21)$$

where we note that high derivatives of $\mathcal{H}(k_a)$ are simply related to the lower ones: $\partial_k^n \mathcal{H}(k_a) = -\partial_k^{n-2} \mathcal{H}(k_a)$ for $n \geq 3$. We now seek the expansion of $1/[E - \mathcal{H}(k_a + q)]$ around $q = 0$. The key point to notice here is that since $[E - \mathcal{H}(k_a)]$ is not invertible, this expansion has a term proportional to $1/q$ that we need to calculate to apply the residue theorem. The algebra to obtain in a systematic way the coefficients of the development of $1/[E - \mathcal{H}(k_a + q)]$ is given in Appendix B.1. We obtain,

$$\frac{1}{E - \mathcal{H}(k_a + q)} = \sum_{n=-1}^{+\infty} \frac{1}{q^n} D_n(k_a) \quad (7.22)$$

with

$$D_{-1} = P_{\lambda_a} \frac{1}{E - \mathcal{H}(k_a) - \partial_k \mathcal{H}(k_a) P_{\lambda_a}} \quad (7.23)$$

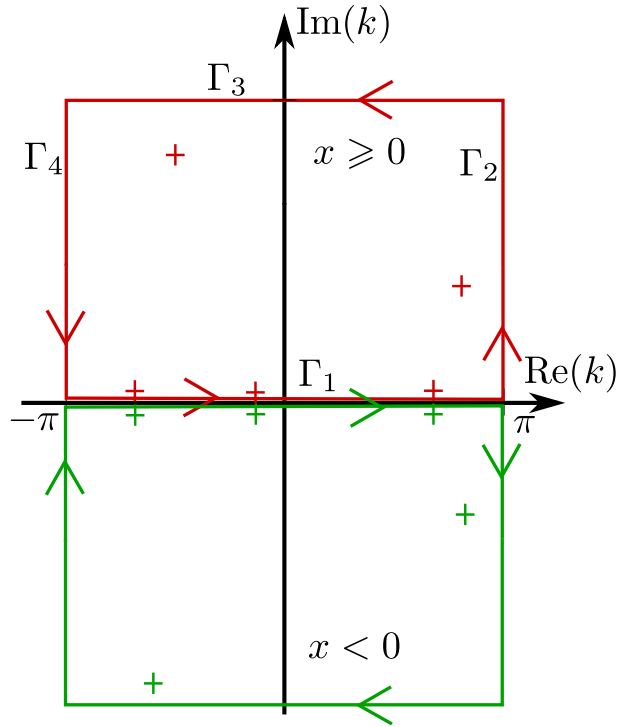


Figure 7.1: The two possible path integrals in the complex plane. The segments on the real axis goes from $-\pi$ to π so it correspond to the bounds of Eq. (7.12). The crosses show the localization of the poles corresponding to solutions of Eq. (7.14). The red ones correspond to right goers and the green ones to left goers. The integration is performed on the red (green) contour if $x \geq 0$ ($x < 0$). Each pole come in pair because for a solution λ there is a corresponding solution $\frac{1}{\lambda^*}$. The three propagative modes ($|\lambda| = 1$) are located at an infinitely small distance η from the real axis.

Applying residue theorem with the above expression for the matrix residue D_{-1} provides the first term of Eq. (7.20). Although we did not encounter the case in practice, it is possible that the matrix $E - \mathcal{H}(k_a) - \partial_k \mathcal{H}(k_a) P_{\lambda_a}$ above is not invertible. In that case the sum in Eq. (7.22) starts at -2 . Appendix B.1 provides a systematic iterative construction of the residue in that case. Appendix B.1 also provides a general algorithm to calculate the other coefficients D_n if ever needed.

Let us now calculate the second term of Eq. (7.20), the integral over the Γ_3 segment of the contour which is only present when $x = 0$. When κ is large, one gets from the definition of $\mathcal{H}(k)$,

$$E - \mathcal{H}(k + i\kappa) = e^{\kappa - ik} [-V + (E - H_0)e^{-\kappa + ik}] + \mathcal{O}(e^{-\kappa}). \quad (7.24)$$

We need to integrate $1/[E - \mathcal{H}(k + i\kappa)]$ over k . If the matrix V is invertible, then the second term of the development is not necessary: $1/[E - \mathcal{H}(k + i\kappa)] \approx -e^{-\kappa + ik} V^{-1}$ and the integrand (hence the integral) vanishes in the limit $\kappa \rightarrow +\infty$. However, if V is not invertible, the expansion of $1/[-V + (E - H_0)e^{-\kappa + ik}]$ in power of $e^{-\kappa + ik}$ has a pole $\propto e^{\kappa - ik}$ which provides a term of order $\mathcal{O}(1)$ in the integrand. Using the result of Appendix B.1, we obtain,

$$\frac{1}{-V + (E - H_0)e^{-\kappa + ik}} = \frac{1}{e^{-\kappa + ik}} P_0 \frac{1}{(E - H)P_0 - V} + \mathcal{O}(1) \quad (7.25)$$

It follows that the integrand of the second term of Eq. (7.20) is k -independent and can be calculated explicitly. This concludes the proof of Eq. (7.19).

7.2 Numerical Fourier transform

Once the integration over k_x has been done using the complex integration technique described in the preceding section, the expression of the TIS Green's function Eq. (7.5) takes the form,

$$g_{x,y,z}^{3D}(E) = \int_{-\pi}^{\pi} \frac{dk_y dk_z}{(2\pi)^2} e^{i(k_y y + k_z z)} g_x^{1D}(k_y, k_z) \quad (7.26)$$

where $g_x^{1D}(k_y, k_z)$ is the result of the residue solver. In this section, we focus on the case where the system extends on the full 3D space, $-\infty \leq x \leq +\infty$. To study, e.g. a surface with $-\infty \leq x \leq 0$, one need to introduce intermediate steps before the integration over k_y and k_z . These steps are discussed in the sections that follows the present one.

The integration over k_y and k_z is performed using a standard quadrature approach where the interval $[-\pi, +\pi]$ is broken into small subintervals and the integrand is approximated with polynoms on each subintervals. A typical example of the integrand is shown in Fig. 7.2. We observe that it possesses

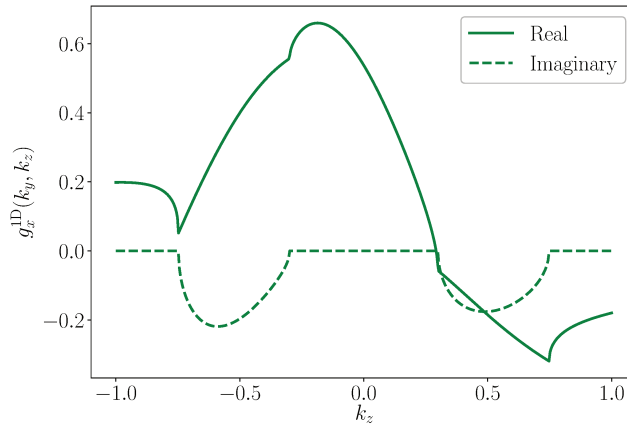


Figure 7.2: Typical integrand in Eq. (7.26). $[g_x^{1D}(k_y, k_z)]_{11}$ is plotted as a function of k_z at $k_y = 0$ along the green dotted line in Fig. 6.6a for the surface of a Weyl semi-metal.

a number of cusps and kinks, so that the integration over momentum is somewhat delicate. To obtain reliable results in a robust way, we have found that the doubly adaptating scheme of Ref. 83 is particularly efficient. Of prime importance is the algorithm used to evaluate the residual error of the integral, that allows one to compute $g_{x,y,z}^{3D}(E)$ to a given precision. We plan to release an efficient implementation of the resulting algorithm as open source software^[?].

7.3 The glueing sequence

In this section, we explain how to use Dyson equation to introduce modifications to the TIS Green's function. This step has been discussed in the past in different contexts^[2,4,84,85]. An alternative, equivalent, formalism uses the so-called T matrix approach^[86,87]. Here, we follow the knitting algorithm discussed in Ref. 4.

Let us suppose that the Hamiltonian of the system splits into two contribution \hat{H} and \hat{W} . Typically \hat{H} is the Hamiltonian of the TIS system and \hat{W} a perturbation that involves only a *finite* number of sites. However, we shall see below that we can be slightly less restrictive. We suppose that we have already calculated the Green's function $\hat{g}(E)$ of the TIS and we seek

the Green's function $\hat{G}(E)$ of the full Hamiltonian,

$$\hat{g} = \frac{1}{E - \hat{H} + i\eta}, \quad (7.27)$$

$$\hat{G} = \frac{1}{E - (\hat{H} + \hat{W}) + i\eta}. \quad (7.28)$$

The starting point for this calculation is a simple equation valid for any two matrices A and B ,

$$\frac{1}{A+B} = \frac{1}{A} - \frac{1}{A}B\frac{1}{A+B}. \quad (7.29)$$

In the present context, it translates into,

$$\hat{G} = \hat{g} + \hat{g}\hat{W}\hat{G} \quad (7.30)$$

which is known as the Dyson equation. Eq. (7.30) involves infinite matrices. Let us introduce the set of points Ω which is the support of the matrix \hat{W} : $\forall i, j \notin \Omega, W_{ij} = 0$. The crucial property of the Dyson equation is that its projection on any finite set of points Θ that contains Ω forms a close set of equations,

$$\forall i, j \in \Theta, \quad \hat{G}_{ij} = \hat{g}_{ij} + \sum_{k,l \in \Omega} \hat{g}_{ik} \hat{W}_{kl} \hat{G}_{lj} \quad (7.31)$$

which can be solved using standard linear algebra routines. More formally, we introduce the projectors P_Ω and P_Θ defined as

$$P_\Theta = \sum_{i \in \Theta} \sum_{\mu\nu} |i, \mu\rangle \langle i, \nu| \quad (7.32)$$

with a similar definition for P_Ω . The finite matrix $\hat{G}_{\Omega\Theta} = P_\Omega \hat{G} P_\Theta$ is given by,

$$\hat{G}_{\Omega\Theta} = \frac{1}{1 - \hat{g}_{\Omega\Omega} \hat{W}_{\Omega\Omega}} \hat{g}_{\Omega\Theta}. \quad (7.33)$$

In a second step, one calculates $\hat{G}_{\Theta\Theta} = P_\Theta \hat{G} P_\Theta$,

$$\hat{G}_{\Theta\Theta} = \hat{g}_{\Theta\Theta} + \hat{g}_{\Theta\Omega} \hat{W}_{\Omega\Omega} \hat{G}_{\Omega\Theta} \quad (7.34)$$

The above sequence allows one to introduce any finite number of modifications to a system whose corresponding Green's function elements are known. Following Ref. 4, we call it the glueing sequence. It is a straightforward generalization of the basic sequence at the root of the recursive Green's function algorithm. Denoting N_Ω and N_Θ the number of elements of the respective sets, the computational cost of the glueing sequence scales as $N_\Omega N_\Theta^2$ (non local properties such as transport) or $N_\Omega^2 N_\Theta$ (local properties such as local density of states). This cost is independent of the system size (which

is infinite) and only depends on the number of modifications and points of interest.

In the MTIS part, we use the glueing sequence in different situations that we list below.

Point like impurities. The simplest application of the glueing sequence is to modify some on-site energies, or some hopping elements. In this case, we strictly follow the sequence given above. An example of such a calculation is the inclusion of on-site disorder in the application on Weyl semi-metal discussed in Sec. 6.4. If one is interested in calculating averages over impurity configurations, then only the last stage of the calculation, the glueing sequence, need to be recalculated for each sample. Hence, these averages can be relatively unexpensive computationally. This approach has been used previously in the context of disordered graphene^[88]. In Ref. 89 the TIS Green's function has been obtained analytically through a route that is similar to the route that we have followed numerically.

Attaching two systems together The glueing sequence can also be used to connect two systems together, e.g. the semi-infinite 2D graphene sheet to the graphene nanoribbon described in Fig. 6.4. In this case the Dyson equation has an additional structure, as the unperturbed Green's function is block diagonal (the two subsystems are initially unconnected). This structure may be used to simplify the algebra of the glueing sequence, see Ref. 4.

Creating a multilayer system. The general matrices \hat{W}_2 introduced in Sec. 5 do not have a finite number of terms, but it conserves momentum along two directions y and z . It can be cast in the form,

$$\hat{W}_2 = \int_{-\pi}^{\pi} \frac{dk_y dk_z}{(2\pi)^2} \sum_{i,j \in \Omega} W_{ij} |k_y, k_z, i\rangle \langle k_y, k_z, j|. \quad (7.35)$$

Hence, for a given value of k_y, k_z , i.e. *before* we have performed the numerical integration on these variables, \hat{W}_2 takes the form of a finite perturbation and we may apply the glueing sequence. Such a step allows one to create e.g. multilayer systems. The above equation is actually not fully general. A straightforward extension is to consider matrices $W_{ij}(k_y, k_z)$ that include an explicit dependance on momentum. Terms of the class \hat{W}_1 are treated in a similar fashion.

Slicing a system in two. A particular example of perturbation of the \hat{W}_2 class is when the perturbation is exactly opposite to one bond V_x .

$$\hat{W}_2 = \sum_{y,z,\mu,\nu} -[V_x]_{\mu\nu} |0, y, z, \mu\rangle \langle 1, y, z, \nu| + h.c. \quad (7.36)$$

In that case the perturbation slices the system and creates two disconnected systems. This what we used to create the semi-infinite 2D graphene sheet as well as the surface of the Weyl semi-metal. It is important to notice

that upon slicing, one may create bound states (1D), edge states (2D) or surface states (3D). In particular in topological materials, these states (that we refer collectively as bound states) are always present. Bound states may also appear in the multilayer example above. How to properly deal with bound states will be discussed in the next section. In the applications shown in this thesis, we focus on surfaces on the [100] direction. The same technique can be extended to other surfaces such as [110] by simply enlarging the unit cell so that [110] becomes effectively [100] for the large unit cell.

7.4 The bound state problem

The last problem that must be addressed is the appearance of bound states in the system. These states appear in a large variety of situations that include slicing the system (creation of a surface), in multilayers (quantum wells), in Josephson junctions or around impurities. In the present part, the edge states of the quantum spin Hall effect and the surface states (Fermi arcs) of the Weyl semi-metals are (generalized) bound states. Bound states do not hybridize with the continuum and must therefore be handled as separate contributions. In MTIS, bound states may be invariant by translation upon zero (true bound states), one (edge states) or two directions (surface states). To simplify the discussion, we focus below on surface states. The results can be straightforwardly extended to the other situations.

Suppose that we have used the residue solver to construct the TIS Green's function $g_x(E, k_y, k_z)$ for fixed values of the transverse momentum (k_y, k_z) . In a second step, we have use the glueing sequence to slice the system and obtain $G_{x,x'}(E, k_y, k_z)$ where the system terminates at $x = 0$ (Fig. 5.2c). The contribution of a bound state $\psi_\alpha(k_y, k_z)$ with energy $E(k_y, k_z)$ to $G_{x,x'}(E, k_y, k_z)$ takes the form

$$\lim_{\eta \rightarrow 0} \frac{\psi_\alpha(x, k_y, k_z) \psi_\alpha^\dagger(x', k_y, k_z)}{E - E_\alpha(k_y, k_z) + i\eta} \quad (7.37)$$

$\lim_{\eta \rightarrow 0} 1/(X + i\eta) = p.v.(1/X) - i\pi\delta(X)$ so that the presence of a bound state leads to two complications: (i) the principal value cannot be integrated with numerical routines as the integral is formally divergent. (ii) The Dirac function associated with the divergence at $E = E_\alpha(k_y, k_z)$ is not captured by $G_{x,x'}(E, k_y, k_z)$. Numerically, one only observes a numerical instability of $G_{x,x'}(E, k_y, k_z)$ for values of (k_y, k_z) such that $E = E_\alpha(k_y, k_z)$. An example of the integrand observed after the slicing sequence is shown in Fig. 7.3 where we indeed observe the behaviour discussed above.

To proceed, one needs first to calculate the bound states independently. For all technical details, refer to part II or the article (Ref. 67). We suppose that we have computed the energy $E_\alpha(k_y, k_z)$ and the associated state $\psi_\alpha(x, k_y, k_z)$ of the semi-infinite problem. Once this is done, we numerically

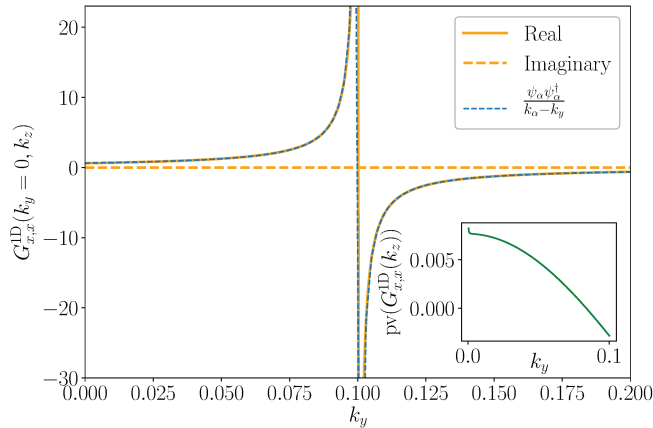


Figure 7.3: Behavior of the integrand around the surface state (Fermi arc) of the Weyl semi metal. $[G_x^{1D}(k_y, k_z)]_{22}$ as a function of k_y at $k_z = 0$ along the orange dotted line in Fig. 6.6a. The fit $\psi_\alpha \psi_\alpha^\dagger / (\bar{k}_y - k_y)$ is only indicative and is not used in the analysis. The inset shows the regularized integrand, see text.

inverse the function $E_\alpha(k_y, k_z)$ to obtain $k_\alpha = \bar{k}_y(E, k_z)$. Our goal is to perform the integration over the k_y variable and calculate,

$$G_{xy, x'y'}(E, k_z) = \int_{-\pi}^{+\pi} \frac{dk_y}{2\pi} e^{ik_y(y-y')} G_{x, x'}(E, k_y, k_z) \quad (7.38)$$

(i) *Regularizing the principal value.* The problem of the presence of the principal value is easily handled once one has evaluated the function $k_\alpha = \bar{k}_y(E, k_z)$. We follow the standard procedure for handling principal values and select a small interval $[k_\alpha - \epsilon, k_\alpha + \epsilon]$. In this interval, we use the symmetrized integrand defined as follows,

$$\int_{k_\alpha - \epsilon}^{k_\alpha + \epsilon} \frac{dk_y}{2\pi} F(k_y) = \int_0^{+\epsilon} \frac{dq}{2\pi} [F(k_\alpha + q) + F(k_\alpha - q)] \quad (7.39)$$

where $F(k_y) = e^{ik_y(y-y')} G_{x, x'}(E, k_y, k_z)$. The symmetrized integrand that gives the principal value of the real part plotted in Fig. 7.3 is displayed in the inset of the same figure. We find that although the original integral was divergent, this procedure correctly regularizes the integral. Subtracting $\psi_\alpha \psi_\alpha^\dagger / (k_\alpha - k_y)$ to $G_{x, x'}(E, k_y, k_z)$ could also regularize the integral. Indeed the dashed line of Fig. 7.3 perfectly fits the GF divergence at the bound state momenta.

(ii) *Contribution from the Dirac function.* We now evaluate the contribution of the bound state due to the Dirac function,

$$\int_{-\pi}^{+\pi} \frac{dk_y}{2i} e^{ik_y(y-y')} \psi_\alpha(x, k_y) \psi_\alpha^\dagger(x', k_y) \delta[E - E_\alpha(k_y)] \quad (7.40)$$

where we have dropped the k_z dependence for compactness. Performing this integral, we arrive at

$$\frac{1}{2i} e^{ik_\alpha(y-y')} \psi_\alpha(x, k_\alpha) \psi_\alpha^\dagger(x', k_\alpha) \left| \frac{\partial E_\alpha}{\partial k_y} \right|^{-1}. \quad (7.41)$$

The last step is to calculate $\partial E_\alpha / \partial k_y$. In the case of a simple slicing where the system is invariant by translation away from the boundary, it is given by

$$\begin{aligned} \frac{\partial E_\alpha}{\partial k_y} &= \psi_\alpha^\dagger \frac{\hat{H}_{1D}}{\partial k_y} \psi_\alpha \\ &= \frac{i}{1 - |\lambda_\alpha|^2} \psi_\alpha^\dagger(x=0) [V_y^\dagger e^{ik_y} - V_y e^{-ik_y}] \psi_\alpha(x=0) \end{aligned} \quad (7.42)$$

where λ_α is the evanescent momentum of the bound state. For more complicated cases, e.g. a coated surface, there is a contribution from the part that is not invariant by translation, that plays the role of the scattering region in Ref. 67.

To summarise this section, the result of the integral over k_y is given by,

$$\begin{aligned} G_{xy, x'y'}(E, k_z) &= \frac{1}{2i} e^{ik_\alpha(y-y')} \psi_\alpha(x, k_\alpha) \psi_\alpha^\dagger(x', k_\alpha) \left| \frac{\partial E_\alpha}{\partial k_y} \right|^{-1} \\ &+ \int_{k_y \notin [k_\alpha - \epsilon, k_\alpha + \epsilon]} \frac{dk_y}{2\pi} e^{ik_y(y-y')} G_{x,x'}(E, k_y, k_z) \\ &+ e^{ik_\alpha(y-y')} \int_0^{+\epsilon} \frac{dq}{2\pi} \left[e^{iq(y-y')} G_{x,x'}(E, k_\alpha + q, k_z) \right. \\ &\quad \left. + e^{-iq(y-y')} G_{x,x'}(E, k_\alpha - q, k_z) \right] \end{aligned} \quad (7.43)$$

Each of the integrals can now be performed using the numerical techniques discussed in Sec. 7.2.

7.5 Conclusion

Despite being ubiquitous, quantum transport simulations face severe limitations in a number of situations where large systems must be simulated.

This is in particular the case of most 3D systems. The Mostly Translational Invariant Systems (MTIS) that we have discussed in this part encompass a significant fraction of systems of interest that were inaccessible to simulations up to now. We have presented a general method that can handle arbitrary MTIS, and demonstrated the power of the approach on a number of situations. The advantage of the MTIS approach stems from the fact that one works directly in the thermodynamic limit. Not only does the computational cost not depend on the size of the (infinite) system, but it also independent on distances such as the distance between two impurities. It is therefore a natural tool for systems that possess several different characteristic length scales. The precision of the method is limited by the numerical integrals and can be pushed to numerical accuracy.

We have studied the transport properties of the surface of a Weyl semi-metal. In our calculation, there is a single surface present as the opposite second surface that would be present in a finite size calculation is sent infinitely far away. Getting rid of the second surface greatly simplifies the calculations and their interpretations. Our approach could be used for other surface problems such as the formation of Majorana bound states around magnetic impurities on top of a superconductor^[90] or the study of the Dirac cones at the surface of a 3D topological insulators^[91] or more generally for simulating scanning tunneling microscope (STM) experiments.

For quantum transport, MTIS provides the possibility to use 2D or 3D electrodes such as the semi-infinite graphene sheet that we have presented. These electrodes are often more realistic than the quasi-1D electrodes used in almost all approaches. They are also less computationally intensive in most situations. We expect these electrodes to quickly become a standard feature of quantum transport toolkits.

MTIS also encompass many applications that we have barely discussed so far. For pure bulk systems, they could be used for the study of defects, (RKKY) interaction between magnetic impurities or to calculate the collision integrals that enter the semi-classical Boltzman equation. The MTIS approach can be trivially combined with the recursive Green's function approach and its generalization to build complex geometries.

Conclusion

In the field of quantum nanoelectronics, simulations of realistic devices faces severe limitations. In particular, numerical calculations of quantum transport often suffer from finite size effects, especially in 3D systems. The Mostly Translational Invariant Systems (MTIS) approach together with the bound state solver that we have discussed in this thesis covers a significant fraction of systems of interest that were out of reach to simulations up to now. This is made possible because both the bound state and the MTIS solvers computational cost do not depend on the size of the (infinite) system. It is therefore a natural tool for systems that possess very different characteristic length scales. Both methods suffer from no approximation, and can be pushed to numerical accuracy.

We demonstrated the usefulness of these approaches on a number of quantum systems, e.g. on topological materials thanks to the bound state solver. Indeed, a proper way to treat bound states in these (semi-) infinite systems is mandatory. This is delicate since bound states should be treated differently than the continuum. Combining the solvers for both bound state and MTIS, we were able for instance to simulate quantum transport in a disordered Weyl semimetal. In our calculation, there is only a single surface present as the opposite second surface that would be present in a finite size calculation is sent infinitely far away. Eliminating the second surface greatly simplifies the calculations and their interpretations.

Both solvers paves the way for future applications. In the following, we present some potential applications that the solvers could simulate out of a huge variety of device and materials, so these applications are by no means exhaustive.

For quantum transport, MTIS also provides the possibility to use 2D or 3D electrodes such as the semi-infinite graphene sheet that we have presented. These electrodes are often more realistic than the quasi-1D electrodes used in almost all approaches. Knowing the properties (that is, the exact self-energy) of these generalized leads also allows one to simulate proximity effects due to superconducting electrodes. For instance one could simulate superconducting three-dimensional aluminum electrodes^[92,93]. We expect

such generalized leads to become a standard feature of quantum transport toolkits.

Among the potential applications, the most promising ones are the three-dimensional devices. The recent emergence of the class of topological materials provided condensed matter physicists with a variety of novel phenomena^[37,53,60]. This thesis provides methods to exactly simulate properties of these materials also for three-dimensional devices. Indeed, the possibility of simulating isolated surfaces containing bound states (or surface states) is a significant advantage compared to traditional algorithms. For instance, the two approaches could be applied to surface problems such as the formation of Majorana bound states around magnetic impurities on top of a superconductor^[90], or the study of the superconductivity in Weyl semimetals induced by proximity effects. The MTIS method can be used not only as a theoretical tool but also provides a direct access to quantities close to experimental data, e.g. a scanning tunneling microscope measurement.

Last but not least, MTIS also encompass many applications with pure 3D bulk systems that we have barely discussed so far. One could study the scattering off defects, (RKKY) interaction between magnetic impurities or compute the collision integrals that enter the semi-classical Boltzman equation.

Appendix A

Bound state appendix

A.1 Normalization of the bound state

Bound states should be correctly normalized:

$$\psi_{\text{sr}}^\dagger \psi_{\text{sr}} + \sum_{j \geq 1} \psi_\alpha(j)^\dagger \psi_\alpha(j) = 1. \quad (\text{A.1})$$

However, our algorithm does not ensure this normalization automatically. For a given set $(\psi_{\text{sr}}, q_{e,\alpha})$ we find that

$$\psi_{\text{sr}}^\dagger \psi_{\text{sr}} + \sum_{j \geq 1} \psi_\alpha(j)^\dagger \psi_\alpha(j) = \psi_{\text{sr}}^\dagger \psi_{\text{sr}} + q_{e,\alpha}^\dagger \left[\sum_{j \geq 1} (\Lambda_e^\dagger)^j \Phi_e^\dagger \Phi_e (\Lambda_e)^j \right] q_{e,\alpha}. \quad (\text{A.2})$$

We recognize a geometric series and arrive at

$$\psi_{\text{sr}}^\dagger \psi_{\text{sr}} + \sum_{j \geq 1} \psi_\alpha(j)^\dagger \psi_\alpha(j) = \psi_{\text{sr}}^\dagger \psi_{\text{sr}} + q_{e,\alpha}^\dagger N q_{e,\alpha}, \quad (\text{A.3})$$

with the matrix N defined as

$$N_{mn} \equiv \frac{1}{1 - \lambda_n \lambda_m^*} \lambda_n \lambda_m^* (\Phi_e^\dagger \Phi_e)_{m,n}. \quad (\text{A.4})$$

Eq. (A.3) can now be used to normalize the bound state wave functions to unity.

A.2 Proof of Eq. (3.13)

To prove Eq. (3.13), we begin by multiplying Eq. (3.6) by Φ_e^\dagger :

$$\Phi_e^\dagger V \Phi_e + \Phi_e^\dagger (H - E) \Phi_e \Lambda_e + \Phi_e^\dagger V^\dagger \Phi_e (\Lambda_e)^2 = 0. \quad (\text{A.5})$$

The complex conjugate of the above equation reads

$$(\Lambda_e^*)^2 \Phi_e^\dagger V \Phi_e + \Lambda_e^* \Phi_e^\dagger (H - E) \Phi_e + \Phi_e^\dagger V^\dagger \Phi_e = 0. \quad (\text{A.6})$$

Now, multiplying Eq. (A.5) by Λ_e^* on the left and Eq. (A.6) by Λ_e on the right, we arrive after subtracting one equation from the other at

$$[\lambda_\alpha^* - (\lambda_\alpha^*)^2 \lambda_\beta] \Phi_e^\dagger V \Phi_e \Big|_{\alpha\beta} = [-\lambda_\alpha^* (\lambda_\beta)^2 + \lambda_\beta] \Phi_e^\dagger V^\dagger \Phi_e \Big|_{\alpha\beta}. \quad (\text{A.7})$$

Since we are dealing with evanescent states, we can simplify by $1 - \lambda_\alpha^* \lambda_\beta \neq 0$ and arrive at

$$\lambda_\alpha^* \Phi_e^\dagger V \Phi_e \Big|_{\alpha\beta} = \lambda_\beta \Phi_e^\dagger V^\dagger \Phi_e \Big|_{\alpha\beta} \quad (\text{A.8})$$

which is essentially Eq. (3.13).

A.3 Degenerate eigenvalues

In some cases, the solutions λ of Eq. (3.3) can be degenerate, as in the quantum spin Hall model of Sec. (4.2.2) where the degeneracies arise because of the two species of spin. A set of degenerate eigenvectors is not uniquely defined, as any linear combination is still a valid solution of the eigenproblem (3.3). This means that the matrix Φ_e that was introduced in Sec. 3.2.3 can be replaced by $\Phi_e' \equiv \Phi_e T$, where T is an invertible matrix equal to unity except in the block corresponding to degenerate eigenvalues. This modification results in an uncertainty of the l.h.s. of Eq. (3.14) since

$$H_{\text{eff}}'(E) \equiv \begin{pmatrix} H_{\text{sr}} - E & P_{\text{sr}}^T V^\dagger \tilde{\Phi}_e' \tilde{\Lambda}_e \\ \tilde{\Lambda}_e^* \tilde{\Phi}_e'^\dagger V P_{\text{sr}} & -\tilde{\Lambda}_e^* \tilde{\Phi}_e'^\dagger V \tilde{\Phi}_e' \end{pmatrix} \quad (\text{A.9})$$

$$= \begin{pmatrix} 1 & 0 \\ 0 & T^\dagger \end{pmatrix} \begin{pmatrix} H_{\text{sr}} - E & P_{\text{sr}}^T V^\dagger \tilde{\Phi}_e \tilde{\Lambda}_e \\ \tilde{\Lambda}_e^* \tilde{\Phi}_e^\dagger V P_{\text{sr}} & -\tilde{\Lambda}_e^* \tilde{\Phi}_e^\dagger V \tilde{\Phi}_e \end{pmatrix} \begin{pmatrix} 1 & 0 \\ 0 & T \end{pmatrix} \quad (\text{A.10})$$

does not have the same eigenvalues as H_{eff} , unless T is unitary. (We use the fact that Λ_e commutes with T .) This leads to a problem during the root-finding phase of the algorithms of Sec. 3.3.1 and 3.3.3: in a naive implementation H_{eff} is evaluated multiple times for different E , each time with an effectively random T . The resulting fluctuations, shown in Fig. A.1(a), are incompatible with efficient root-finder routines. The algorithm presented in 3.3.4 is not considered here as the derivatives computed in that section are not well defined for degenerate eigenvalues.

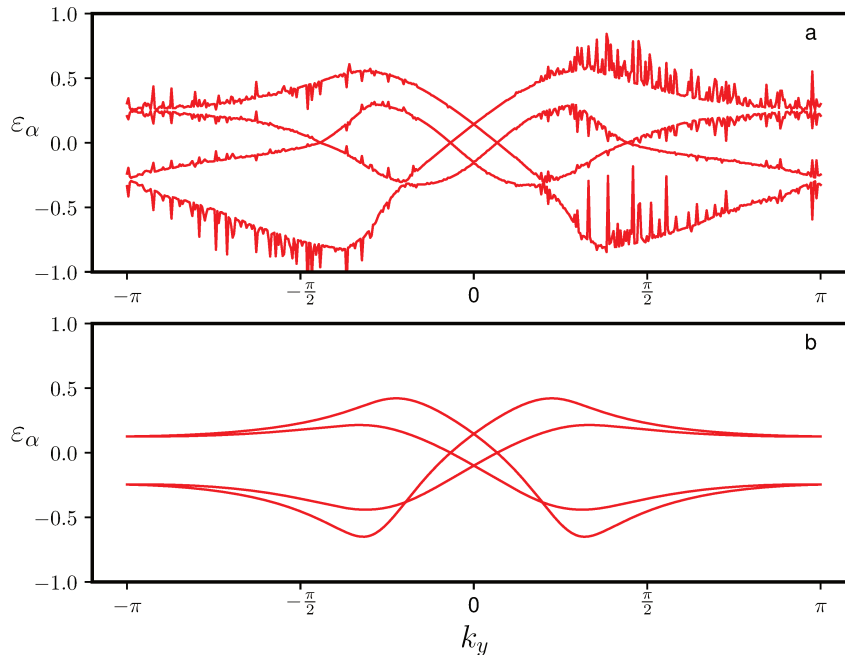


Figure A.1: Eigenvalues of $H_{\text{eff}}(E, k)$ for the quantum spin Hall model (Sec. 4.2.2) as a function of the momentum, $E = -0.4$. In (a) the vectors Φ_e are normed but not orthogonalized, in (b) the vectors are orthogonalized using a QR decomposition.

It is important to note that the transformation from $H_{\text{eff}}(E)$ to $H'_{\text{eff}}(E)$ does not affect the zero-valued eigenvalues – the only ones with a physical meaning. Furthermore, replacing Φ by ΦT also changes q_e by $T^{-1}q_e$, so that the final wavefunction $\Psi(j)$ in Eq. (3.7) remains unchanged. This is why the algorithms of Sec. 3.3 remain correct, but require a fluctuation-tolerant root-finder when implemented naively. In practice, it is preferable to fix a unique spectrum such that an efficient standard root-finder can be used. The matrices Φ_e cannot be fixed in a unique way, but one can choose the column vectors such that the degenerate ones are orthogonal. To this end, one performs the QR decomposition $\Phi_e = QR$, where Q is an orthogonal matrix and R an upper triangular matrix, and substitutes in Eq. (3.17):

$$\Phi_e \rightarrow Q, \quad (\text{A.11})$$

$$\Lambda_e \rightarrow R\Lambda_e R^{-1}, \quad (\text{A.12})$$

$$q_e \rightarrow R^{-1}q_e. \quad (\text{A.13})$$

The resulting smooth eigenvalues are shown in Fig. A.1(b).

Orthogonalizing Φ_e forces the matrix T to be unitary, as we can understand using the following geometrical argument. Any superposition on two vectors \mathbf{e}_1 and \mathbf{e}_2 of the (x, y) plane is still a valid basis as long as they are not collinear. If one forces the vectors to be perpendicular to each other, then the only transformation left is a rotation, in other words a unitary transformation.

Appendix B

Mostly translationally invariant system appendix

B.1 Laurent expansion of the inverse of a matrix

Let $A(x)$ be a matrix that depends on a continuous parameter x . $A(x)$ is defined in terms of its expansion in power of x ,

$$A(x) = A_0 + xA_1 + x^2A_2 + \dots \quad (\text{B.1})$$

Let G be the inverse of A ,

$$A(x)G(x) = \mathbf{1}. \quad (\text{B.2})$$

The aim of this appendix is to calculate the terms G_k of the Laurent expansion of $G(x)$,

$$G(x) = \sum_{k=-\infty}^{\infty} G_k x^k, \quad (\text{B.3})$$

in terms of the expansion of $A(x)$. If A_0 is invertible, this problem is trivial: one simply insert the expansion of $A(x)$ and $G(x)$ in Eq. (B.2) and identify the terms one by one. One gets,

$$G_0 = A_0^{-1} \quad (\text{B.4})$$

$$G_1 = -A_0^{-1}A_1A_0^{-1} \quad (\text{B.5})$$

$$G_n = -A_0^{-1} \sum_{p=0}^{n-1} A_{n-p} G_p \quad (\text{B.6})$$

$$(\text{B.7})$$

In this appendix, we focus on the case where A_0 is not invertible which leads to the appearance of a term G_{-1} . Let P be the projector on the Kernel

of A_0 , i.e. $A_0P = 0$, and $Q = \mathbb{1} - P$. To proceed, we write Eq. (B.2) in block form in the P and Q subblocks.

$$\begin{aligned} (A_0 + xA_1 + x^2A_2 + \dots)(P + Q)G &= \mathbb{1}, \\ [A_1 + xA_2 + \dots]xP + (A_0 + xA_1 + x^2A_2 + \dots)Q &] G = \mathbb{1}. \end{aligned}$$

Introducing the new variable

$$\bar{G} = (Px + Q)G, \quad (\text{B.8})$$

and the new series

$$B(x) \equiv B_0 + B_1x + B_2x^2 + \dots \quad (\text{B.9})$$

with

$$B_k = A_{k+1}P + A_kQ. \quad (\text{B.10})$$

These variables allow one to map the problem of calculating \bar{G} to a problem that has the same structure as Eq. (B.2),

$$B(x)\bar{G}(x) = \mathbb{1}. \quad (\text{B.11})$$

If $B_0 = A_1P + A_0Q = A_1P + A_0$ is invertible, then a term by term identification of Eq. (B.11) leads to

$$\bar{G}_0 = B_0^{-1} \quad (\text{B.12})$$

$$\bar{G}_1 = -B_0^{-1}B_1B_0^{-1} \quad (\text{B.13})$$

$$\bar{G}_n = -B_0^{-1} \sum_{p=0}^{n-1} B_{n-p} \bar{G}_p \quad (\text{B.14})$$

$$(\text{B.15})$$

Eq. (B.8) can be inverted in

$$G = \left(\frac{1}{x}P + Q \right) \bar{G} \quad (\text{B.16})$$

and we finally arrive at

$$G_{-1} = P \frac{1}{A_1P + A_0} \quad (\text{B.17})$$

$$\begin{aligned} G_0 &= -P \frac{1}{A_1P + A_0} (A_2P + A_1Q) \frac{1}{A_1P + A_0} \\ &+ Q \frac{1}{A_1P + A_0} \end{aligned} \quad (\text{B.18})$$

$$G_n = P\bar{G}_{n+1} + Q\bar{G}_n. \quad (\text{B.19})$$

$$(\text{B.20})$$

Eq. (B.17) is the central result used for the construction of the residue solver. In all the calculations that we have performed, we have always found B_0 to be invertible. If B_0 is not invertible, the same construction that has been done on Eq. (B.2) can be performed on Eq. (B.11). In that case, one would introduce the projector P' on the kernel of B_0 and proceed to expand $\overline{\overline{G}} = P'\overline{G} + (1 - P')\overline{G}$. In that case, the development of $G(x)$ would start at G_{-2} . The same procedure can be extended iteratively to the case where the development starts at G_{-n} .

Bibliography

- [1] A. MacKinnon. The calculation of transport properties and density of states of disordered solids. *Zeitschrift für Physik B Condensed Matter*, 59(4):385–390, Dec 1985.
- [2] G. Metalidis and P. Bruno. Green’s function technique for studying electron flow in two-dimensional mesoscopic samples. *Phys. Rev. B*, 72:235304, Dec 2005.
- [3] Harold U. Baranger, David P. DiVincenzo, Rodolfo A. Jalabert, and A. Douglas Stone. Classical and quantum ballistic-transport anomalies in microjunctions. *Phys. Rev. B*, 44:10637–10675, Nov 1991.
- [4] K. Kazymyrenko and X. Waintal. Knitting algorithm for calculating green functions in quantum systems. *Phys. Rev. B*, 77:115119, Mar 2008.
- [5] Alexander Weiße, Gerhard Wellein, Andreas Alvermann, and Holger Fehske. The kernel polynomial method. *Rev. Mod. Phys.*, 78:275–306, Mar 2006.
- [6] Zheyong Fan, Jose Hugo Garcia, Aron W Cummings, Jose-Eduardo Barrios, Michel Panhans, Ari Harju, Frank Ortmann, and Stephan Roche. Linear scaling quantum transport methodologies. *arXiv preprint arXiv:1811.07387*, 2018.
- [7] Christoph W Groth, Michael Wimmer, Anton R Akhmerov, and Xavier Waintal. Kwant: a software package for quantum transport. *New J. Phys.*, 16(6):063065, 2014.
- [8] Richard Stallman. *Free software, free society: Selected essays of Richard M. Stallman*. Lulu. com, 2002.
- [9] Christoph W Groth, Michael Wimmer, Anton R Akhmerov, and Xavier Waintal. Kwant: a software package for quantum transport. *New Journal of Physics*, 16(6):063065, 2014.

- [10] S. Birner, T. Zibold, T. Andlauer, T. Kubis, M. Sabathil, A. Trellakis, and P. Vogl. nextnano: General purpose 3-d simulations. *IEEE Transactions on Electron Devices*, 54(9):2137–2142, Sep. 2007.
- [11] J. E. Fonseca, T. Kubis, M. Povolotskyi, B. Novakovic, A. Ajoy, G. Hegde, H. Ilatikhameneh, Z. Jiang, P. Sengupta, Y. Tan, and G. Klimeck. Efficient and realistic device modeling from atomic detail to the nanoscale. *Journal of Computational Electronics*, 12(4):592–600, Dec 2013.
- [12] Supriyo Datta. *Electronic transport in mesoscopic systems*. Cambridge university press, 1997.
- [13] Markus König, Steffen Wiedmann, Christoph Brüne, Andreas Roth, Hartmut Buhmann, Laurens W. Molenkamp, Xiao-Liang Qi, and Shou-Cheng Zhang. Quantum spin hall insulator state in hgte quantum wells. *Science*, 318(5851):766–770, 2007.
- [14] Luca Banszerus, Michael Schmitz, Stephan Engels, Matthias Goldsche, Kenji Watanabe, Takashi Taniguchi, Bernd Beschoten, and Christoph Stampfer. Ballistic transport exceeding 28 nm in cvd grown graphene. *Nano letters*, 16:1387, 01 2016.
- [15] D. J. Thouless, M. Kohmoto, M. P. Nightingale, and M. den Nijs. Quantized hall conductance in a two-dimensional periodic potential. *Phys. Rev. Lett.*, 49:405–408, Aug 1982.
- [16] Mervyn Roy. The tight-binding method, 2015.
- [17] Nathan Argaman and Guy Makov. Density functional theory: An introduction. *American Journal of Physics*, 68(1):69–79, 2000.
- [18] N ASHCROFT and N MERMIN. *Solid state physics.[Sl]: Saunders College, 1976*.
- [19] Eric Jones, Travis Oliphant, Pearu Peterson, et al. SciPy: Open source scientific tools for Python, 2001–. [Online; accessed \uparrow today \downarrow].
- [20] Travis Oliphant. NumPy: A guide to NumPy. USA: Trelgol Publishing, 2006–. [Online; accessed \uparrow today \downarrow].
- [21] Waintal X, Nikolic B, Akhmerov A, Istas M, et al. Computational quantum transport. In preparation.
- [22] Michael Wimmer. Quantum transport in nanostructures: From computational concepts to spintronics in graphene and magnetic tunnel junctions, December 2009.

- [23] Yuli V Nazarov and Yaroslav M Blanter. *Quantum transport: introduction to nanoscience*. Cambridge University Press, 2009.
- [24] Benoit Gaury, Joseph Weston, and Xavier Waintal. Stopping electrons with radio-frequency pulses in the quantum hall regime. *Phys. Rev. B*, 90:161305, Oct 2014.
- [25] S. Reich, J. Maultzsch, C. Thomsen, and P. Ordejón. Tight-binding description of graphene. *Phys. Rev. B*, 66:035412, Jul 2002.
- [26] Yigal Meir and Ned S. Wingreen. Landauer formula for the current through an interacting electron region. *Phys. Rev. Lett.*, 68:2512–2515, Apr 1992.
- [27] B. J. van Wees, H. van Houten, C. W. J. Beenakker, J. G. Williamson, L. P. Kouwenhoven, D. van der Marel, and C. T. Foxon. Quantized conductance of point contacts in a two-dimensional electron gas. *Phys. Rev. Lett.*, 60:848–850, Feb 1988.
- [28] Daniel S. Fisher and Patrick A. Lee. Relation between conductivity and transmission matrix. *Phys. Rev. B*, 23:6851–6854, Jun 1981.
- [29] Patrick A Lee and Daniel S Fisher. Anderson localization in two dimensions. *Phys. Rev. Lett.*, 47(12):882, 1981.
- [30] A MacKinnon. The calculation of transport properties and density of states of disordered solids. *Zeitschrift für Physik B Condensed Matter*, 59(4):385–390, 1985.
- [31] Taisuke Ozaki, Kengo Nishio, and Hiori Kino. Efficient implementation of the nonequilibrium green function method for electronic transport calculations. *Phys. Rev. B*, 81(3):035116, 2010.
- [32] A Reily Rocha, Víctor M García-Suárez, S Bailey, C Lambert, J Ferrer, and Stefano Sanvito. Spin and molecular electronics in atomically generated orbital landscapes. *Phys. Rev. B*, 73(8):085414, 2006.
- [33] James E Fonseca, T Kubis, Michael Povolotskyi, Bozidar Novakovic, Arvind Ajoy, G Hegde, Hesameddin Ilatikhameneh, Zhengping Jiang, Parijat Sengupta, Y Tan, et al. Efficient and realistic device modeling from atomic detail to the nanoscale. *J. Comput. Electron.*, 12(4):592–600, 2013.
- [34] T Van der Sar, ZH Wang, MS Blok, H Bernien, TH Taminiau, DM Toyli, DA Lidar, DD Awschalom, R Hanson, and VV Dobrovitski. Decoherence-protected quantum gates for a hybrid solid-state spin register. *Nat.*, 484(7392):82–86, 2012.

- [35] AF Andreev. The thermal conductivity of the intermediate state in superconductors. *Journal of Experimental and Theoretical Physics*, 46(5):1823–1828, 1964.
- [36] A Yu Kitaev. Unpaired majorana fermions in quantum wires. *Phys. Usp.*, 44(10S):131, 2001.
- [37] Yuval Oreg, Gil Refael, and Felix von Oppen. Helical liquids and majorana bound states in quantum wires. *Phys. Rev. Lett.*, 105(17):177002, 2010.
- [38] Roman M Lutchyn, Jay D Sau, and S Das Sarma. Majorana fermions and a topological phase transition in semiconductor-superconductor heterostructures. *Phys. Rev. Lett.*, 105(7):077001, 2010.
- [39] Rosario EV Profumo, Christoph Groth, Laura Messio, Olivier Parcollet, and Xavier Waintal. Quantum monte carlo for correlated out-of-equilibrium nanoelectronic devices. *Phys. Rev. B*, 91(24):245154, 2015.
- [40] CWJ Beenakker. Universal limit of critical-current fluctuations in mesoscopic josephson junctions. *Phys. Rev. Lett.*, 67(27):3836, 1991.
- [41] CWJ Beenakker. Andreev billiards. In *Quantum Dots: a Doorway to Nanoscale Physics*, pages 131–174. Springer, 2005.
- [42] Kun Woo Kim, Tami Pereg-Barnea, and Gil Refael. Semiclassical approach to bound states of a pointlike impurity in a two-dimensional dirac system. *Phys. Rev. B*, 89:085117, Feb 2014.
- [43] P. A. Knipp and T. L. Reinecke. Boundary-element method for the calculation of electronic states in semiconductor nanostructures. *Phys. Rev. B*, 54:1880–1891, Jul 1996.
- [44] J Von Neuman and Eugene Wigner. Uber merkwürdige diskrete eigenwerte. uber das verhalten von eigenwerten bei adiabatischen prozessen. *Z. Phys. B Condens. Matter*, 30:467–470, 1929.
- [45] Konstantin Pichugin, Holger Schanz, and Petr Šeba. Effective coupling for open billiards. *Phys. Rev. E*, 64:056227, Oct 2001.
- [46] Almas F Sadreev, Evgeny N Bulgakov, and Ingrid Rotter. Bound states in the continuum in open quantum billiards with a variable shape. *Phys. Rev. B*, 73(23):235342, 2006.
- [47] T. Ando. Quantum point contacts in magnetic fields. *Phys. Rev. B*, 44:8017–8027, Oct 1991.

- [48] D J Thouless and S Kirkpatrick. Conductivity of the disordered linear chain. *Journal of Physics C: Solid State Physics*, 14(3):235, 1981.
- [49] Jeremy Taylor, Hong Guo, and Jian Wang. Ab initio modeling of quantum transport properties of molecular electronic devices. *Phys. Rev. B*, 63:245407, Jun 2001.
- [50] Abhijeet Alase, Emilio Cobanera, Gerardo Ortiz, and Lorenza Viola. Exact solution of quadratic fermionic hamiltonians for arbitrary boundary conditions. *Phys. Rev. Lett.*, 117:076804, Aug 2016.
- [51] Abhijeet Alase, Emilio Cobanera, Gerardo Ortiz, and Lorenza Viola. Generalization of bloch’s theorem for arbitrary boundary conditions: Theory. *Phys. Rev. B*, 96:195133, Nov 2017.
- [52] Durbha V Murthy and Raphael T Haftka. Derivatives of eigenvalues and eigenvectors of a general complex matrix. *Int. J. Numer. Methods. Eng.*, 26(2):293–311, 1988.
- [53] B Andrei Bernevig, Taylor L Hughes, and Shou-Cheng Zhang. Quantum spin hall effect and topological phase transition in hgte quantum wells. *Sci.*, 314(5806):1757–1761, 2006.
- [54] M. M. Vazifeh and M. Franz. Electromagnetic response of weyl semimetals. *Phys. Rev. Lett.*, 111:027201, Jul 2013.
- [55] P Baireuther, J Tworzydło, M Breitzkreiz, İnanç Adagideli, and CWJ Beenakker. Weyl-majorana solenoid. *New J. Phys.*, 19(2):025006, 2017.
- [56] Patrick A. Lee and Daniel S. Fisher. Anderson localization in two dimensions. *Phys. Rev. Lett.*, 47:882–885, Sep 1981.
- [57] D J Thouless and S Kirkpatrick. Conductivity of the disordered linear chain. *Journal of Physics C: Solid State Physics*, 14(3):235–245, jan 1981.
- [58] T. Ando. Quantum point contacts in magnetic fields. *Phys. Rev. B*, 44:8017–8027, Oct 1991.
- [59] Ajit Agrawal, Philip Klein, and R Ravi. Cutting down on fill using nested dissection: provably good elimination orderings. In *Graph Theory and Sparse Matrix Computation*, pages 31–55. Springer, 1993.
- [60] Su-Yang Xu, Ilya Belopolski, Nasser Alidoust, Madhab Neupane, Guang Bian, Chenglong Zhang, Raman Sankar, Guoqing Chang, Zhu-jun Yuan, Chi-Cheng Lee, Shin-Ming Huang, Hao Zheng, Jie Ma, Daniel S. Sanchez, BaoKai Wang, Arun Bansil, Fangcheng Chou,

- Pavel P. Shibayev, Hsin Lin, Shuang Jia, and M. Zahid Hasan. Discovery of a weyl fermion semimetal and topological fermi arcs. *Science*, 349(6248):613–617, 2015.
- [61] Cornelius Lanczos. *An iteration method for the solution of the eigenvalue problem of linear differential and integral operators*. United States Governm. Press Office Los Angeles, CA, 1950.
- [62] Markus Aichhorn, Maria Daghofer, Hans Gerd Evertz, and Wolfgang von der Linden. Low-temperature lanczos method for strongly correlated systems. *Phys. Rev. B*, 67:161103, Apr 2003.
- [63] J. Jaklič and P. Prelovšek. Finite-temperature properties of doped antiferromagnets. *Advances in Physics*, 49(1):1–92, 2000.
- [64] Pierre Darancet, Valerio Olevano, and Didier Mayou. Quantum transport through resistive nanocontacts: Effective one-dimensional theory and conductance formulas for nonballistic leads. *Phys. Rev. B*, 81:155422, Apr 2010.
- [65] Scheer Elke and Cuevas Juan Carlos. *Molecular electronics: an introduction to theory and experiment*, volume 15. World Scientific, 2017.
- [66] Supriyo Datta. *Electronic Transport in Mesoscopic Systems*. Cambridge Studies in Semiconductor Physics and Microelectronic Engineering. Cambridge University Press, 1995.
- [67] M. Istas, C. Groth, A. R. Akhmerov, M. Wimmer, and X. Waintal. A general algorithm for computing bound states in infinite tight-binding systems. *SciPost Phys.*, 4:26, 2018.
- [68] MF Crommie, CP Lutz, and DM Eigler. Imaging standing waves in a two-dimensional electron gas. *Nature*, 363(6429):524, 1993.
- [69] Walter A Harrison. *Solid state theory*. Courier Corporation, 1980.
- [70] B. Andrei Bernevig, Taylor L. Hughes, and Shou-Cheng Zhang. Quantum spin hall effect and topological phase transition in hgte quantum wells. *Science*, 314(5806):1757–1761, 2006.
- [71] Weizhe Edward Liu, Ewelina M. Hankiewicz, and Dimitrie Culcer. Quantum transport in weyl semimetal thin films in the presence of spin-orbit coupled impurities. *Phys. Rev. B*, 96:045307, Jul 2017.
- [72] Andrew K. Mitchell and Lars Fritz. Signatures of weyl semimetals in quasiparticle interference. *Phys. Rev. B*, 93:035137, Jan 2016.

- [73] Justin H. Wilson, J. H. Pixley, David A. Huse, Gil Refael, and S. Das Sarma. Do the surface fermi arcs in weyl semimetals survive disorder? *Phys. Rev. B*, 97:235108, Jun 2018.
- [74] Pierre Darancet, Valerio Olevano, and Didier Mayou. Coherent electronic transport through graphene constrictions: Subwavelength regime and optical analogy. *Phys. Rev. Lett.*, 102:136803, Mar 2009.
- [75] M. Büttiker. Time-dependent current partition in mesoscopic conductors. *Il Nuovo Cimento B (1971-1996)*, 110(5):509–522, May 1995.
- [76] Su-Yang Xu, Nasser Alidoust, Ilya Belopolski, Zhujun Yuan, Guang Bian, Tay-Rong Chang, Hao Zheng, Vladimir N Strocov, Daniel S Sanchez, Guoqing Chang, et al. Discovery of a weyl fermion state with fermi arcs in niobium arsenide. *Nature Physics*, 11(9):748, 2015.
- [77] Ke Deng, Guoliang Wan, Peng Deng, Kenan Zhang, Shijie Ding, Eryin Wang, Mingzhe Yan, Huaqing Huang, Hongyun Zhang, Zhilin Xu, et al. Experimental observation of topological fermi arcs in type-ii weyl semimetal mote 2. *Nature Physics*, 12(12):1105, 2016.
- [78] E. V. Gorbar, V. A. Miransky, I. A. Shovkovy, and P. O. Sukhachov. Origin of dissipative fermi arc transport in weyl semimetals. *Phys. Rev. B*, 93:235127, Jun 2016.
- [79] Björn Sbierski, Gregor Pohl, Emil J. Bergholtz, and Piet W. Brouwer. Quantum transport of disordered weyl semimetals at the nodal point. *Phys. Rev. Lett.*, 113:026602, Jul 2014.
- [80] Sergey V. Syzranov and Leo Radzihovsky. High-dimensional disorder-driven phenomena in weyl semimetals, semiconductors, and related systems. *Annual Review of Condensed Matter Physics*, 9(1):35–58, 2018.
- [81] J. H. Pixley, Pallab Goswami, and S. Das Sarma. Anderson localization and the quantum phase diagram of three dimensional disordered dirac semimetals. *Phys. Rev. Lett.*, 115:076601, Aug 2015.
- [82] Chui-Zhen Chen, Juntao Song, Hua Jiang, Qing-feng Sun, Ziqiang Wang, and X. C. Xie. Disorder and metal-insulator transitions in weyl semimetals. *Phys. Rev. Lett.*, 115:246603, Dec 2015.
- [83] Pedro Gonnet. *Adaptive quadrature re-revisited*. PhD thesis, ETH Zurich, 2009.
- [84] Juan Carlos Cuevas and Elke Scheer. *Molecular Electronics*. WORLD SCIENTIFIC, 2010.

- [85] Alexander L Fetter and John Dirk Walecka. *Quantum theory of many-particle systems*. Courier Corporation, 2012.
- [86] Cristina Bena, Sudip Chakravarty, Jiangping Hu, and Chetan Nayak. Quasiparticle scattering and local density of states in the d-density-wave phase. *Phys. Rev. B*, 69:134517, Apr 2004.
- [87] Annica M. Black-Schaffer and Alexander V. Balatsky. Subsurface impurities and vacancies in a three-dimensional topological insulator. *Phys. Rev. B*, 86:115433, Sep 2012.
- [88] Caio H. Lewenkopf and Eduardo R. Mucciolo. The recursive green’s function method for graphene. *Journal of Computational Electronics*, 12(2):203–231, Jun 2013.
- [89] James A. Lawlor and Mauro S. Ferreira. Green functions of graphene: An analytic approach. *Physica B: Condensed Matter*, 463:48 – 53, 2015.
- [90] Gerbold C Ménard, Sébastien Guissart, Christophe Brun, Stéphane Pons, Vasily S Stolyarov, François Debontridder, Matthieu V Leclerc, Etienne Janod, Laurent Cario, Dimitri Roditchev, et al. Coherent long-range magnetic bound states in a superconductor. *Nature Physics*, 11(12):1013, 2015.
- [91] Madhab Neupane, Su-Yang Xu, Raman Sankar, Nasser Alidoust, Guang Bian, Chang Liu, Ilya Belopolski, Tay-Rong Chang, Horng-Tay Jeng, Hsin Lin, et al. Observation of a three-dimensional topological dirac semimetal phase in high-mobility cd 3 as 2. *Nature communications*, 5:3786, 2014.
- [92] D. G. Salinas, S. Guéron, D. C. Ralph, C. T. Black, and M. Tinkham. Effects of spin-orbit interactions on tunneling via discrete energy levels in metal nanoparticles. *Phys. Rev. B*, 60:6137–6145, Aug 1999.
- [93] D. C. Ralph, C. T. Black, and M. Tinkham. Gate-voltage studies of discrete electronic states in aluminum nanoparticles. *Phys. Rev. Lett.*, 78:4087–4090, May 1997.